Search for cosmic neutrinos with ANTARES

Search for cosmic neutrinos with ANTARES

ACADEMISCH PROEFSCHRIFT

ter verkrijging van
de graad van Doctor aan de Universiteit Leiden,
op gezag van Rector Magnificus prof.mr. C. J. J. M. Stolker,
volgens besluit van het College voor Promoties
te verdedigen op donderdag 15 mei 2014
klokke 15:00 uur

door

Claudio Bogazzi

geboren te Massa, Italië
in 1984

Promotor:	Prof. dr. M. de Jong
Co-promotor:	Dr. A. J. Heijboer (Nikhef, Amsterdam)
Overige leden:	Prof. dr. E. R. Eliel
	Prof. dr. A. Achúcarro
	Dr. D. F. E. Samtleben
	Prof. dr. P. Kooijman (Universiteit van Amsterdam)
	Dr. D. Berge (Universiteit van Amsterdam)
	Dr. J. Brunner (Centre de physique des particules de Marseille)

Casimir PhD series, Delft-Leiden 2014-8
ISBN 978-90-8593-183-6
First published in print format 2014.

The work described in this thesis is part of the research program of Fundamental Research on Matter (FOM), which is part of the Netherlands Organisation for Scientific Research (NWO).
The research was carried out at the National Institute for Subatomic Physics (NIKHEF) in Amsterdam, The Netherlands.

Cover Image Title: Bioluminescence at Squeaky Beach.
Description: The ghostly blue light produced by small single-celled marine micro-organisms Noctiluca scintillans, commonly known as the Sea Sparkle, in the waters of the Southern Ocean. Planet Jupiter and constellations of the Bull (Taurus) and the Hunter (Orion) are prominent in the Summer skies.
Location: Squeaky Beach, Wilsons Promontory, Victoria, Australia.
Tech data: Single image. Nikon D3S, Nikon 14-24mm lens, f/2.8, 30 sec, ISO 3200.
Credit line: Alex Cherney©(www.terrastro.com)

Printed in The Netherlands by Ipskamp Drukkers B.V.

A nonno Salvatore,
che ha osservato le stelle
molto prima del sottoscritto
e con intenti diversi
ma altrettanto importanti.

A zio Mario, che lo ha raggiunto.

Zoeken naar kosmische neutrino's met ANTARES

Contents

Introduction

Considerate la vostra semenza: fatti non foste a viver come bruti, ma per seguir virtute e canoscenza
Consider ye the seed from which ye sprang: Ye were not made to live like unto brutes, but for pursuit of virtue and of knowledge.

Dante Alighieri, The Divine Comedy, Inferno: Canto XXVI

The observation of the sky is something that humanity has done since its dawn. In fact it is generally believed that astronomy is the oldest of the sciences.

Through the centuries, many ancient civilizations have performed astronomical observations of the visible light coming from celestial objects. Early cultures looked at celestial objects and related them to gods and myths. It is not a surprise that the first astronomers were priests [1]. Their temples, such as Stonehenge, were built for both astronomical and religious functions.

During the Middle Ages, astronomy started to slowly separate from religion. The contribution from the Islamic world was crucial and with the work of Ibn al-Haytham (Alhazen) in the 11th century, astronomy became an independent science.

A first big improvement was made with the invention of the telescope, made by the Dutch lensmaker Hans Lippershey. Galileo Galilei was one of the first scientist to use an optical telescope to observe the sky. He discovered the four largest moons of Jupiter, the craters of our Moon and observed sunspots and Venus phases.

Modern astronomy started in the 19th century with the discovery of the first spectral lines from celestial objects. With the development of spectroscopy, during the 20th century, the observations were not restricted anymore to the visible part of the spectrum. Telescopes, allowing to detect light from the very low radio frequencies to the high frequencies of γ-rays, introduced a new way to investigate the mysteries of the Universe.

In the 20th century a new window on the Universe was opened. In 1912, Victor Francis Hess carried three electrometers to an altitude of 5.3 km by mean of balloons to investigate the ionisation of the atmosphere and, in particular, its dependence with altitude. During that time it was generally believed that the ionisation of the air was a consequence of the radiation emitted by the decay of radioactive elements in the ground. Hess results clearly showed that the ionising radiation decreased up to 1.5 km. Then, an increase was observed and surprisingly [2] "the increase reaches, at altitudes of 3000 to 4000 m, already 50% of the total radiation observed on the ground. [...] At 4000 to 5200 m the radiation is stronger (more than 160%) than on the ground". Hess concluded that the only possible

explanation for this increase was that the radiation comes from above, i.e. it has extra-terrestrial origin. For the discovery of the cosmic radiation, Hess was awarded the Nobel Prize in 1936.

Cosmic rays and the observed light from astrophysical sources are two sides of the same coin. Some of the objects observed in different wavelengths by astronomers around the world are also thought to be responsible of the origin and acceleration of cosmic rays.

Neutrino astronomy, i.e. the study and detection of neutrinos with extraterrestrial origin, is a new field which, together with gamma-ray astronomy and cosmic ray physics, is now a part of a multimessenger way to observe the sky. Whereas light is absorbed by the interstellar matter and charged particles are deflected by Galactic and extragalactic magnetic fields during their journey to the Earth, neutrinos, due to their neutral and weakly interacting nature, points back to their source of origin. The information carried by astrophysical neutrinos could provide the answers to the remaining questions about cosmic rays origins, production and acceleration.

The work presented in this thesis describes a search for point-like sources of astrophysical neutrinos with the ANTARES telescope. The ANTARES detector is located at the bottom of the Mediterranean sea, 50 km off the French coast. It consists of 12 vertical lines equipped with photomultiplier tubes to detect the Cherenkov light emitted by relativistic muons created by the interaction of neutrinos with matter. Data collected from January 2007 to December 2010 are used for the analysis.

There are different ways to look for an excess of cosmic neutrinos above the background of atmospheric muons and neutrinos. The search for a diffuse flux of astrophysical neutrinos represents one of them, especially if the single point-like sources are too weak to be detected. In this case, the presence of an excess of signal events is tested by analysing the energy spectrum as astrophysical neutrinos are expected to have an harder spectrum than atmospheric neutrinos.

In a search for point-like sources of cosmic neutrinos the presence of an excess of signal events is tested by looking for clusters of events coming from the same direction.

The search was done via hypothesis testing, using a likelihood ratio approach. The null hypothesis was the case where our sample contains only atmospheric muons and neutrinos background. The alternative hypothesis states that in addition to this background there are signal events. Two alternative searches were performed. In the full-sky search, the presence of an excess of signal events over the background was tested anywhere in the visible sky, i.e. in the declination range $(-90^\circ, +48^\circ)$. In the candidate list search, we looked for an excess of events at the locations of 51 predefined candidate sources.

The inclusion of a possible source extension in the likelihood was also investigated as well as assuming an exponential cut-off function to describe the cosmic neutrino spectrum instead of the standard E_ν^{-2} flux. Specific models of neutrino emission from three Galactic sources were also tested.

This thesis is organised in the following way. Chapter 1 gives a review of the physics behind cosmic rays and introduces the astronomy with neutrinos. Chapter 2 briefly outlines the gamma-ray astronomy and focuses on three Galactic objects which are believed to be sources of cosmic rays and neutrinos. For each of these sources, three models describing the emission of neutrinos are presented. In Chapter 3 the ANTARES neutrino telescope and its detection principle are discussed. Chapter 4 describes the simulation tools and the

reconstruction strategy used in the analysis. The final data sample is presented in Chapter 6 while Chapter 5 reports several systematic studies done to constrain the acceptance and the angular resolution of the detector. The algorithm developed for the search is described in Chapter 7 and finally the results are presented in Chapter 8.

1. Cosmic rays and neutrino astronomy

Okay, the unexpected I can deal with...
as long as I'm expecting it, that is...

Peter Parker

This chapter focuses on cosmic rays and their connection to neutrinos. It is likely that neutrinos are created by the interactions of accelerated protons and nuclei near their sources. Being neutral particles, neutrinos are not deflected by the galactic magnetic fields. Thus, detecting astrophysical neutrinos could help to identify the source of cosmic rays.

The chapter is divided in three sections: Section 1.1 will briefly discuss the main properties of cosmic rays and the mechanism thought to be responsible for their acceleration. Section 1.2 will introduce neutrino astronomy with particular attention to neutrino production from cosmic rays. Potential cosmic rays and neutrinos sources will be presented in Section 1.3.

1.1. Cosmic rays

Cosmic rays (CRs) are energetic particles, which continuously hit the Earth's atmosphere. Primary CRs mainly consist of ionised nuclei such as protons ($\sim 85\%$), helium ($\sim 12\%$) and heavier nuclei ($\sim 1\%$) [3]. The remaining component includes electrons.

1.1.1. Flux and energy spectrum

The differential flux of cosmic rays, shown in Figure 1.1, spans many orders of magnitude in energy and it is roughly described by a broken power-law formula

$$\frac{dN}{dE} \propto E^{-\gamma}, \tag{1.1}$$

where E is the energy of the primary particle and γ is called the spectral index. The spectral index has a value of about 2.7 below $E \simeq 4 \times 10^{15}$ eV. At this energy, the "knee", the spectral index changes to 3.3. At higher energies, $E \sim 3 \times 10^{18}$ eV, it changes again to 2.6 resulting in a concave shape of the spectrum curve, the so called "ankle".

Two possible scenarios explain the steepening of the flux around the knee region:

- In the first case, the knee is explained as a consequence of the limited spatial extension and magnetic field of the source accelerator. Since the energy of the cosmic

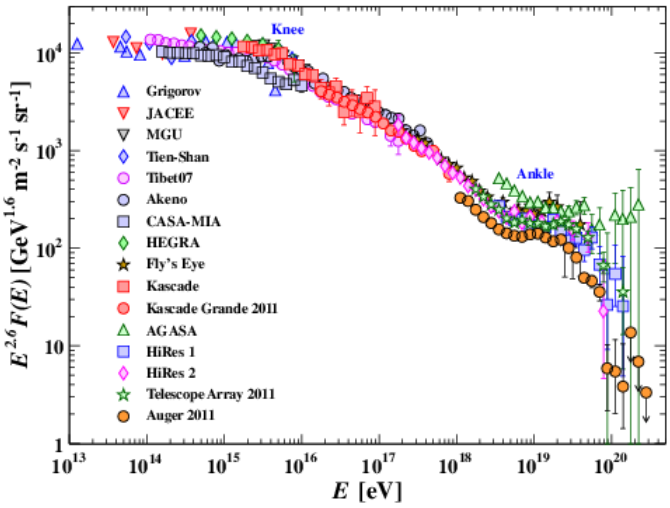

Figure 1.1.: All-particle cosmic rays energy spectrum [4]

rays is proportional to the charge of the particle, and the maximum energy the cosmic rays can be accelerated is determined by the size of the source, the size of the accelerating region has to be larger than the Larmor radius of the particle

$$r_L = 1.08 \frac{E/\mathrm{PeV}}{\mathrm{Z} \cdot \mathrm{B}/\mu\mathrm{G}} \ \mathrm{pc}, \tag{1.2}$$

where E is the energy of the particle with charge Z and B is the magnetic field of the source.

- The second scenario supposes that the galactic magnetic field is too weak to confine particles with energy above the knee. That is, the Larmor radius of a particle exceeds the thickness of the galactic disk and cosmic rays can escape the boundary of the Milky Way. Since the Larmor radius scales with E/Z, heavier nuclei can be kept inside our Galaxy up to higher energies compared to protons. Measurements on the cosmic ray composition could verify this theory.

The flattening of the energy spectrum at the ankle is generally explained as a transition from a Galactic to an extragalactic component [5]. Hence, the ankle is the energy at which the two components give an equal contribution to the particle flux. Cosmic rays above this energy are usually called Ultra-High-Energy Cosmic Rays (UHECR). Another possible interpretation is that the dip structure around the ankle region of the spectrum is

a consequence of the energy losses of protons interacting with the 2.7 K Cosmic Microwave Background (CMB)[6] via $\gamma + \mathrm{p} \rightarrow \mathrm{e}^+ + \mathrm{e}^- + \mathrm{p}$.

At the high-energy end of the spectrum the flux is suppressed. This is due to the so called Greisen-Zatsepsin-Kuz'min (GZK) effect [7, 8] which predicts that above 60 EeV protons lose energy by interacting with the CMB via pion production:

$$\begin{aligned} p + \gamma &\rightarrow \Delta^+(1232) \rightarrow p + \pi^0 \\ p + \gamma &\rightarrow \Delta^+(1232) \rightarrow n + \pi^+. \end{aligned} \tag{1.3}$$

1.1.2. Anisotropy of arrival directions

The presence of anisotropies in the arrival direction of high-energy cosmic rays on different angular scales may help to understand their propagation and deflection as well as to identify their sources.

The distribution of the arrival direction of cosmic rays with energies below 1 EeV is uniform because of the diffusion in the galactic magnetic field. Above this energy the galactic magnetic field is too weak to significantly deflect the cosmic rays and therefore the arrival directions of cosmic rays should point back to their sources[1]. As a consequence, assuming that the sources are not uniformly distributed, an anisotropic arrival direction distribution is expected for the most energetic cosmic rays.

The Pierre Auger Collaboration reported [10] in 2010 interesting results which showed a hint of correlation between the arrival directions of 69 events observed with energies above 57 EeV and the locations of Active Galactic Nuclei (AGN) with redshift $z \leq 0.018$ (distances ≤ 75 Mpc) within an opening angle of 3.1°. A fraction of 38% of these events is correlated with AGNs. This number has to be compared with the 21% expected if the cosmic rays flux were isotropic. Figure 1.2 shows the sky map in galactic coordinates of the 69 arrival directions of CRs together with the positions of 318 AGNs.

The center of the region which shows the largest excess of arrival directions among the 69 CRs above the isotropic expectation is only 4° away from the position of the AGN Centaurus A (see also Section 1.3.3). Figure 1.3 shows the number of events as a function of the cumulative angular distance Ψ_{CenA} from the direction of Centaurus A: 12 events are within 13° from the center of the AGN with an isotropic expectation of 1.7.

With more statistics it will be possible to tell if Centaurus A is the first UHECR source to be revealed. At lower energies where the distribution of cosmic rays is expected to be uniform, the identification of a source of origin is possible only with the detection of neutrinos. Centaurus A is also one of the candidate neutrino sources considered in this thesis. According to Cuoco and Hannestad [11] an event rate of 0.5 yr^{-1} is expected for a km^3 neutrino telescope.

1.1.3. Acceleration mechanism

The mechanism most widely considered to be responsible for accelerating CRs was proposed by Enrico Fermi in 1949 [12]. Fermi considered the interactions between CRs and

[1] A typical angular resolution for a surface array detector is around 1 degree, while hybrid detector can achieve a better pointing accuracy [9]

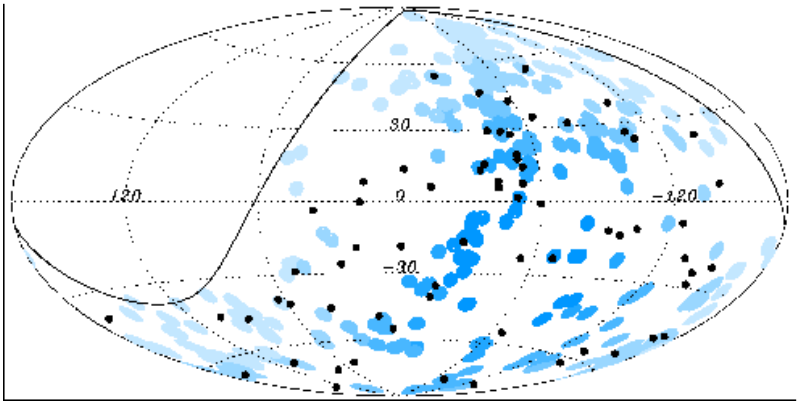

Figure 1.2.: Sky map in galactic coordinates of the 69 arrival directions of CRs with energy $E \geq 55$ EeV detected by the PAO up to December 2009 (black dots). Blue circles of radius 3.1° show the locations of the 318 selected AGNs within 75 Mpc. The darker is the blue the larger is the relative exposure. The solid line represents the field of view of the PAO for zenith angles smaller than 60°. The figure is taken from [10].

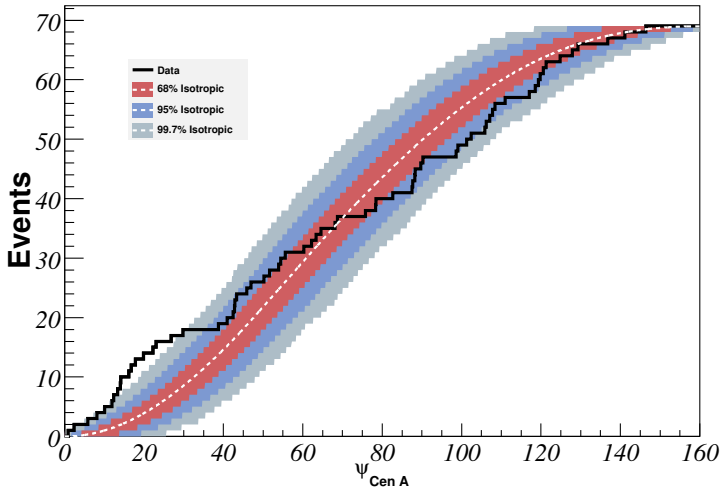

Figure 1.3.: Cumulative number of events as a function of the angular distance from the location of Centaurus A. The bands correspond to the 1σ, 2σ and 3σ confidence level (CL) for an expected isotropic flux. 13 arrival directions are within 18° from Centaurus A. Figure taken from [10].

interstellar magnetic clouds of plasma as responsible for the acceleration. A particle with initial energy E_1 enters a moving gas cloud where it is diffused by irregularities in the magnetic field. After a few deflections the particle emerges from the cloud in a random direction with energy E_2 (see the top illustration of Figure 1.4). In the rest frame of the moving cloud, the cosmic ray particle has total energy

$$E_1' = \gamma E_1(1 - \beta\cos\theta_1) = E_2', \tag{1.4}$$

with γ the Lorentz factor and $\beta = V/c$ the velocity of the cloud with respect to the laboratory frame (outside the cloud). The last equality is obtained by imposing energy conservation (the interactions between the particle and the magnetic field are elastic). The quantities with primes correspond to a frame moving with velocity V. Transforming to the laboratory frame gives:

$$E_2 = \gamma E_2'(1 + \beta\cos\theta_2'). \tag{1.5}$$

The change in energy in the laboratory frame is:

$$\frac{\Delta E}{E_1} = \frac{(E_2 - E_1)}{E_1} = \frac{1 - \beta\cos\theta_1 + \beta\cos\theta_2' - \beta^2\cos\theta_1 - \beta^2\cos\theta_1\cos\theta_2'}{1 - \beta^2} - 1. \tag{1.6}$$

The cosmic ray particle comes out from the cloud with random direction, thus $\langle\cos\theta_2'\rangle = 0$. The average value of $\cos\theta_1$ depends on the collision rate of cosmic rays with clouds for different angles so that the probability of a collision is proportional to the relative velocity between the cloud and the particle. Hence, $\langle\cos\theta_1\rangle = -V/3c$. The change in energy can now be written as:

$$\frac{\langle\Delta E\rangle}{E} = \frac{1 + \beta^2/3}{1 - \beta^2} \simeq \frac{4}{3}\beta^2. \tag{1.7}$$

From Equation 1.7 we conclude that $\langle\Delta E\rangle/E$ is positive (the particle gains energy) and is proportional to the square of beta. If $\beta << 1$ then the average energy gain per collision is very small. This is the so called 2nd order Fermi mechanism.

Fermi's theory has been extended in the 1970's (see [13] or [14] for more details) to describe a more efficient acceleration especially in the non-relativistic limit ($\beta << 1$). In this case the idea is that CR particles gain energy by bouncing back and forth over a shock fron such as the one emitted during a supernova explosion. On both sides of the shock the particles are elastically scattered off irregularities in the magnetic field.

To describe the model we consider for simplicity non-relativistic planar shocks. As illustrated in Figure 1.4 (bottom), we assume that a planar shock wave is moving with velocity $\vec{v}_s$ in the laboratory frame (region of unshocked material). V is now the velocity of the shocked material (downstream) relative to the unshocked material (upstream) and is related to the shock velocity by the relation

$$V = \frac{3}{4}v_s. \tag{1.8}$$

Equation 1.6 is also valid for this case. The main difference with the 2nd order Fermi acceleration comes from the angular average since particles can only exit planar shock

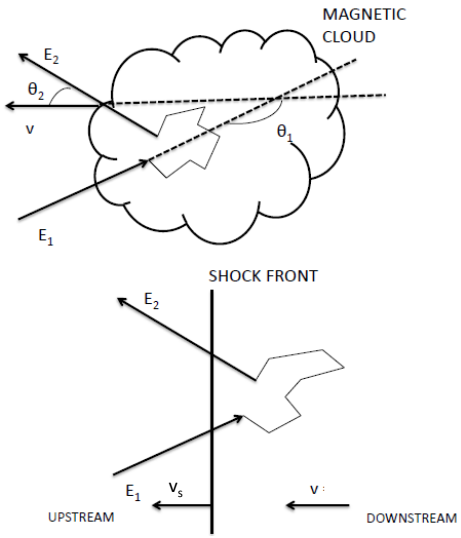

Figure 1.4.: Illustration of the second (top) and first (bottom) Fermi mechanism

fronts through the shock front. In this case $\langle \cos\theta_2' \rangle = 2/3$ and $\langle \cos\theta_1 \rangle = -2/3$. Thus

$$\frac{\langle \Delta E \rangle}{E} = \frac{1 + \frac{4}{3}\beta + \frac{4}{9}\beta^2}{1 - \beta^2} \simeq \frac{4}{3}\beta = \frac{v_s}{c}. \tag{1.9}$$

The average energy gain is now linear in β (1st order Fermi mechanism) therefore more efficient.

Another aspect which makes the 1st order Fermi mechanism a good candidate to describe CRs acceleration is the prediction of a power law flux with spectral index $\gamma = 2$ while from the 2nd order Fermi mechanism a prediction over the spectral index is impossible since it strictly depends on many parameters of the magnetic clouds.

1.2. Neutrino astronomy

On the night of February 23rd, 1987 in the Andes Mountains in Chile Ian Shelton, a research assistant at the University of Toronto pointed the big telescope of the Las Campanas observatory towards the Large Magellanic Cloud (LCM). He was looking for variable stars and novae. After three hours, as soon as the plates he was working on were developed he noticed a bright star of about 5th magnitude. The interesting thing was that, in that specific part of the sky, there should not have been any. At about the same time, Oscar Duhalde, another Las Campanas astronomer, was taking a break outside and noticed a new star in the LCM. Shelton and Duhalde were the first ones to discover the supernova SN1987A, perhaps the best-studied supernova in human history.

One of the first surprise of this supernova was its progenitor. Many models described red supergiant massive stars as typical progenitor for Type II supernova like SN1987A. However, the progenitor star of SN1987A was the blue supergiant Sanduleak -69° 202 with a mass of about $18M_{\odot}$, i.e. a relatively young and small star.

Following the suggestion of Bahcall, Dar and Piran [15], scientists from the Kamiokande II collaboration [16] looked for a possible a neutrino signal in their data. The result [17] opened a new window on the universe: a burst of 12 neutrino events was detected at 7h 35m 35s UT on February 23, two hours before the first optical light was recorded. Similar results (see [18, 19]) were obtained by the IMB [20] (8 events) and Baksan [21] (5 events) experiments. The observation of these events provided an unique opportunity to investigate the dynamics of supernova explosions [22].

Figure 1.5 shows the predicted astrophysical neutrino energy spectrum. It covers 15 orders of magnitude in energy and 42 in intensity of the flux. The analysis presented in this thesis is sensitive to neutrinos in the energy range 100 GeV - 100 TeV. In the following sections we discuss the main sources of astrophysical neutrinos from the low energy cosmic neutrino background to the high-energies.

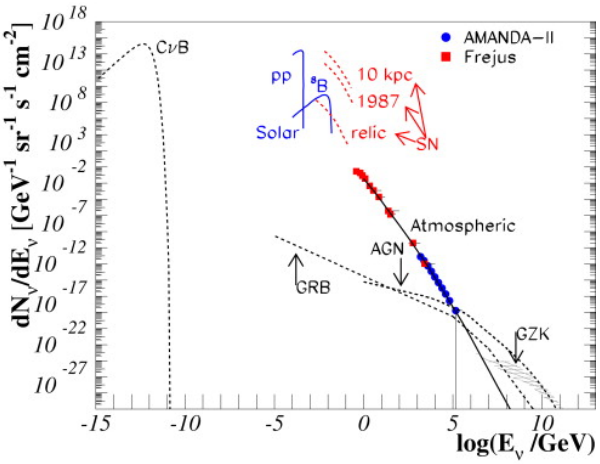

Figure 1.5.: Neutrino spectrum for several source predictions. The flux predicted from point sources have been scaled to $1/(4\pi)$ in order to be comparable with diffuse spectra. The atmospheric neutrino data are from the FREJUS (red squares) and AMANDA (blue circles) experiment. Figure taken from [23].

1.2.1. Cosmic neutrino background

The Cosmic Neutrino Background (CνB) is the neutrino equivalent of the Cosmic Microwave Background. It is a relic of the big bang which decoupled from matter when the universe was roughly 1 second old and had a temperature of about 1 MeV. Direct detection of the CνB represents a big challenge.

1.2.2. Solar neutrinos

The first identified source of extraterrestrial neutrinos is the Sun. Solar neutrinos are produced by the nuclear reactions that power the Sun such as the proton-proton (pp) chain and the CN-NO bi-cycle. The pp chain can be summarised by the reaction

$$4p \rightarrow {}^4He + 2e^+ + 2\nu_e, \tag{1.10}$$

with an average neutrino energy of $\langle E_\nu \rangle \sim 0.6$ MeV. The CN-NO bi-cycle also converts hydrogen to helium but involves heavier nuclei like carbon, nitrogen and oxygen. The energy spectrum of solar neutrinos is shown in Figure 1.6.

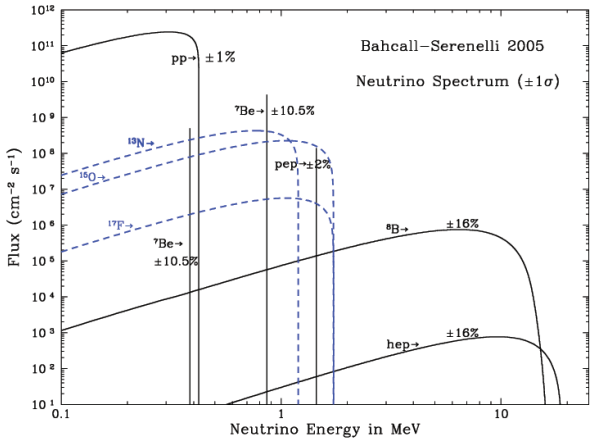

Figure 1.6.: Energy spectrum for solar neutrinos predicted by the standard solar model. Black solid lines show the neutrino flux from reactions of the pp chain, while blue lines correspond to the CN-NO bi-cycle. Figure taken from [4].

Following the idea to use chlorine as medium to detect neutrinos suggested by Bruno Pontecorvo in 1946 [26], the first experiment to detect solar neutrinos was built in the Homestake gold mine in South Dakota in 1968. The neutrino absorption reaction used was:

$$\nu_e + {}^{37}\mathrm{Cl} \rightarrow \mathrm{e}^- + {}^{37}\mathrm{Ar}. \tag{1.11}$$

The energy threshold for this reaction is 0.814 MeV.

The first results from the Homestake detector showed a deficit of neutrinos. The rate of detected neutrinos was roughly 2.5 Solar Neutrino Units (SNU)[2] over an expected capture rate of 7.6 SNU. This discrepancy, known as Solar Neutrino Problem, remained unresolved for many years and was also confirmed by other experiments such as Kamiokande (and its successor Super Kamiokande) [16] and Gallex [27].

[2] A Solar Neutrino Unit is defined as the product of neutrino flux and the neutrino cross section. 1 SNU corresponds to 10^{-36} captures per target per atom per second.

The final answer to this dilemma came from Sudbury Neutrino Observatory (SNO) experiment [28]. The SNO experiment was able to detect the total flux of solar neutrinos of any flavor. In 2002, the SNO collaboration reported their results. The sum of all the fluxes for all the three flavors was consistent with the predicted electron neutrino flux. It was a confirmation of the observation of neutrino flavor oscillations already announced by Super-Kamiokande in 1998 [3] and the solar neutrino model.

1.2.3. High-energy astrophysical neutrinos

The production of high-energy neutrinos is expected by the interactions of accelerated cosmic rays with dense matter or photons field near the cosmic ray source. The dominant channels near the π production threshold for nucleon-photon interactions are

$$\begin{aligned} p + \gamma &\to \Delta^+ \to \pi^0 + p \\ p + \gamma &\to \Delta^+ \to \pi^+ + n. \end{aligned} \tag{1.12}$$

$$\begin{aligned} n + \gamma &\to \Delta^0 \to \pi^0 + n \\ n + \gamma &\to \Delta^0 \to \pi^- + p. \end{aligned} \tag{1.13}$$

Pions are also generated in nucleon-nucleon processes, such as:

$$\begin{aligned} p + p &\to p + p + \pi^0 \\ &\to p + n + \pi^+ \end{aligned} \tag{1.14}$$

$$\begin{aligned} p + n &\to p + n + \pi^0 \\ &\to p + p + \pi^-. \end{aligned} \tag{1.15}$$

The charged pions decay into neutrinos while the neutral pions decay into gamma rays:

$$\begin{aligned} &\pi^0 \to \gamma + \gamma \\ &\pi^+ \to \mu^+ + \nu_\mu \to e^+ + \nu_e + \bar{\nu}_\mu + \nu_\mu \\ &\pi^- \to \mu^- + \bar{\nu}_\mu \to e^- + \bar{\nu}_e + \nu_\mu + \bar{\nu}. \end{aligned} \tag{1.16}$$

At higher energies kaons can be produced which also decay into neutrinos. The four leptons emerging from the decay of the pion carry roughly the same fraction of the energy. As a consequence, each neutrino carries about $1/4$ of the pion's initial energy. Since for high-energy protons roughly 20% of the initial energy, E_p, is transferred to the pion, we obtain for the neutrino energy, E_ν, that $E_\nu = E_p/20$.

The flavor ratio[4] at the source is

$$\nu_e : \nu_\mu : \nu_\tau = 1 : 2 : 0. \tag{1.17}$$

[3] The fact that if neutrinos have non-zero masses, they could oscillate between flavors was first suggested by Bruno Pontecorvo in the 1950s.

[4] we do not make any distinction between neutrinos and anti-neutrinos

	π^+	π^0	ν_μ	γ	$x_{\nu/\gamma}$
p-p	$\frac{1}{3}$	$\frac{1}{3}$	$2{\cdot}\frac{1}{2}\cdot\frac{1}{4}\cdot\frac{1}{3}=\frac{1}{6}$	$\frac{1}{2}\cdot\frac{1}{3}=\frac{1}{6}$	1
	π^+/π^0	p/n	ν_μ	γ	$x_{\nu/\gamma}$
p-γ	$\frac{1}{3}$	$\frac{2}{3}$	$\frac{1}{2}\cdot\frac{1}{3}=\frac{1}{6}$	$2{\cdot}\frac{2}{3}\cdot\frac{1}{2}=\frac{2}{3}$	4

Table 1.1.: Fraction of the proton energy which goes to pions, muon neutrinos and photons in p-p and p-γ interactions.

Taking into account flavor oscillations, the resulting flavor ratio at Earth is approximately:

$$\nu_e : \nu_\mu : \nu_\tau \approx 1 : 1 : 1. \tag{1.18}$$

In case of sources with high magnetic fields the contribution from muon decay could be suppressed due to the loss energy by mesons and/or muons. The observed flavor ratio is then [30]:

$$\nu_e : \nu_\mu : \nu_\tau \approx 1 : 1.8 : 1.8. \tag{1.19}$$

Normalisation of the flux

In the discussed hadronic processes, both TeV photons and neutrinos are produced by the decay of neutral and charged pions respectively. Thus, it is possible to relate gamma-ray and neutrino fluxes by imposing simple energy conservation as [23, 24]:

$$\int_{E_\gamma^{\min}} \frac{dN_\gamma}{dE_\gamma} E_\gamma dE_\gamma = x_{\nu/\gamma} \cdot \int_{E_\nu^{\min}} \frac{dN_\nu}{dE_\nu} E_\nu dE_\nu, \tag{1.20}$$

where $E_\gamma^{\min}$ is the minimum energy of the photons with hadronic origin and $E_\nu^{\min}$ the minimum energy of the neutrinos. The constant of proportionality $x_{\nu/\gamma}$ depends on whether the neutral pions are of pp or $p\gamma$ origin and in particular on the fraction of energy which goes into pion production. In pp interactions $1/3$ of the proton energy goes into each pion flavor on average. The charged pion then decays into muons which decay into electrons. Two ν_μ are produced in these decays with $E_\pi/4$ energy for each photon with $E_\pi/2$. Hence, the energy in neutrinos is equal to the energy in photons [24] and $x_{\nu/\gamma} \sim 1$. In $p\gamma$ interactions $2/3$ of the proton energy goes to the neutrons (protons) and the remaining third goes to the positively-charged pions (neutral pions). In the charged pion decay a single ν_μ is created with half of the pion energy for every photon with half of the neutral pion energy. Thus, in this case $x_{\nu/\gamma} \sim 4$. Table 1.1 summarises it.

Neutrino effective area

For a neutrino flux dN_ν/dE_ν at the Earth, the event rate can be computed from the "effective area":

$$R_\nu(\delta_\nu) = \frac{dN_\nu(\delta_\nu)}{dt} = \int dE_\nu A_\nu^{\rm eff}(E_\nu, \delta_\nu)\frac{dN_\nu}{dE_\nu}, \tag{1.21}$$

where $A_\nu^{\rm eff}(E_\nu, \delta_\nu)$ is the neutrino effective area, i.e. the equivalent area of a 100% efficient detector, which depends on both the neutrino energy, E_ν, and the source declination δ_ν. The neutrino effective area, which is computed via Monte Carlo simulation, takes into account the neutrino charged current cross section (see next chapter), $\sigma_\nu(E_\nu)$, the absorption of neutrinos through the Earth, $\mathrm{P_{Earth}(E_\nu)}$ and the muon detection (and selection) efficiency, ϵ, in the generation volume $V_{\rm gen}$:

$$A_\nu^{\rm eff}(E_\nu, \delta_\nu) = \epsilon \times V_{\rm gen} \times \rho \times N_{\rm A} \times \sigma_\nu(E_\nu) \times \mathrm{P_{Earth}(E_\nu)}, \tag{1.22}$$

with ρ the material density and $N_{\rm A}$ the Avogadro number. The neutrino survival probability $P_{\rm Earth}$ can be written as:

$$\mathrm{P_{Earth}} = \mathrm{e}^{-\mathrm{N_A}\sigma_\nu(\mathrm{E_\nu})\int \rho(\mathrm{l})\mathrm{dl}} \tag{1.23}$$

for a neutrino propagating through paths of density $\rho(l)$. The neutrino effective area for the ANTARES detector is shown in Figure 1.7 as a function of E_ν for three declination bands.

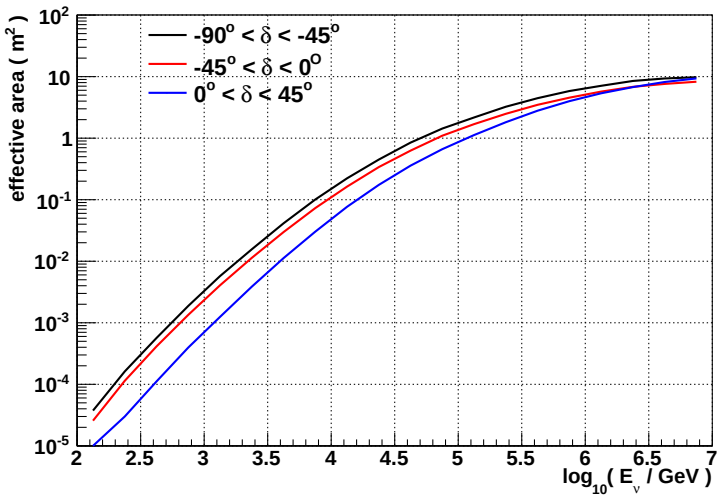

Figure 1.7.: Neutrino effective area of the ANTARES detector for the period 2007-2010 as a function of the neutrino energy for three declination bands.

1.3. Candidate sources of cosmic neutrinos

In this section possible sources of cosmic rays and neutrinos are presented. A distinction between Galactic and extragalactic sources is made. A sky-map showing the location in Galactic coordindates for some of these γ-ray sources is shown in Figure 1.9.

1.3.1. Visibility at the ANTARES site

The location of the ANTARES detector in the Mediterranean Sea makes it suitable to detect potential Galactic sources of neutrinos. Figure 1.9 shows that most of the Galactic Plane is visible for ANTARES which is sensitive to upgoing neutrinos, i.e. below the local horizon (θ <90, where θ is the zenith angle). A source at declination δ which emits neutrinos required to be as upgoing by a detector at latitude ϕ, is visible for a fraction of the day [32]:

$$f = 1 - \frac{\arccos(-\tan\delta\tan\phi)}{\pi}. \tag{1.24}$$

For example, the Galactic Center ($\delta = -29°$), which is never visible at the South Pole, has $f \approx 67\%$ at the ANTARES site ($\phi \approx 42°50^{'}$). The SNR RX J1713.7-3946, one of the brightest TeV sources, is located at $\delta = -39.75°$ and is visible at the ANTARES site for 78% of the time. Figure 1.8 (top) shows the quantity f as a function of the detector latitude for various Galactic sources. The visibility as a function of the source declination is shown in Figure 1.8 (bottom)

1.3.2. Galactic sources

During the last decade many Galactic TeV gamma-ray sources have been discovered using atmospheric Cherenkov telescopes such as H.E.S.S. [33, 34], VERITAS [35] and MAGIC [36]. Today, the TeV source catalogue comprises more than 100 objects[5]. For many sources the question whether the observed gamma-ray flux is produced leptonically, i.e. via inverse Compton scattering, or hadronically, through the reactions described in 1.2.3, is still open.

The most promising Galactic candidate ν sources are:

- **Shell-type supernova remnants.** A supernova is a stellar explosion which ejects most of the stellar material at a velocity up to 30.000 km/s. Shock waves are generated by the interaction of the matter ejected with the interstellar medium. They could result in particle acceleration via the Fermi mechanism. The interactions of the accelerated cosmic rays with the local matter of the remnant create neutrinos and gamma-rays via decay of charged and neutral pions. Two of the most famous examples of shell-type supernova are Vela Jr.(RX J0852.04622) and RX J1713.3946-7. TeV gamma-rays have been observed from both sources [37, 38]. Predictions of neutrino emission from RX J1713.3946-7 are discussed in the next chapter.

[5] see for example the online TeV gamma-ray catalog TeVCat at http://tevcat.uchicago.edu

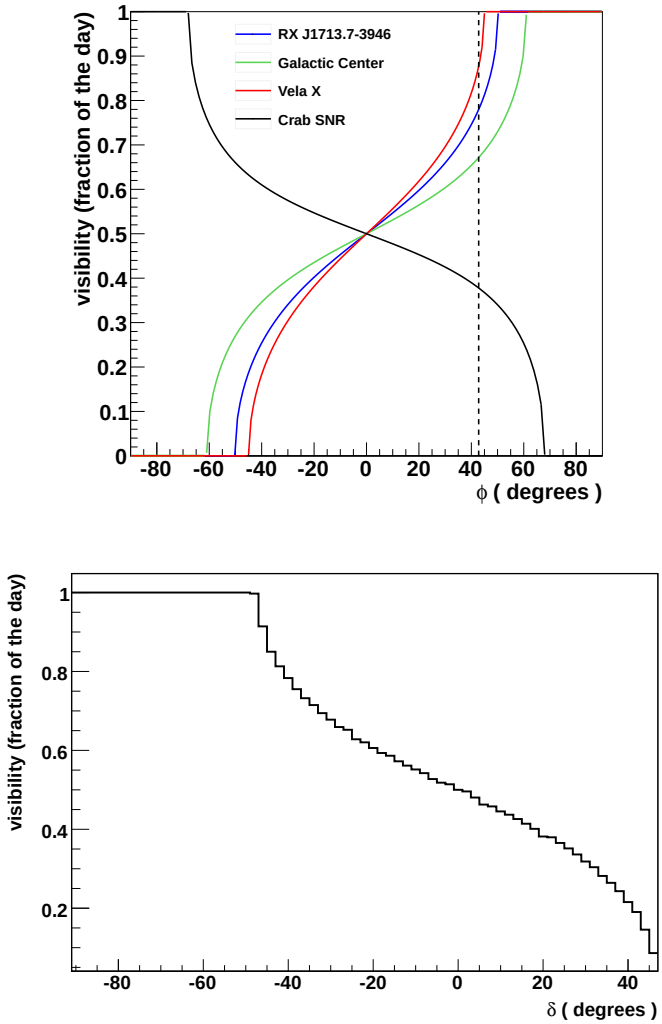

Figure 1.8.: Top: fraction of time a source is visible from a detector at latitude ϕ. The dashed line shows the ANTARES location. Bottom: visibility at the ANTARES site as a function of the source declination.

In February 2013, the Fermi-Lat [40] collaboration provided the first evidence that cosmic ray protons are accelerated in supernova remnants (SNRs) [41]. GeV gamma-rays from SNRs associated with giant molecular clouds, W 44 and IC 443, were detected. At GeV energies hadronic models fit the data better the leptonic ones. The γ-ray spectra of these two sources are shown in Figure 1.10. Both sources are investigated in the point source analysis described in this thesis.

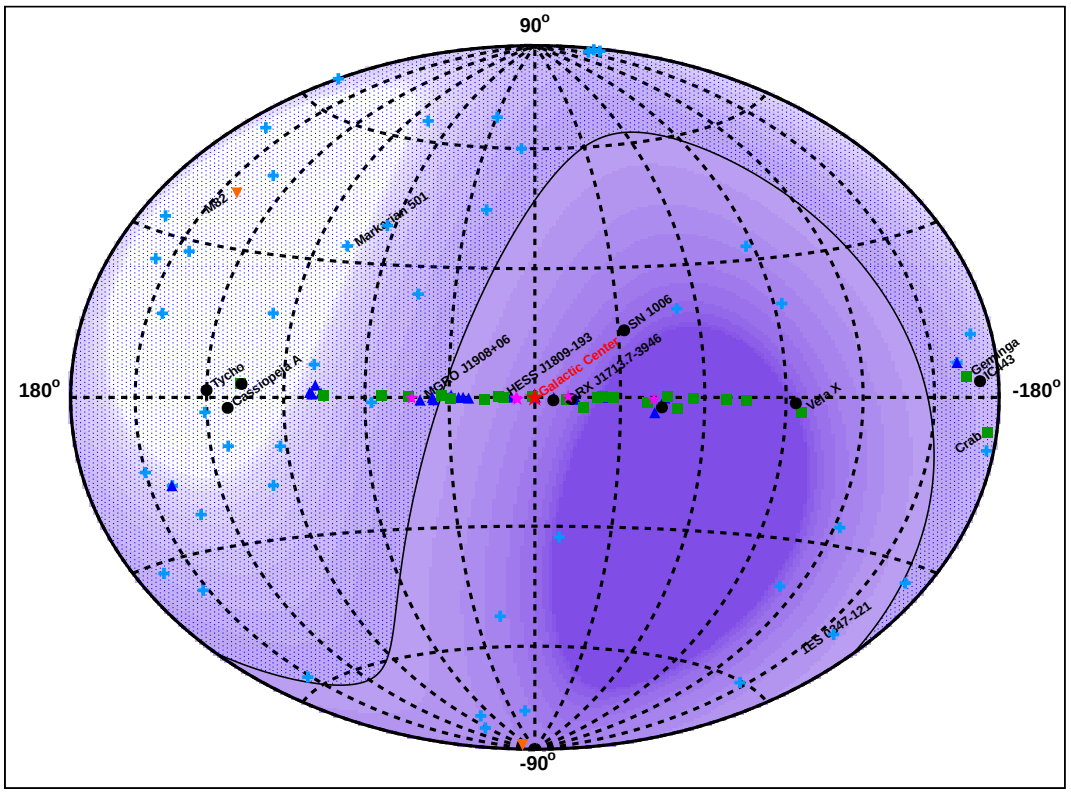

Figure 1.9.: Sky map in Galactic coordinates of TeV γ-ray sources. Different symbols represent different source types: black circles for shell type supernovae, magenta stars for supernovae remnants and molecular clouds, green squares for pulsar wind nebulae, orange triangles for starburst galaxies, blue cross for AGNs and blue triangles for unidentified sources. The red star represents the Galactic Center. The solid line shows the extend of the visibility for a South Pole detector. The visibility in ANTARES is indicated by the different shades of purple.

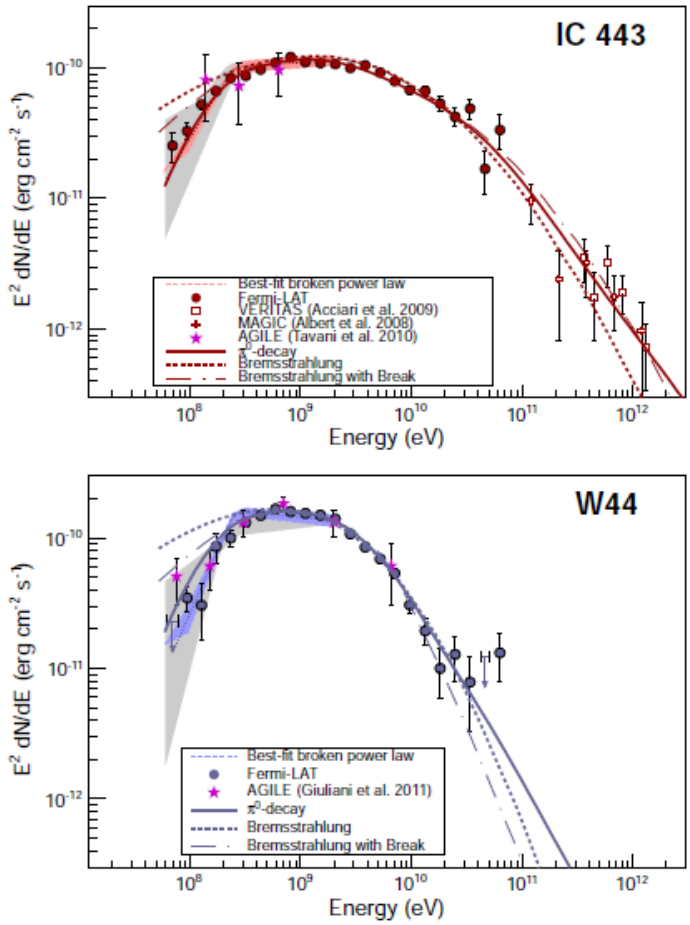

Figure 1.10.: Gamma-ray spectra of the SNRs IC 443 (top) and W44 (bottom) measured by Fermi-LAT. The solid lines denote the smoothly broken power-law function used for the fit which is based on a hadronic model. The dashed lines show the same but for a leptonic model. For IC 443 the TeV data points from MAGIC, VERITAS and H.E.S.S. are also shown.

- **Pulsar wind nebulae.** Pulsar wind nebulae (PWN), also known as plerions, are a sub-class of supernova remnants characterised by the presence of a central pulsar blowing out a "wind" of electrons and positrons into the nebula. The acceleration of cosmic rays may take place at shocks in the pulsar wind. The most famous PWN is the Crab Nebula which was the first TeV γ-ray source ever detected [39]. Another TeV γ-ray plerion is Vela X [42]. In the next chapter we will describe models of neutrino emission from these two sources.

- **Microquasars.** Microquasars are Galactic X-ray binary systems. They are usually characterised by relativistic radio jets. They consist of a compact object, such as a neutron star or a black hole, which accretes matter from a companion star usually of smaller mass. The X-ray emission can be separated into a thermal component, produced by the accretion disk, and a power law component which is generated by Compton scattering of soft photons on a gas of hot electrons. Neutrinos can be generated by the interactions of accelerated protons with synchrotron photons produced inside the jet by thermal electrons. TeV gamma-rays have been detected by H.E.S.S. for the microquasars LS 5039 [43] and LSI $+61°303$ [44]. In [45] neutrino fluxes and event rates from microquasars are predicted. The model discussed is based on the assumptions that the jets are protonic[6]. Upper limits on these models were recently obtained by the ANTARES collaboration [46].

- **Galactic center.** The H.E.S.S. telescope has observed a point-like source of very high-energy gamma rays (HESS J1745-290) [47] in the direction of the central region of our Galaxy. The source of this emission could be either the supermassive black hole Sagittarius A* or the supernova remnant (SNR) Sgr A East. Unfortunately the angular distance between these two objects is smaller than the detector angular resolution. A second observation revealed another source (HESS J1747-281) located at the same coordinates of the supernova remnant G 0.9+0.1 [48]. Recently a diffuse gamma-ray emission of energies greater than 100 GeV was discovered [49] in a very large region which spans the Galactic coordinates $|l| < 0.8°$, $|b| < 0.3°$. The measured gamma-ray flux is well described by a power lay spectrum $dN_\gamma/dE \propto (E/TeV)^{-2.29}$. Considering the morphological correlation between the high density ($n_{\rm H} \sim 10^4$ cm^3) of molecular clouds in the region and the gamma-ray emission, the only reasonable mechanism of photons production is via meson decay, thus a neutrino flux is also expected [50]. The excess of gamma-rays detected by H.E.S.S. is shown in Figure 1.11.

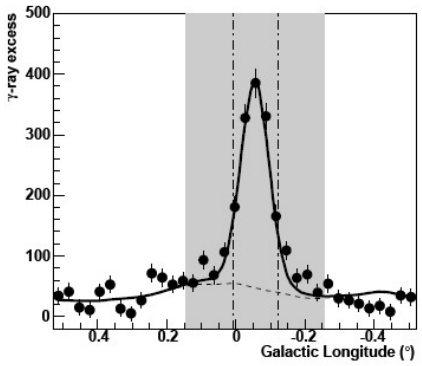

Figure 1.11.: γ-ray excess as a function of Galactic longitude. A strong emission at the Galactic center is clearly visible as well as a diffuse emission at larger longitude values. The dashed-dotted lines show the 68% containment region of the point spread function of the instrument.

- **Fermi bubbles.** The Fermi bubbles are two large bubbles extending north and south

[6] Jets dominated by electro-proton plasma.

of the Galactic center for approximately 25 thousands light years emitting gamma-rays. They were recorded for the first time in November 2010 by the Fermi-LAT detector [12]. The energy spectrum spans from 1 GeV to $\sim$ 100 GeV. Several mechanisms have been suggested in order to explain this gamma-ray emission, most of them involving leptonic processes. However, some models describe also a possible hadronic scenario via collisions of accelerated protons with a neutrino flux as consequence [51].

1.3.3. Extragalactic sources

In the following, the most promising candidate source of extragalactic neutrinos are summarised:

- **Active Galactic Nuclei.** AGN are galaxies hosting a supermassive black hole ($10^6 - 10^9$ solar masses) at their center. AGN release a large amount of energy, $L > 10^{47}\mathrm{erg/s}$, provided by the accretion of matter by the supermassive black hole. Two relativistic jets are emitted perpendicular to the accretion disk, transporting matter. A subclass of AGN is represented by the so called blazars in which the jet axis is aligned along the line of sight of an observer.

  AGNs have been observed in all frequency bands, from radio up to TeV energies.

  Many models predict neutrino emission from the relativistic jets [53, 52, 54] where the accelerated protons can interact with synchrotron photons. Protons are accelerated by shock fronts created by plasma blobs moving with different speeds. The diffuse neutrino flux predicted by these models is computed by convoluting the single source flux with the redshift and luminosity dependent number of sources, dn/dL, as:

  $$\frac{dN_\nu}{dE_\nu} \propto \int_z \int_L dL dz \frac{d\Phi_\nu}{dE_\nu}(L,z) \cdot \frac{dn}{dL}(L,z). \tag{1.25}$$

  The overall normalisation of the neutrino spectra depends on the observed gamma-ray flux. The model proposed by [53] is based on a possible correlation between the emission of X-rays and neutrinos. The prediction from Halzen and Zas [52] takes into account the results from the EGRET collaboration [64]: the diffuse extragalactic background measured by EGRET ($E_\gamma > 100$ MeV) can be interpreted as the result of interactions between TeV photons from AGNs with nucleons in the source. The normalisation of the neutrino flux proposed in [54] assumes that the neutrino emission from a single AGN is correlated to the radio luminosity.

  The flux predicted from these models has been experimentally rejected by the recent analyses from the IceCube and ANTARES collaboration [56, 57] as shown in Figure 1.14. This indicates that the assumptions made in the mode are wrong or too optimistic. For example in [54] several neutrino models from radio galaxy are discussed for different spectral shapes of the primary proton cosmic ray spectrum and optical thickness of the source. The upper limit obtained by IceCube rejects only the model with a primary cosmic ray spectrum of E^{-2} and an optical thickness $\tau = 0.2$.

- **Gamma-ray bursts.** GRBs are short but extremely energetic bursts of gamma radiation (KeV-MeV photons). The initial burst is often followed by X-ray, optical and radio emission, i.e. the so called "afterglow". GRBs are commonly divided in two categories depending on their duration. "Long" GRBs last for more than 2 seconds and have an average duration of 30 seconds while "short" GRBs last for less than 2 seconds. It is thought these correspond to different progenitors: "long" GRBs are often associated with supernovae as was first indicated by the observation of GRB980425 on April 25, 1998 and later confirmed by its coincidence in time and space with the supernova SN 1998bw [65]. "Short" GRBs are instead associated with binaries system with a small fraction of a solar mass of matter accreting on a massive black hole.

  The most widely accepted theory to describe the physics of GRBs is the "fireball" model. A "fireball", produced either during the collapse of a supernova or the merger of a binary system, expands at relativistic velocity. Cosmic rays are thought to be accelerated in the fireball internal shocks, hence neutrinos are produced in the decay of charged pions created in the interactions of protons with local photons. Two models of neutrino emission [66, 67], which assume that all UHECR are produced in GRBs, have been rejected by the IceCube collaboration [68] in a search of neutrinos from GRBs. The upper limits are a factor 3.7 below these predictions. From these results, shown in Figure 1.12, the conclusion seems that the current theories and neutrino production in GRBs have to be revisited. As a result, gamma-ray bursts are not a primary source of ultra high-energy cosmic rays.

- **Starburst galaxies.** Starburst galaxies are characterised by a very high rate of star formation often triggered by the galaxy merger mechanism. As a consequence a high rate of supernova explosions is also expected. Supernovae will therefore enrich the dense star forming region with relativistic cosmic rays accelerated in front shocks. Hence, neutrinos will be produced by the decay of charged pions generated by the interactions of relativistic protons with the interstellar medium. In [58], a flux of neutrinos from supernova remnants in starburst galaxies is predicted. The flux derived follows a power-law spectrum with an exponential cutoff. A few events per year are predicted for a kilometer scale detector. This theoretical model has been tested by a stacking search performed by the IceCube collaboration [59] using data from a partially completed detector. Upper limits have been derived.

- **Galaxy clusters.** Cluster of galaxies (GCs) are the largest gravitationally bound objects in the universe and represent a potential source of high-energy cosmic rays. Neutrinos are generated through pp interactions with the intracluster material. Neutrino fluxes for five nearby ($z < 0.03$) GCs (Virgo, Centaurus A, Perseus, Coma and Ophiuchus) are derived in [60]. The calculated event rate is shown in Figure 1.13 for a kilometer-cube detector. A few events per year are expected.

Upper bounds to the neutrino flux from Extragalactic sources

Ultra high-energy cosmic rays ($E > 10^{18}\mathrm{eV}$) are believed to have an extragalactic origin as their Larmor radius exceeds the size of the Galaxy. An upper bound to the neutrino flux

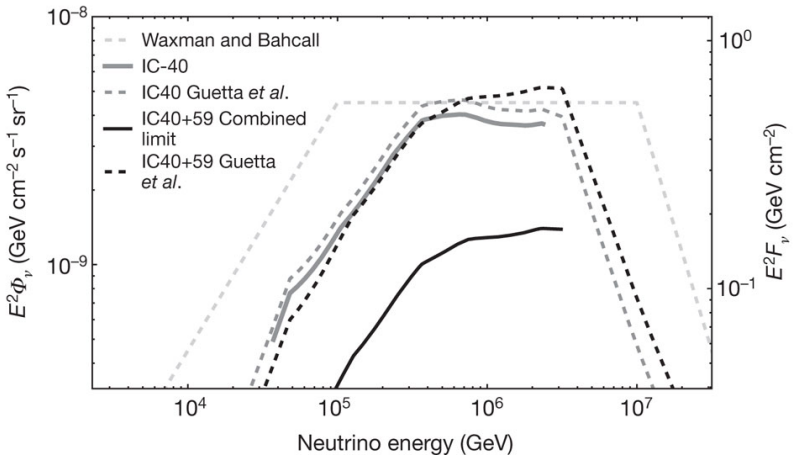

Figure 1.12.: Predictions from [66, 67] for neutrinos from GRBs are shown in dashed lines as a function of the neutrino energy. The dashed line labelled as "IC40 Guetta *et al.*" shows the flux prediction for IceCube using only 40 strings. The black dashed line labelled as "IC40+59 Guetta *et al.*" shows the prediction for the full data set of the analysis. Solid lines refer to 90% CL upper limit, with the the grey line labelled as "IC40 limit" showing the results from a previous analysis [69] and the black line labelled as "IC40+59 Combined limit" showing the final results. Figure taken from [68]

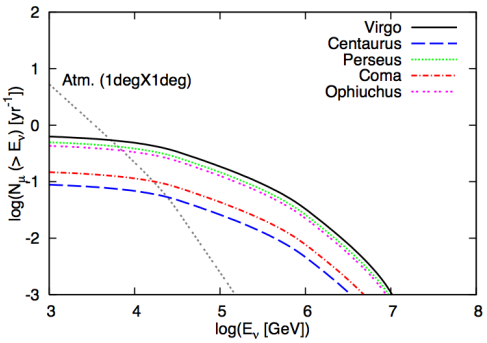

Figure 1.13: Expected event rates for muon neutrinos in a kilometer-cube detector from five GCs: Virgo, Centaurus A, Perseus, Coma and Ophiuchus. Figure taken from [60]

from extragalactic sources was estimated by Waxmann and Bahcall [61, 62]. The model applies in particular to Active Galactic Nuclei (AGNs) and Gamma-Ray Bursts (GRB) and relies on cosmic ray observations (the observed spectrum of UHECRs was used as a normalisation factor to their calculations). The upper limit is $E_\nu^2 \Phi_\nu < 4.5 \times 10^{-8} \mathrm{GeV cm^{-2} s^{-1}}$. The limit derived by Waxmann and Bahcall (WB) is based on assumptions which have been criticised [63]:

1. Neutrons generated in photohadronic interactions escape from the source.
2. Magnetic fields do not play any role in the propagation of CRs.
3. The injection spectrum is $\propto E^{-2}$.

In [63] instead, a bound has been derived directly not only from the CRs observation (as in the case of Waxmann and Bahcall) but also from the gamma-ray flux observed by EGRET [64]. The bound discussed in [63] is in general in agreement with the WB limit in the neutrino energy range $10^7 \mathrm{GeV} \leq \mathrm{E}_\nu \leq 10^9 \mathrm{GeV}$ but is higher at lower and higher energies. Both the bound predicted in [63] and by Waxmann and Bahcall are shown in Figure 1.14.

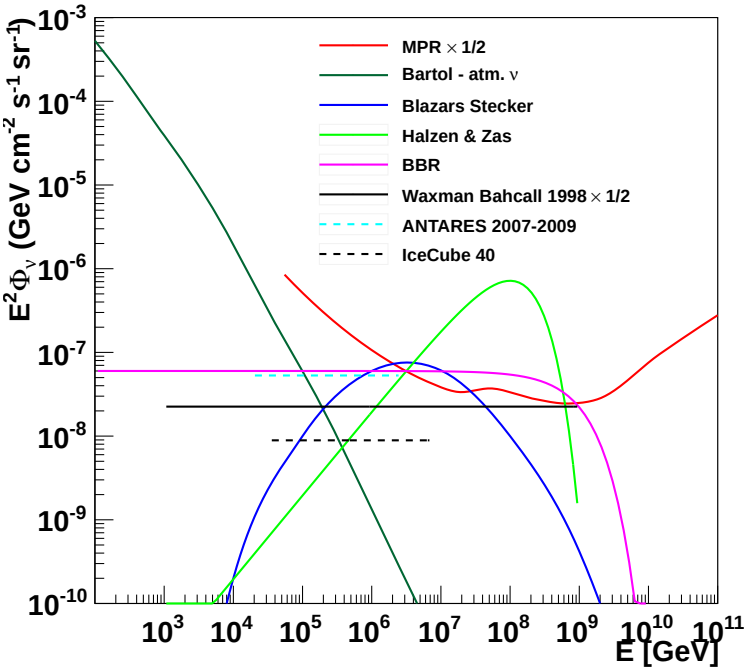

Figure 1.14.: Various predictions for the diffuse neutrino flux from AGNs together with the WB bound (solid black line) and the Mannheim, Protheroe and Rachen [63] (MPR) (solid red line). To take into account neutrino oscillations from the source to the Earth they are both divided by two. The solid green line shows the diffuse neutrino flux predicted by Halzen and Zas in 1997 [52]. The solid blue line the model by Stecker [53] for blazars and the magenta line the model by Becker, Biermann and Rhode (BBR) in 2005 [54]. The solid dark green line shows the atmospheric neutrino flux as parametrised in [55] (averaged over all ν_μ directions). Upper limits from ANTARES [57] (dashed light blue line) and IceCube [56] (dashed black line) are also shown.

2. Models of astrophysical neutrino emission from Galactic sources

It doesn't matter how beautiful your theory is, it doesn't matter how smart you are. If it doesn't agree with experiment, it's wrong.

Richard P. Feynman

In Chapter 1 we presented potential sources of neutrinos. Here we will focus on Galactic objects and in particular on supernova remnants (SNRs) which are thought to produce the Galactic cosmic rays. In the following sections the sources shown in Figure 1.8 together with theoretical models for neutrino emission from them are discussed. First, a small review of the TeV gamma-ray astronomy is presented to elaborate on the strong connection between the emission of TeV gamma-rays and neutrinos.

2.1. Intermezzo: gamma-ray astronomy

Gamma-ray astronomy covers a very large energy range, namely from low ($<$ 30 MeV) to high (100 MeV - to 50 GeV) and very high (50 GeV - 100 TeV) energies. Due to the opacity of the Earth's atmosphere, the low energy gamma-rays are detected with spaced-based experiments. Unfortunately, satellites can host only relatively small detectors (effective area $\leq 1\ \mathrm{m}^2$). Currently, two gamma-ray satellites are operating: AGILE [70] and Fermi-LAT [40]. The latest catalog of GeV gamma-rays sources released by the Fermi-LAT collaboration contains 1873 sources [71]. Many of these source are not associated with any counterpart in visible light.

At TeV energies, gamma-rays are detected by ground-based imaging atmospheric Cherenkov telescopes (IACTs). IACTs detect the Cherenkov light emitted by charged particles in electromagnetic air showers created by the primary gamma-rays hitting the atmosphere. The three main IACTs are H.E.S.S., MAGIC and VERITAS.

There are about 80 known TeV sources within our Galaxy. Most of them were discovered during the H.E.S.S. survey of the inner Galaxy [72].

2.1.1. Gamma-ray production

In general the light emitted by celestial objects can be divided into two main categories, namely thermal and non-thermal radiation. Thermal radiation is produced by the thermal motion of charged particles in matter. All matter with a temperature above the absolute

zero emits thermal radiation. The most important processes which produce non-thermal radiation are:

- **Synchrotron radiation.** The emission of radio or x-ray photons from electrons moving in a magnetic field.
- **Inverse Compton (IC).** Low energy photons are scattered by relativistic electrons to higher energies.
- **Neutral pion decay**. π^0 mesons produced in p-γ or p-p interactions decay into photons. The π^0 lifetime is $\tau \sim 10^{-16}$ (see Equations 1.14,1.12 for p-p and p-γ interactions and 1.16 for pions decay). The energy of each photon is $m_{\pi^0}c^2/2 = 67.5$ MeV in the rest frame of the π^0.

The first two processes are purely leptonic, i.e. accelerated electrons are responsible for the gamma-ray emission. Hadronic processes such as π^0 production can also be responsible for the VHE photon emission and are associated with the production of neutrinos due to the charged pions decay.

Figure 2.1 illustrates the predicted Spectral Energy Distribution (SED) for the three processes. Two pronounced humps are visible. The first one at X-ray energies (keV), the second one around a few TeV. Synchrotron radiation is responsible for the low-energy hump. The spectrum due to synchrotron radiation follows a power-law function of which the spectral index depends on the energy spectrum of the parent electrons. The high-energy part of the SED is due to (a combination of) IC scattering and π^0 decay. In many leptonic models, the photons produced by synchrotron radiation are the seed photons for the IC process. This is known as self-synchrotron Compton (SSC) emission scenario. The simplest SSC models involve a single population of relativistic electrons emitting synchrotron radiation in radio and X-ray energies and IC photons from X-rays to gamma-rays. Assuming an electron spectrum proportional to $E^{-\alpha}$, in the non-relativistic regime (Thomson limit, $E_e E_\gamma \ll m_e^2 c^2$) the IC scattering produces in the TeV region a flatter spectrum with spectral index $(\alpha+1)/2$ [73]. In the ultrarelativistic domain (Klein-Nishina limit, $E_e E_\gamma \gg m_e^2 c^2$) the spectrum is steeper with index $\alpha + 1$.

The π^0 decay spectrum, dN_γ/dE_γ, is symmetric around 67.5 MeV in a log-log representation (pion-bump). In the SED distribution, $E_\gamma^2 dN_\gamma/dE_\gamma$, it rises steeply below $\sim$ 200 MeV and approximately follows the energy distribution of the parent protons up to energies greater than a few TeV with the same spectral index. The difference in the normalisation between the π^0 decay and the IC scattering spectrum is mainly due to source properties such as, for SNRs, the magnetic field and the proton density, $n_{\rm H}$. Ellison et al. [74] showed that the π^0 decay flux increases more rapidly with $n_{\rm H}$ than the IC flux. More quantitatively, at 1 TeV the ratio between the number of photons due to pion decay and the number of IC photons, $n_\gamma^\pi/n_\gamma^{\rm IC}$, is 0.01 for $n_{\rm H} = 0.01$ cm^{-3} and 0.65 for $n_{\rm H} = 1$ cm^{-3}. A proton density greater than 1 cm^{-3} yields a ratio $(n_\gamma^\pi/n_\gamma^{\rm IC})_{1\rm TeV} > 1$.

Figure 1.10 shows the energy spectrum for the two SNR which were identified as sources of cosmic rays by the FERMI-LAT collaboration. The GeV gamma-ray data are well fitted by an hadronic model while the leptonic models do not match the data. In the leptonic models discussed in the paper the values of the local magnetic field and the ambient gas

density are chosen to fit both the synchrotron radio and the gamma-ray flux[1]. The low-energy breaks found in data for energies below 200 MeV is not explained by these models, even when assuming an additional low-energy break in the electron spectra to make the gamma-ray spectra below 200 MeV as hard as possible.

The discovery of TeV gamma-ray emitters represents the first step towards the identification of cosmic ray sources (provided that is possible to disentangle the hadronic contribution from the IC). Multi-wavelength observations of the source, from the radio energies to the TeV domain, can contribute to the identification.

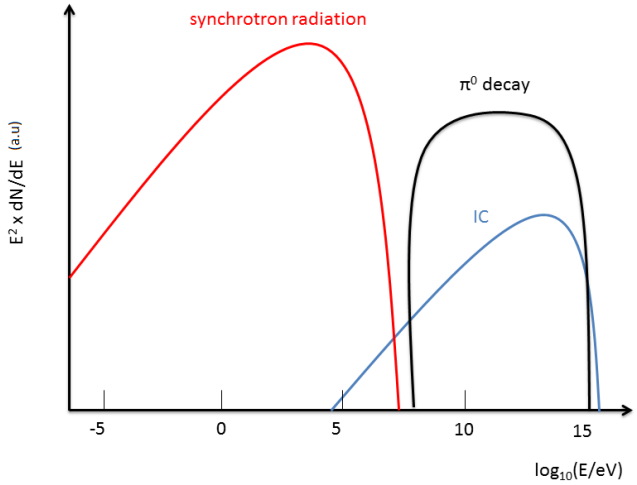

Figure 2.1.: Spectral energy distribution for synchrotron radiation, inverse compton and π^0 decay.

In the next sections we will focus on three Galactic candidate sources of neutrinos. For each of them three neutrino emission models will be discussed. Flux parameters and event rates are reported in Table 2.1.

2.2. RX J1713.7-3946

RX J1713.7-3946 (also known as G347.3-0.5) is a supernova remnant associated with a core collapse supernova which exploded in the constellation of Scorpius in 393 A.D. [75]. It is 1 kpc far from the Earth [76] and has an angular diameter of roughly 1° with a shell of ~ 20 pc size. It was first discovered in the X-rays by ROSAT [77]. Its X-ray spectrum

[1] Due to bremsstrahlung.

is completely dominated by synchrotron emission [78] with very faint thermal X-ray and radio emission.

RX J1713.7-3946 is better known for being the first SNR for which TeV gamma-rays were clearly detected [79]. A detailed campaign from H.E.S.S. revealed indeed a bright TeV gamma-ray emitter with an energy spectrum measured up to 10 TeV and well described by a power law with spectral index of 2.2 [38]. The gamma-ray morphology of RX J1713.7-3946 is shown in Figure 2.2

The main open question regarding RX J1713.7-3946 is the origin of its TeV gamma-rays. A hadronic mechanism would reveal a connection between TeV gamma-ray photons and accelerated protons via the decay of pions, while a leptonic mechanism would suggest that the TeV emission is caused by inverse Compton scattering of the photon fields near the remnant by the same relativistic electrons that are responsible of the X-ray emission. In this regard, the recent results published in 2011 by the Fermi-LAT collaboration [81] are of particular importance since they collected data in the energy range (500 MeV to 400 GeV) which closes the gap between X-ray satellites measurements and TeV gamma-ray telescopes. Figure 2.3 (top) shows the energy spectrum measured by Fermi-LAT at low energies and H.E.S.S. at high energies. The hard spectrum in the energy range 1-100 GeV agrees with leptonic models describing the gamma-ray emission as consequence of IC scattering (see also Figure 2.1). Pure hadronic models seems to be disfavored by these measurements as can be inferred by Figure 2.3 (bottom). In particular, the lack of thermal X-ray emission yields a small proton density in the SNR since the main sources responsible for the heating of the electrons are Coulomb collisions between electrons and protons [74]. However, the good agreement between Fermi-LAT data and leptonic processes models does not mean that protons are not accelerated in this SNR and an hybrid scenario (leptonic and hadronic) [82] can not be ruled out. The proton spectral index that can be inferred from the LAT data is $\alpha =\sim 1.5$ a value which is as small as the asymptotic limit of $\alpha = 1.5$ predicted for extremely efficient CRs acceleration [83]. Recently Inoue et al. [84] showed that the X-ray thermal emission could suppressed by molecular clouds which stall the accelerated shock wave. The interaction between the accelerated CR protons and the protons of the clouds could produce neutral pions. The derived photon index of the hadronic gamma-rays is consistent with the FERMI-LAT observations.

2.2.1. Neutrino emission from RX J1713.7-3946

In the last decade many theoretical models to describe neutrino emission from RX J1713.7-3946 have been developed. We consider three recent models proposed after the latest H.E.S.S. measurements. In these models, a similar neutrino spectrum which follows a power-law distribution with exponential cut-off is obtained:

$$\frac{dN_\nu}{dE_\nu} = k_\nu (\frac{E_\nu}{1\mathrm{TeV}})^{-\Gamma_\nu} \exp(-\sqrt(E_\nu/E_{c,\nu})). \tag{2.1}$$

The values of the flux normalisation, k_ν, the spectral index, Γ and the cut-off energy $E_{c,\nu}$ for each of these models are reported in Table 2.1.

- **Kistler and Beacom (2006).** The authors of [50] present a model based on the measured parameters of the gamma-ray spectrum for various Galactic sources. The

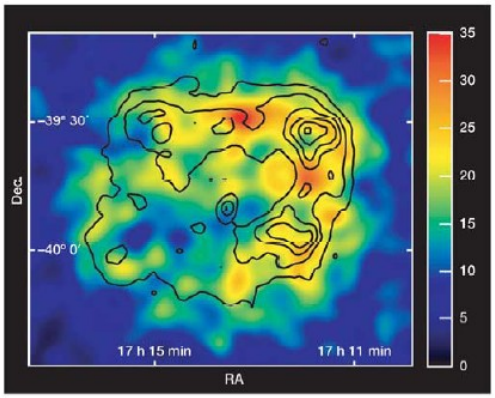

Figure 2.2.: Gamma-ray image of the SNR RX J1713.7-3946. Figure taken from [38].

following assumptions were made:

1. The gamma-ray and the neutrino flux share the same spectral index Γ (2.2 for RX J1713.7-3946 as reported in [38]).
2. In p-p interactions, for equal pion multiplicities each photon from π^0 decay corresponds to a neutrino from $\pi^{\pm}$ decay. The energy of these neutrinos is roughly half of the photon energy. The resulting neutrino spectrum is then shifted, relative to the gamma-ray spectrum and

$$\frac{dN_\nu}{dE_\nu} = k_\nu E_\nu^{-\Gamma} = (\frac{1}{2})^{\Gamma-1} k_\gamma E_\nu^{-\Gamma} \tag{2.2}$$

   thus, the relation between the gamma and neutrino flux normalisation is given by:

$$k_\nu = k_\gamma (\frac{1}{2})^{\Gamma-1}, \tag{2.3}$$

   with $k_\gamma = 15 \times 10^{-12} \mathrm{TeV}^{-1} \mathrm{cm}^{-2} \mathrm{s}^{-1}$ (as reported in [38]).
3. The neutrinos are assumed to cut-off at half the observed gamma cut-off, i.e. $E_{c,\nu} = 0.5 \cdot E_{c,\gamma}$ (for RX J1713.7-3946 $E_{c,\nu} = 50$ TeV).

- **Kappes et al. (2007).** A neutrino emission model which can be applied to most of the known Galactic sources is proposed in [95]. Parametrisations of simulated energy spectra of pions and secondary particles produced in inelastic proton- proton collisions are presented in [96]. These parametrisations are used to calculate the relationship between gamma-ray and neutrino spectra. The primary proton spectrum is given by a power law with spectral index Γ and exponential cut-off energy $E_{c,p}$:

$$\frac{dN_p}{dE_p} = k_p (\frac{E_p}{1\mathrm{TeV}})^{-\Gamma_p} \exp(-\frac{E_p}{E_{c,p}}). \tag{2.4}$$

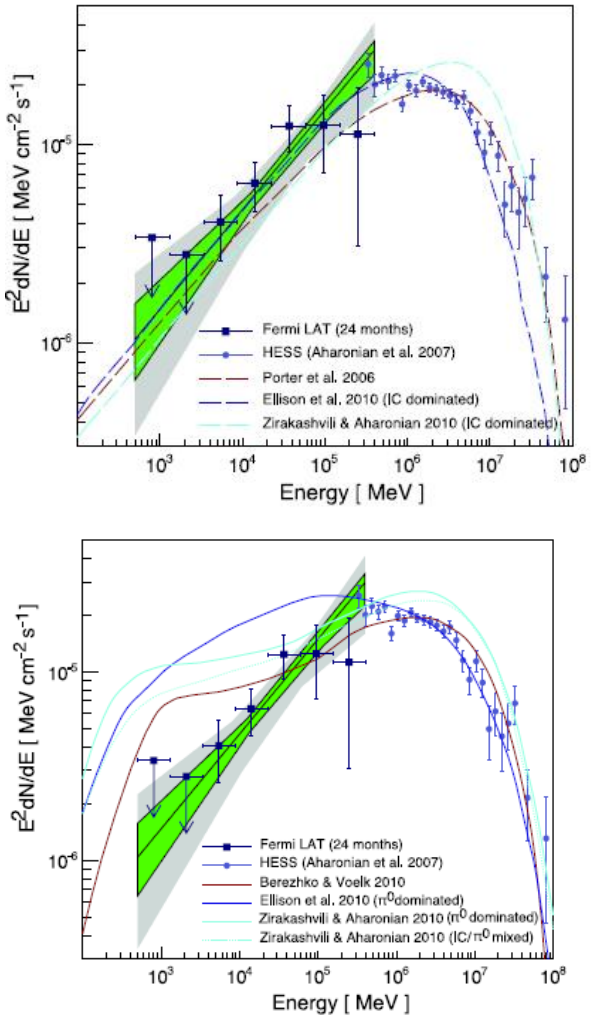

Figure 2.3.: Energy spectrum of RX J1713.7-3946 with data from Fermi-LAT and H.E.S.S. [38]. The top plot features predictions where the photons are produced via the leptonic mechanism. The bottom plot shows several models where the photons are generated via the hadronic mechanism. Fermi-LAT data agrees with emission scenarios in which the dominant source of emission is IC scattering. Both figures are taken from [81].

The resulting γ-ray and neutrino spectra follows the function given in Equation 2.1 with:

$$\begin{aligned} k_\nu &\simeq (0.71 - 0.16\Gamma_p)k_\gamma \\ \Gamma_\nu &\simeq \Gamma_\nu \simeq \alpha - 0.1 \\ E_{c,\nu} &\simeq 0.59 E_{c,\gamma} \simeq E_{c,p}/40 \end{aligned} \tag{2.5}$$

For RX J1713.7-3946 the flux normalisation $k_\nu = 15 \times 10^{-12}\mathrm{TeV}^{-1}\mathrm{cm}^{-2}\mathrm{s}^{-1}$, the spectral index $\Gamma_\nu = 1.72$ and the energy cut-off $E_{c,\nu} = 1.35\,\mathrm{TeV}$.

Several assumptions are made in these calculations. Among them we emphasize the following:

1. The radiation and the matter densities of the source are sufficiently low for the photons to escape without interacting. This also means that the charged pions and the muons decay before interacting (matter density low) and that p-γ interactions are neglected (radiation density low).
2. Muons decay without losing a significant fraction of the energy. This is possible only for low magnetic fields (B $\sim$ few μG).
3. A total neutrino mixing occurs $(\nu_e : \nu_\mu : \nu_\tau) = (1{:}1{:}1)$

For RX J1713.7-3946 all these assumptions seem reasonable.

- **Morlino et al. (2009).** Unlike the previous models, the one described in [97] is based on a non linear diffuse shock acceleration (NLDSA) approach. The idea behind the NLDSA theory is to overcome one of the main problems of the so-called *test particle* approximation of particle acceleration in collisionless shocks. In the first order Fermi mechanism, a fraction of the kinetic energy of the moving stream has to be transferred to the accelerated particles, a clear contradiction of the assumption that the accelerated particles are test particles [98]. The fact that the spectrum is described by a power law is a consequence of this assumption. In NLDSA theory a dynamical backreaction of the accelerated particles on the shock is assumed: the pressure of the accelerated particles affects the shock dynamics [97, 99]. This leads to a shape of the spectrum of the accelerated particles which is not a simple power law but rather a more complicated one that can be as hard as $p^{-3.2}$ for high momenta p of the accelerated particle.

  The neutrino flux derived has $k_\nu = 3.01 \times 10^{-14}\mathrm{GeV}^{-1}\mathrm{cm}^{-2}\mathrm{s}^{-1}$, $\Gamma_\nu = 1.78$ and $E_{c,\nu} = 2.6\,\mathrm{TeV}$.

In Figure 2.4 the predicted neutrino fluxes for the three models discussed are shown. Despite the different assumptions made, these models produce similar fluxes. In particular, the proposed spectral index and cut-off energy in the models from Kappes et al. and Morlino et al. agree, but the flux normalisation differs. The predicted number of signal events for this analysis which is reported in Table 2.1 is quite low (less than one event is expected).

2.3. Vela X

The Vela supernova remnant is the closest SNR which contains a pulsar, PSR B0833-45. It is located at a distance of roughly 290 pc [85]. The pulsar has a period of 89.3 ms and a period derivative of 1.25 $\times$ 10^{-13} s s^{-1}, Its age is 11 kyr[2]. Radio and X-ray

[2]Assuming a braking index $\mathrm{n} = 3$, i.e. the magnetic dipole radiation is responsible for the spin-down of the pulsar

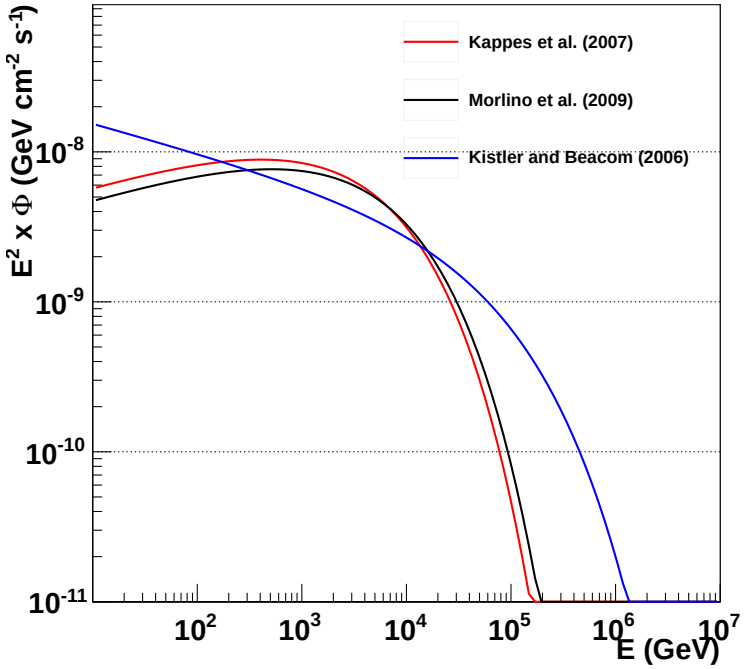

Figure 2.4.: Estimated neutrino flux from RX J1713.7-3946 as a function of the neutrino energy for the three models considered in the text: blue line for Kistler and Beacom (2006) [50], red line for Kappes et al. [95] (2007) and black line for Morlino et al. (2009) [97].

observations showed the presence of a large diffuse emission surrounding the pulsar. These radio observations established that within the 8 degrees diameter of Vela SNR there are three distinct regions of bright diffuse emission. The most intense of these regions is Vela X. It is generally believed that Vela X is a pulsar wind nebula (PWN) formed by material ejected from PSR B0833-45.

Very high-energy gamma-rays were observed by H.E.S.S. in 2006 and 2012 [42, 86]. It should be noted that the latest data yield an integral flux which is a factor 1.6 higher than previously reported. A comparison between the differential gamma-ray spectra is shown in Figure 2.5 (left) together with the source morphology (right).

The wide-band emission from Vela X is well explained by a two-zone leptonic model [87]: the gamma-ray emission is described through IC by a first population of electrons accelerated in the vicinity of the Vela pulsar. These electrons are also responsible of the synchrotron emission in X-rays. A second population of electrons with lower energies and more extended spatial distribution give rise to the radio emission.

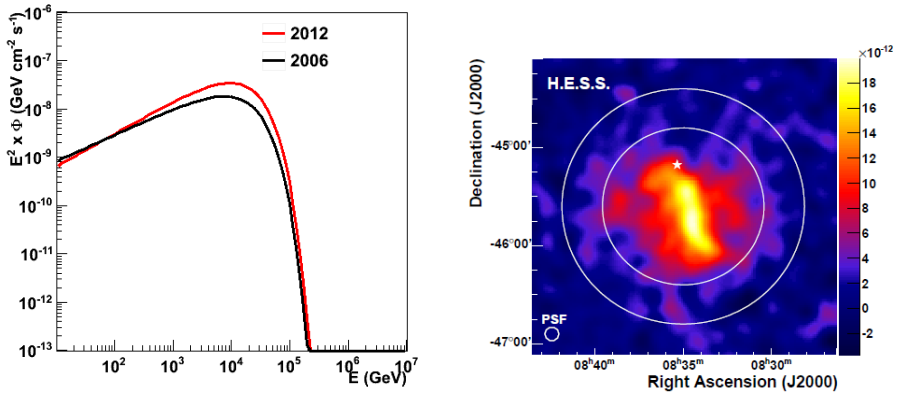

Figure 2.5.: Left: exponential cut-off power law functions which give the best fit results of the differential gamma-ray spectrum in the TeV energy range for the PWN Vela X. The black line shows the function used to fit the H.E.S.S. data from 2006. The red line corresponds to the function which fitted the H.E.S.S. data from 2012. Right: TeV image of Vela X. Figure taken from [42].

2.3.1. Neutrino emission from Vela X

Being one of the brightest Galactic sources, Vela X is an interesting candidate neutrino source. Several theoretical models of neutrino emission have been developed in the last decade. We discuss only on three of them. The neutrino flux proposed is described by a power-law function with exponential cut-off as in Equation 2.1.

- **Kistler and Beacom (2006).** The model presented in [50] was already discussed in Section 2.2.1. It also applied to Vela X. The values of the flux parameters are now $k_\nu = 6.6 \times 10^{-12}\mathrm{TeV}^{-1}\mathrm{cm}^{-2}\mathrm{s}^{-1}$, $\Gamma_\nu = 1.45$ and $E_{c,\nu} = 7\ \mathrm{TeV}$.

- **Kappes et al. (2007).** The spectrum parameters derived by Kappes et al. for Vela X are $11.75 \times 10^{-12}\ \mathrm{TeV}^{-1}\mathrm{cm}^{-2}\mathrm{s}^{-1}$, 0.98 and 0.84 $0.84\ \mathrm{TeV}$ for k_ν, Γ_ν and $E_{c,\nu}$ respectively.

- **Villante & Vissani (2008).** As last model for neutrino emission from Vela X, we consider the one described in [100] which does not need a preliminary parametrisation of the gamma-ray observations but uses directly the gamma-ray data as input. Neutrinos and hadronic gamma-rays are considered to be linked by a linear relation:

$$\Phi_\nu(E_\nu) = 0.380\Phi_\gamma(\frac{E_\gamma}{1-r_\pi}) + 0.013\Phi_\gamma(\frac{E_\gamma}{1-r_K}) + \int_0^1 \frac{dx}{x} K_\mu \Phi_\gamma(\frac{E_\gamma}{x}), \qquad (2.6)$$

  where the first and the second terms take into account neutrinos produced in pions and kaons respectively with $r_{\pi,K} = (m_\mu/m_{\pi,K})^2$. The kernel K_μ describes neutrinos

produced by muon decay and can be expressed as:

$$K_\mu(x) = \begin{cases} x^2(15.34 - 28.93x) & 0 < x < r_K \\ 0.0165 + 0.1193x + 3.747x^2 - 3.981x^3 & r_K < x < r_\pi \\ (1-x)^2(-0.6698 + 6.588x) & r_\pi < x < 1 \end{cases} \quad (2.7)$$

Similar equations describe the antineutrino emission. The calculated flux can then be fitted by power law function with exponential cut-off with $k_\nu = 0.94 \times 10^{-14} \mathrm{TeV}^{-1}\mathrm{cm}^{-2}\mathrm{s}^{-1}$, $\Gamma_\nu = 1.32$ and $E_{c,\nu} = 8\ \mathrm{TeV}$.

The predicted neutrino fluxes from the three models described above are shown in Figure 2.6. Villante and Vissani propose a neutrino flux which is well above the prediction from Kistler and Beacom and Kappes et al. This is due to the different gamma-ray data considered. The results from Villante and Vissani were derived for the latest H.E.S.S. results while the other two predictions are based on the H.E.S.S. data from 2006.

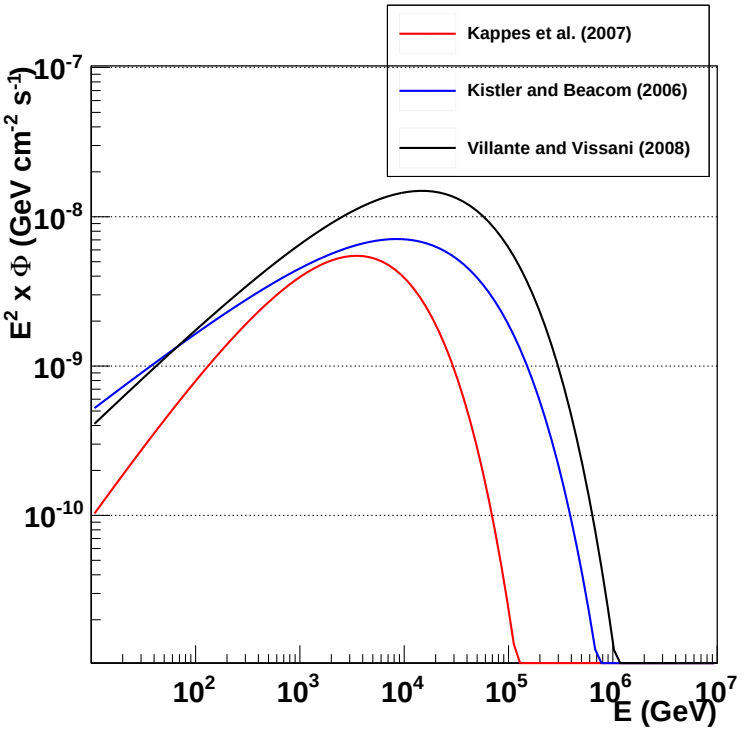

Figure 2.6.: Estimated neutrino flux from Vela X as a function of the neutrino energy for the three models considered in the text: blue line for Kistler and Beacom (2006) [50], red line for Kappes et al. [95] (2007) and black line for Villante and Vissani (2008) [100].

The expected number of signal events from Vela X assuming each one of the models is reported in Table 2.1. As for RX J1713.7-3946, also for Vela X less than one event is

expected for this analysis.

2.4. Crab

The Crab Nebula is a supernova remnant with a central pulsar located about 2 kpc from Earth. The associated SN explosion was observed in 1054 A.D. by Arabic, Chinese, Indian and Japanese astronomers. The Crab Nebula was discovered in 1731 by the English astronomer John Bevis. The central pulsar PSR B0531+21, the most energetic pulsar in the Galaxy, has a spin-down power of $4.6 \times 10^{38}\,\mathrm{erg\ s^{-1}}$.

The Crab Nebula was discovered at TeV energies in 1989 [88] by the Whipple 10 m telescope, followed by several others experiments [89, 90, 91]. The TeV gamma-ray flux from the Crab Nebula is the highest. Recent observations from the AGILE satellite [92] and FERMI-LAT [93] have discovered strong gamma-ray flares (up to 10 GeV), raising a new interest for this source.

The SED of the non-thermal emission shows two components. The low energy component can be explained by synchrotron radiation of high-energy electrons travelling through the magnetic fields of the nebula. The same electron population is responsible for the high-energy component attributed to IC scattering of photons by these electrons.

2.4.1. Neutrino emission from Crab Nebula

Although the Crab Nebula is visible at the ANTARES site for roughly 40% of the day, we report and discuss neutrino emission from this PWN keeping in mind that despite a low visibility the Crab Nebula is the brightest Galactic source. Most of the energy of the pulsar which powers the Crab Nebula is carried by a magnetised wind of relativistic plasma. The composition of this plasma is still not known. The majority of the models predicting neutrino emission from the Crab consider a plasma composed by a mixture of $e^{\pm}$, responsible of synchrotron radiation and IC scattering, and protons or ions which generate charged mesons via p-p or p-γ interactions. Indeed, a common assumption shared by these models is that a significant fraction of the rotational energy lost by the pulsar is transferred to relativistic nuclei in the nebula, which can interact with the local matter and produce CRs and neutrinos via pion decay.

An interesting model of neutrino emission is described in [101] (2005). In this, positive ions can be accelerated up to 1 PeV on the surface of young rotating neutron stars ($\leq 10^5$ yrs). A beam of muon neutrinos is produced by high-energy protons interacting with surface X-ray photons when the photomeson production resonance is reached. However, this model has been excluded at more than 90% CL by the recent IceCube point source analysis with 40 strings [59].

We now discuss three models which predict a neutrino flux parametrised by a power-law function with exponential cut-off.

- **Amato et al. (2003)**. This model [102] investigates the transfer of rotational energy lost by the pulsar to the relativistic nuclei in the pulsar wind, which is considered to be composed of these heavy ions and a denser plasma of electron-positrons pairs.

Alfvén cyclotron waves are generated by the nuclei when they meet the pulsar wind shock [103]. These Alfvén waves will resonantly scatter off positrons and electrons accelerating them [31], which are responsible for the synchrotron emission. After crossing the shock, the relativistic nuclei drift towards the outer part of the nebula. They may interact with the plerion radiation field and the ejected material to create pions which decay to neutrinos. The pion differential spectra for the p-p scattering is described as:

$$\frac{dN_\pi}{dE_\pi dt} = K_\pi E_\pi^{-1} g_\pi(E_\pi/E_p), \tag{2.8}$$

where E_p is the energy of the primary proton and the function g is parametrised as follows:

$$g_\pi(x) = (1-x)^{3.5} + \frac{e^{-18x}}{1.34}. \tag{2.9}$$

The variable K_π is related to the pulsar spin-down luminosity and to the probability for a relativistic proton to create a pion before losing energy.

The differential neutrino flux is given by:

$$\frac{dN_\nu}{dE_\nu dt} \simeq 4(1+f^\nu[3E_\nu])f^\mu[4E_\nu]\frac{dN_{\pi^\pm}}{dE_{\pi^\pm}dt}|_{E_{\pi^\pm}=4E_\nu} \tag{2.10}$$

where $f^\mu = \min[1, \mathrm{t}^\pi_{\mathrm{losses}}/\mathrm{t}^\pi_{\mathrm{decay}}]$ and $f^\nu = \min[1, \mathrm{t}^\mu_{\mathrm{losses}}/\mathrm{t}^\mu_{\mathrm{decay}}]$ take into account the energy loss of pions and muons before decaying and are derived from simulations for different Lorentz factors of the pulsar wind. The derived neutrino flux can be approximated by the function in Equation 2.1. The calculated parameters for the optimistic case with a Lorentz factor $\Gamma = 10^7$ are $k_\nu = 3.7 \times 10^{-14}\mathrm{TeV}^{-1}\mathrm{cm}^{-2}\mathrm{s}^{-1}$, $\Gamma_\nu = 1.08$ and $E_{c,\nu} = 6.47 \times 10^2\mathrm{TeV}$.

Although the predicted flux was excluded at 90% CL by IceCube [59], it is still interesting to investigate the response of the detector assuming this model for a source like the Crab Nebula with a low visibility.

- **Kistler and Beacom (2006).** As for RX J1713.7-39 and Velax, also for the Crab Nebula we report the neutrino flux predicted in [50]. The values considered for k_ν, Γ_ν and $E_{c,\nu}$ are respectively $11 \times 10^{-12}\mathrm{TeV}^{-1}\mathrm{cm}^{-2}\mathrm{s}^{-1}$, 2.57 and $50\,\mathrm{TeV}$.

- **Kappes et al. (2007).** The model described in [95] is also applied to the case of the Crab Nebula. The values of the flux normalisation, spectral index and cut-off energy are changed accordingly and are:

$$\begin{cases} k_\nu = 22.3 \times 10^{-15}\mathrm{GeV}^{-1}\mathrm{cm}^{-2}\mathrm{s}^{-1} \\ \Gamma_\nu = 2.15 \\ E_{c,\nu} = 1.72\,\mathrm{TeV} \end{cases} \tag{2.11}$$

Figure 2.7 shows the expected neutrino fluxes for these three models and Table 2.1 summarizes them. Amato et al. predict a cut-off energy roughly one order of magnitude higher than the other two models. The spectral index also differs. This is because Kistler

and Beacom and Kappes et al. based their predictions on the H.E.S.S. data which were not published yet when Amato et al. proposed their model.

The expected number of events for this analysis is significantly smaller than for the other sources and models considered. This is mainly due to the location of the Crab Nebula which is visible only for a fraction of the day of 40%.

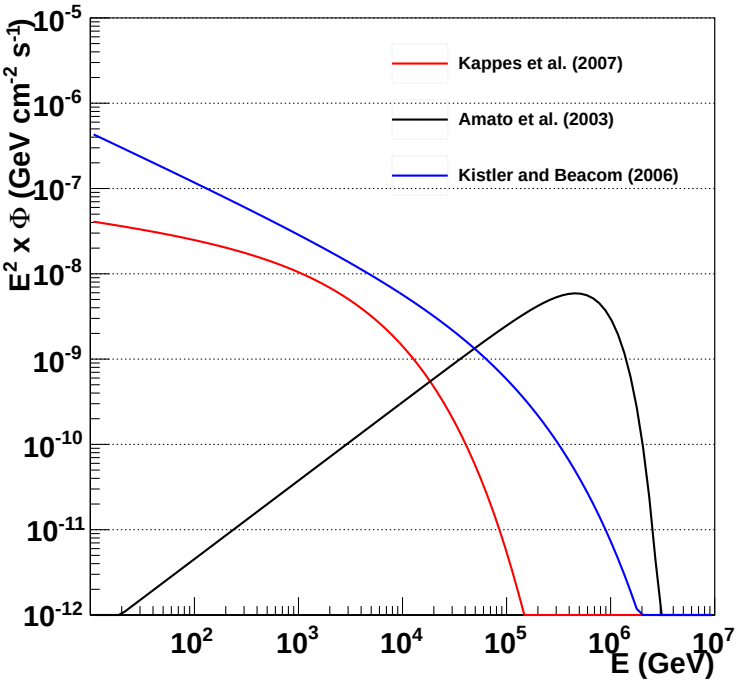

Figure 2.7.: Neutrino fluxes from the Crab Nebula as a function of the neutrino energy: blue line for Kistler and Beacom (2006) [50], red line for Kappes et al. [95] (2007) and black line for Amato et al. (2003) [102].

Source	Models	$k_\nu[\mathrm{GeV}^{-1}\mathrm{cm}^{-2}\mathrm{s}^{-1}]$	Γ_ν	$E_{c,\nu}[\mathrm{GeV}]$	$\hat{N}_{\mathrm{sig}}$
RX J1713.7-3946	Kistler & Beacom	15×10^{-15}	2.19	5×10^4	0.12
	Kappes et al.	16.8×10^{-15}	1.78	2.1×10^3	0.13
	Morlino et al.	3.01×10^{-14}	1.78	2.6×10^3	0.11
Vela X	Kistler & Beacom	6.58×10^{-15}	1.45	7×10^3	0.15
	Kappes et al.	11.75×10^{-15}	0.98	840	0.20
	Villante & Vissani	9.3×10^{-15}	1.32	8×10^3	0.60
Crab	Kistler & Beacom	11.1×10^{-15}	2.57	5×10^4	0.09
	Kappes et al.	2.23×10^{-14}	2.15	1.72×10^4	0.05
	Amato et al.	3.76×10^{-17}	1.08	6.47×10^5	0.09

Table 2.1.: Flux normalisation (third column), spectral-index (fourth column) and cut-off energy (fift column) assuming a neutrino flux parametrised by a power-law function with exponential cut-off for each source and model considered. The last column shows the expected number of events that would be selected by ANTARES using the data set 2007-2010 and applying the same cuts of the analysis described in this thesis.

3. The ANTARES neutrino telescope

Get ready for a major remodel fellas.
We are back in hardware mode.

Tony Stark

In this chapter, the detector built by the ANTARES (Astronomy with a Neutrino Telescope and Abyss environmental Research) collaboration is described. The Russian physicist Moisei Aleksandrovich Markov proposed [104] *to install detectors deep in a lake or sea water and determine the direction of the charged particles with the help of Cherenkov radiation*. The detection principle relies on the observation of the Cherenkov radiation produced by relativistic charged particles emerging from neutrino interactions with matter. Due to the small cross section of these interactions, large detectors or large target masses are required.

This chapter is organised as follows: in Section 3.1 the interactions of neutrinos with matter and the different event topologies are described. In Section 3.2 and Section 3.3 the ANTARES detector and its data acquisition system are described. The timing and position calibration are presented in Section 3.4 and finally, in Section 3.5 the main sources of background are reviewed.

3.1. Neutrino interactions

Neutrinos with energies above 10 GeV can be detected indirectly by observing the relativistic particles produced by the deep inelastic scattering off a target nucleon. The cross section for interactions with electrons is negligible with the exception of the so-called Glashow resonance, i.e. the resonant W^- production via the $\bar{\nu}_e e \rightarrow W^-$ channel at roughly 6.4 PeV [105].

The weak interaction of a neutrino with a nucleon, N, occurs in two processes described in Figure 3.1: the charged-current (CC) channel

$$\nu_l(\bar{\nu}_l) + N \rightarrow l^-(l^+) + X, \tag{3.1}$$

where a hadronic cascade, X, and a lepton, l, are produced via exchange of a W boson, and the neutral-current (NC) channel

$$\nu_l(\bar{\nu}_l) + N \rightarrow \nu_l(\bar{\nu}_l) + X, \tag{3.2}$$

where a Z-boson is exchanged.

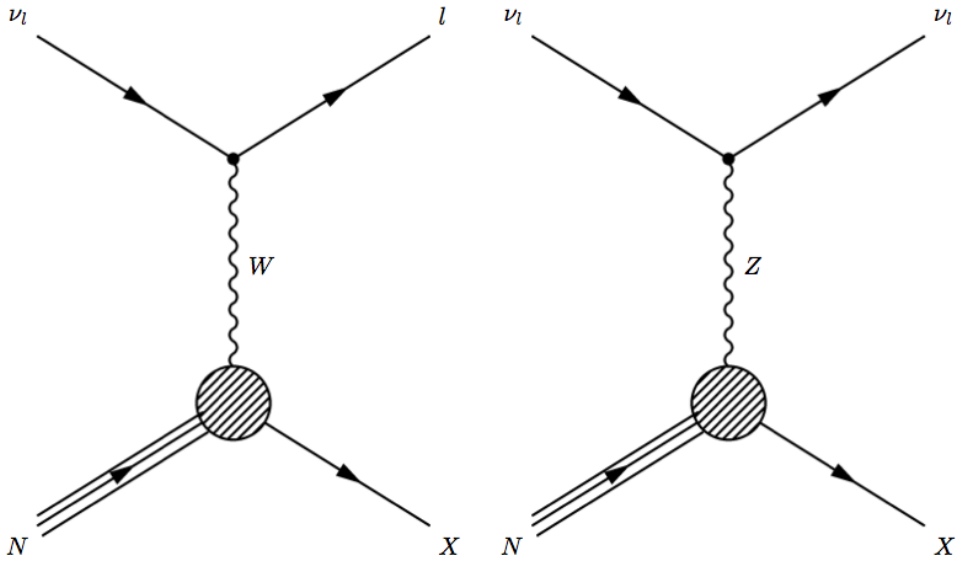

Figure 3.1.: Feynman diagrams for the charged-current (left) and neutral-current (right) channels.

Assuming that the target is an isoscalar nucleon consisting of an equal amount of protons and neutrons, the leading order differential cross section for the CC deep-inelastic scattering can be expressed as function of the Bjorken variables $x = Q^2/2m_N(E_\nu - E_l)$ and $y = (E_\nu - E_l)/E_\nu$ as [106]:

$$\frac{d^2\sigma_{\nu N}}{dxdy} = \frac{2G_F^2 m_N E_\nu}{\pi}\left(\frac{M_W^4}{(Q^2+M_W^2)}\right)^2[xq(x,Q^2) + x(1-y)^2\bar{q}(x,Q^2)], \tag{3.3}$$

where Q^2 is the square of the momentum transferred between the neutrino and the lepton, M_W and m_N are the masses of the W boson and the nucleon respectively and G_F is the Fermi coupling constant[1]. E_ν and E_l are the neutrino and lepton energies. Finally, $q(x,Q^2)$ and $\bar{q}(x,Q^2)$ are sums of parton density functions for quarks and anti-quarks respectively:

$$\begin{aligned} q(x,Q^2) &= \frac{1}{2}(d_p(x,Q^2) + s_p(x,Q^2) + b_p(x,Q^2) + d_n(x,Q^2) + s_n(x,Q^2) + b_n(x,Q^2)) \\ \bar{q}(x,Q^2) &= \frac{1}{2}(\bar{u}_p(x,Q^2) + \bar{c}_p(x,Q^2) + \bar{u}_n(x,Q^2) + \bar{c}_n(x,Q^2)) \end{aligned} \tag{3.4}$$

where the subscripts p and n denote protons and neutrons respectively and d, s, b, u, c refers to the down, strange, bottom, up and charm quarks. The contribution from top quarks has been neglected.

[1] $G_F = 1.17 \times 10^{-5}$ GeV^{-2}

Due to the isospin symmetry the quark densities in the proton are related to those in the neutron through $d_p = u_n$, $\bar{d}_p = \bar{u}_n$. Hence, assuming that the sea quark distributions in protons and neutrons are equal, it is possible to express q and $\bar{q}$ in terms of the quark density functions in the proton only:

$$q(x,Q^2) = \frac{1}{2}(d_p(x,Q^2) + u_p(x,Q^2) + 2s_p(x,Q^2) + 2b_p(x,Q^2))$$
$$\bar{q}(x,Q^2) = \frac{1}{2}(\bar{d}_p(x,Q^2) + \bar{u}_p(x,Q^2)) + 2\bar{c}_p(x,Q^2)) \quad (3.5)$$

The differential cross section for the neutral-current reaction is given by

$$\frac{d^2\sigma}{dxdy} = \frac{G_F m_N E_\nu}{2\pi}(\frac{M_Z^2}{Q^2+M_Z^2})^2[xq^0(x,Q^2) + x\bar{q}^0(x,Q^2)(1-y^2)], \quad (3.6)$$

where M_Z is the mass of the neutral intermediate boson and q^0 and $\bar{q}^0$ are obtained taking into accounts parton density functions and chiral couplings.

Details on calculations of the cross section for deep inelastic neutrino-nucleon scattering are presented in [107]. These calculations are based on the CTEQ4-DIS parton distributions [108]. The neutrino Monte Carlo simulations used in the analysis presented in this thesis use more recent parametrisations released by the CTEQ collaboration in 2002 [109].

The cross sections as a function of the neutrino energy for the CC and NC reactions for both neutrinos and anti-neutrinos are shown in Figure 3.2. For $E_\nu \leq 10\,\mathrm{TeV}$ the CC cross section rises linearly with E_ν with a value of $\sigma_{\nu N} \approx 10^{-35}\,\mathrm{cm}^2$ at $E_\nu = 1\,\mathrm{TeV}$. For higher energies, the charged (neutral) current cross section is damped by the W(Z)-propagator, resulting in a cross section proportional to $E_\nu^{0.4}$.

3.1.1. Neutrino signatures

The different types of neutrino interactions correspond to distinct signatures observed by a neutrino telescope (see Figure 3.3). For $E_\nu > 10\,\mathrm{GeV}$, the disintegration of the target nucleus occurs and a hadronic shower is created.

- **CC interaction.** For an electron neutrino, the outgoing electron loses energy in the medium via bremsstrahlung and pair production, producing an electromagnetic shower. For a muon neutrino the outgoing muon can travel up to few km before it stops (and decays). For a tau neutrino the topology is more complicated. The lifetime of a tau lepton is very short ($c\tau = 87.11\mu m$[4]) A tau lepton can decay either leptonically as $\tau \to e + \nu_e + \nu_\tau$ (branching ratio $\sim 17.8\%$) or $\tau \to \mu + \nu_\mu + \nu_\tau$ (branching ratio $\sim 17.4\%$), or hadronically into charged pions and kaons (branching ratio $\sim 65\%$). In the first case as well as in the last, two separate showers will be present, the so-called "double-bang" signature [113]. If the interaction vertex lies outside the detector only the cascade created by the τ decay will be visible ("lollipop" signature). In the case of a decay, the event signature resembles that of a CC interaction of a muon neutrino [114] however it is not detectable in the GeV-TeV range which is relevant to this analysis.

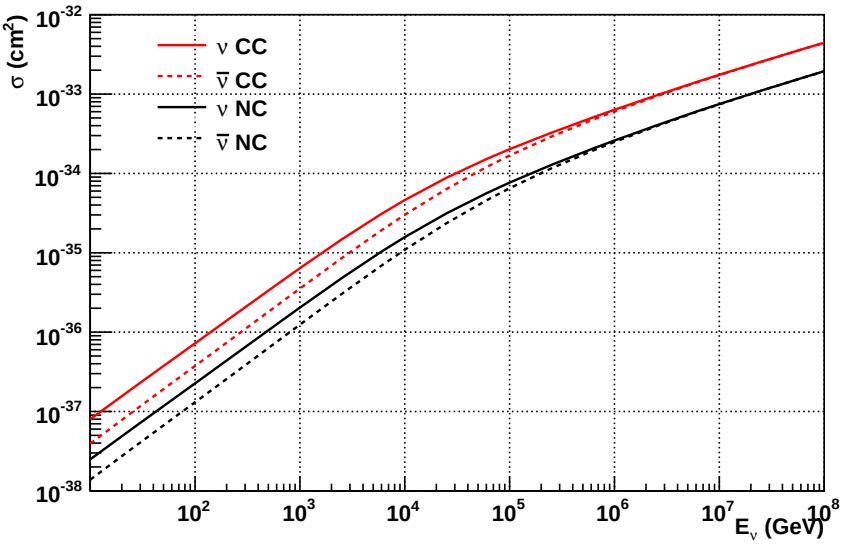

Figure 3.2.: Charged current (red lines) and neutral current (black lines) cross sections for neutrino (solid lines) and anti-neutrino (dashed lines) interactions on nucleons according to the CTEQ6-DIS parton distributions [107].

- **NC interaction.** In this case the only signature is a hadronic shower since the outgoing neutrino leaves the detector unnoticed. The length of a hadronic shower is of the order of a few meters at the energies considered in this work.

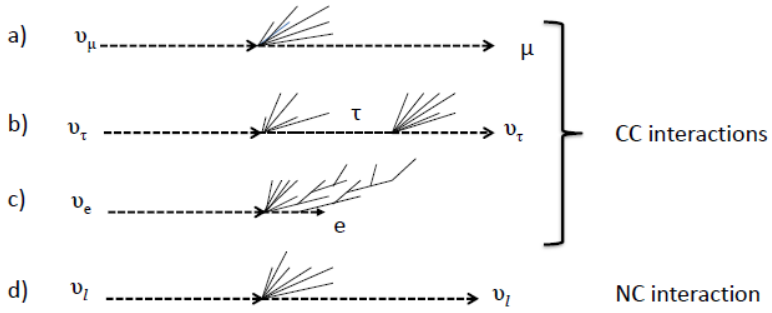

Figure 3.3.: Neutrino interactions: a) ν_μ creating a hadronic shower and a muon; b) ν_τ generating a hadronic shower and a τ which immediately decays into a second ν_τ creating another hadronic shower; c) ν_e-CC interaction with the production of an electron which initiates a hadronic shower and an electromagnetic shower; d) NC interaction of a ν of flavour l.

From now on we will consider only muon neutrinos unless otherwise stated. Muon neutrinos are very important for a search for point sources in the energy range 100 GeV $< E_\nu <$ 1 PeV. In this energy range, the muons have enough energy to traverse the detector while the vertex can occur outside the detector volume.

3.1.2. Muon propagation

The mean scattering angle between the direction of the muon and the parent neutrino after the CC interaction can be parameterised as:

$$< \Delta\theta_{\mathrm{scat}} >= \frac{0.7^\circ}{(E[\mathrm{TeV}])^{0.6}}. \tag{3.7}$$

A muon traversing a medium is also deflected by multiple Coulomb scattering. However the scattering angle due to the CC interaction is almost an order of magnitude larger. Hence, multiple Coulomb scattering can largely be ignored.

While travelling through a medium, a muon loses energy. A parametrisation of the muon energy loss is given by [110] (see Figure 3.4). At energies above 1 TeV the radiative processes are dominant.

3.1.3. Cherenkov radiation

A charged particle travelling in a transparent medium with a velocity exceeding the phase velocity of light in the medium emits Cherenkov radiation [111]. As the charged particle

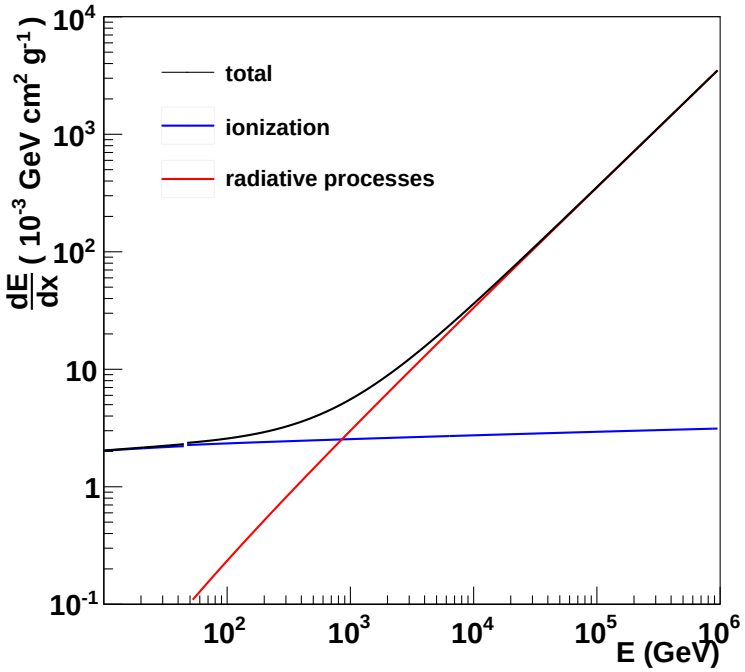

Figure 3.4.: Average muon energy losses in pure water as a function of energy. The blue line represents loss due to ionisation while the red line is for loss due to all radiative processes. The black line describes total energy losses.

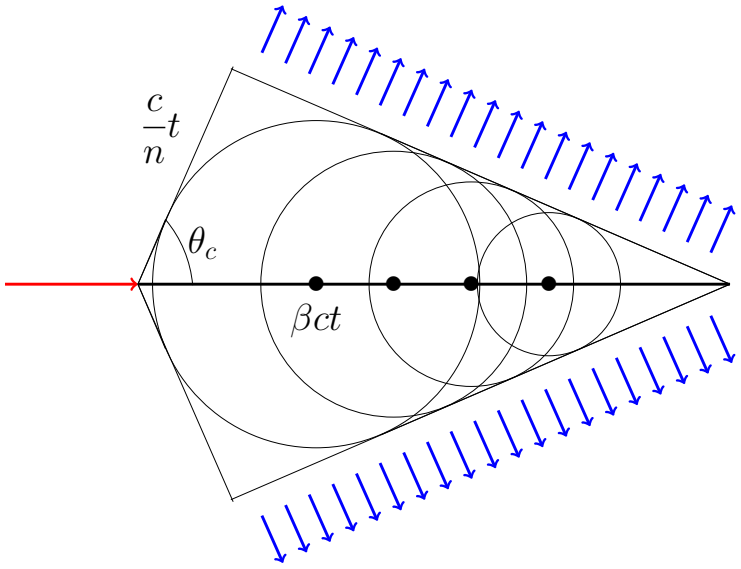

Figure 3.5.: Schematic view of the Cherenkov cone.

travels, its electromagnetic field polarises the atoms of the medium. When the electrons of the atoms restore to equilibrium, photons are emitted under a characteristic angle θ_{C} given by

$$\cos\theta_{\mathrm{C}} = \frac{1}{\beta n}, \tag{3.8}$$

where β is the velocity of the particle expressed as a fraction of the speed of light in vacuum c, and n is the refractive index of the medium. At high energies, neutrinos are relativistic particles, thus $\beta \approx 1$, and being the refractive index of sea water $n \simeq 1.364$, a value of $\theta_C \simeq 43°$ is obtained. In Figure 3.5 schematics of the Cherenkov light cone and the wave front radiation are shown.

The number of Cherenkov photons, N_γ, emitted by a particle of charge e is [112]

$$\frac{dN_\gamma}{dxd\lambda} = \frac{2\pi\alpha}{\lambda^2}(1 - \frac{1}{\beta^2 n^2}), \tag{3.9}$$

where α is the finestructure constant. For the wavelength range of the photomultiplier tubes in ANTARES (300-600 nm), $N_\gamma \simeq 3.5 \times 10^4$ photons per meter.

3.2. Detector layout

The ANTARES detector [119] is located at a depth of 2.475 km in the Mediterranean Sea, roughly 40 km off the coast of the south of France at 42°48'N, 6°10'E (Figure 3.6). It

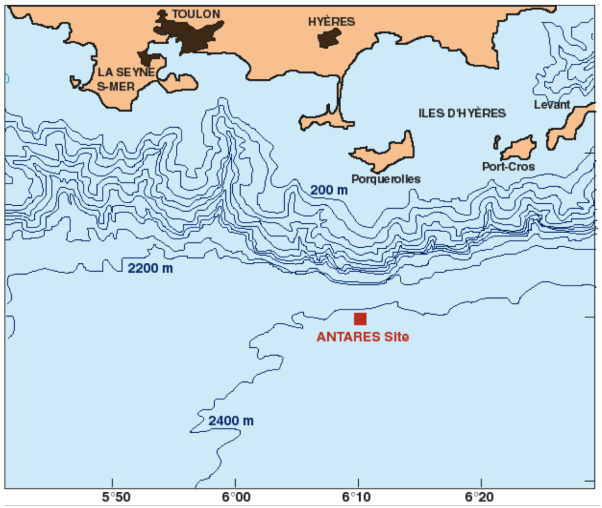

Figure 3.6: Location of the ANTARES site. The detector is located at 2475 km depth, 40 km away from the coast. Indicated are the depth levels and the coast line. The telescope is connected via a deep sea cable to the "shore station" at La Seyne sur Mer where the transmitted data are filtered.

consists of an array of flexible lines (also called strings) separated by a distance of $\sim 70\mathrm{m}$. Figure 3.7 shows a schematic view of the detector.

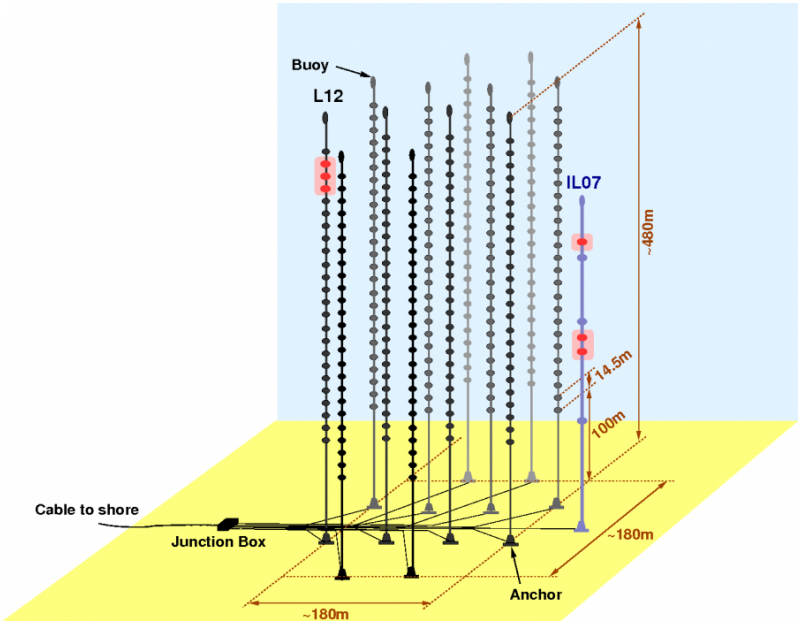

Figure 3.7.: ANTARES layout in a schematic view. The main elements of the ANTARES detector are outlined in the figure. Each string consists of 25 storeys and it is connected to the junction box.

The key elements of the detector are the Optical Modules (OMs) [120] (see Figure 3.8). Each OM consists of a pressure-resistant glass sphere (43 cm in diameter with a thickness of 15 mm) containing a Hamamatsu R7081-20 photomultiplier (PMT) (nominal gain of 5×10^7 at a high voltage of 1760 V). The photo-catode is sensitive to light in the 300 - 600 nm wavelength range and has a maximum quantum efficiency of approximately 25% at 370 nm.

The timing resolution of the PMT is determined by the spread of the transit time, i.e. the interval between the arrival of the photon and the current pulse in the anode. The standard deviation of the Transit Time Spread (TTS) is approximately 1.3 ns. In order to avoid possible degradation of the TTS due to the Earth's magnetic field ($\sim 46\ \mu\mathrm{T}$ at the ANTARES site), the PMT is surrounded by a high permeability μ-metal cage.

Triplets of OMs form the so-called storeys (or floors) which is shown in Figure 3.9. In a storey the 3 OMs are grouped at equidistant angles around a titanium Optical Module Frame (OMF). The OMs point downward at 45° in order to foster the detection of upgoing events. The OMs also house the Local Control Module (LCM), a titanium cylinder which contains the data transmission electronics.

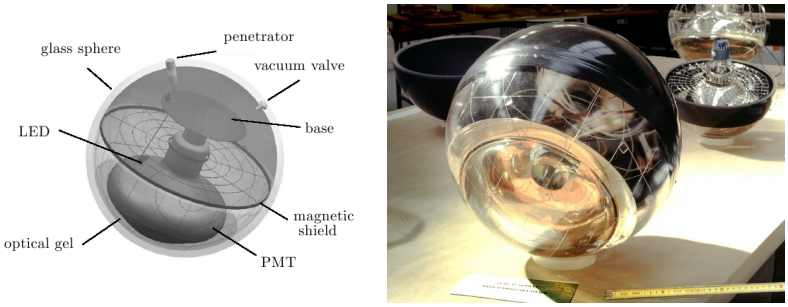

Figure 3.8.: Schematic view (left) and picture (right) of an ANTARES optical module.

All the storeys in a line are connected by an Electro-Mechanical Cable (EMC) equipped with electrical wires for power supply and optical fibres for data transmission. A group of five consecutive storeys in the same line forms a sector, an independent unit in terms of power distribution and data acquisition. Each sector houses a Master Local Control Module (MLCM) which collects the data and sends them to shore.

The ANTARES detector in its final configuration consists of 12 lines, each line with 5 sectors (25 floors) with a total of 885 PMTs[1]. The distance between adjacent storeys is 14.5 m. The bottom 100 m of the line is not instrumented. A buoy at the top of the lines keeps them vertical while they are anchored to the soil via a Bottom String Socket (BSS) which contains electronics for powering and controlling the string.

There is a thirteenth line, known as Instrumentation Line (IL) which is equipped with various devices for acoustic neutrino detection (also in the top sector of Line 12) and water properties measurement.

[1] $(12 \times 5 \times 5 \times 3) - (5 \times 3) = 885$ since at the top sector of Line 12 there are no OMs but various acoustic devices. [121]

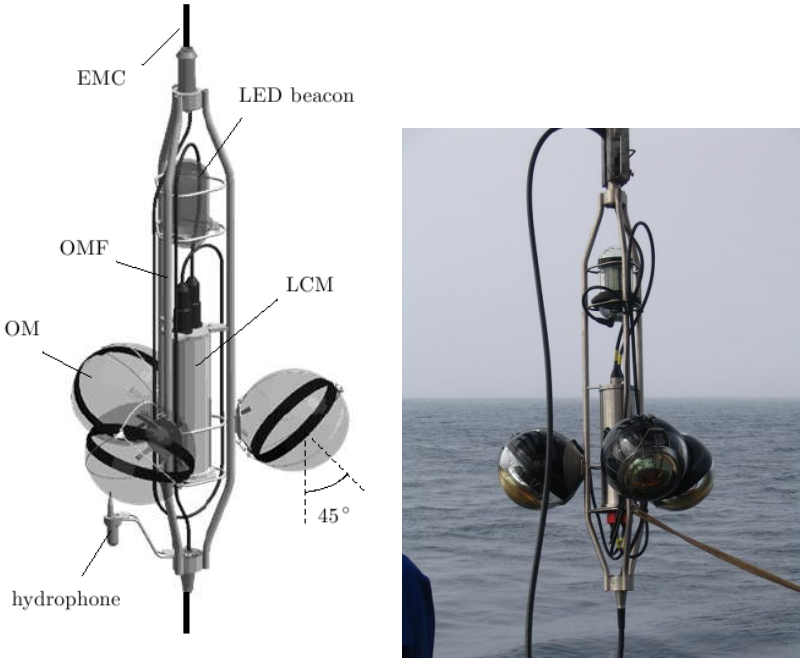

Figure 3.9.: Schematic view (left) and picture (right) of a storey

The BSS of each line is linked to the Junction Box (JB), a pressure-resistant titanium container which provides power to the lines and is connected to the onshore control room by means of the ∼40 km long Main Electro-Optical Cable (MEOC).

3.2.1. Detector status and milestones

The first string (Line 1) of the ANTARES detector was deployed on March 2$^{\mathrm{nd}}$ 2006. Data taking started the same day. A few months later, in July 2006, Line 2 was deployed. It was connected on September 21$^{\mathrm{st}}$ becoming the second operational line of the detector. On January 29$^{\mathrm{th}}$ 2007 the connection of Lines 3-5 took place. As a result, ANTARES became the most sensitive neutrino telescope in the Northern Hemisphere.

Lines 6-10 were connected on December 7$^{\mathrm{th}}$ 2007 and the detector was completed in May 2008 with the connections of Lines 11 and 12. From June 25$^{\mathrm{th}}$ 2008 to September 5$^{\mathrm{th}}$ a problem in the MEOC forced to stop data taking. With the exception of this period, ANTARES has been taking data.

Figure 3.10 shows the effective days of data taking from year 2009 to 2011. Causes for loss of efficiency are the periods of high bioluminiscence (see Section 3.5.1) and sea operations.

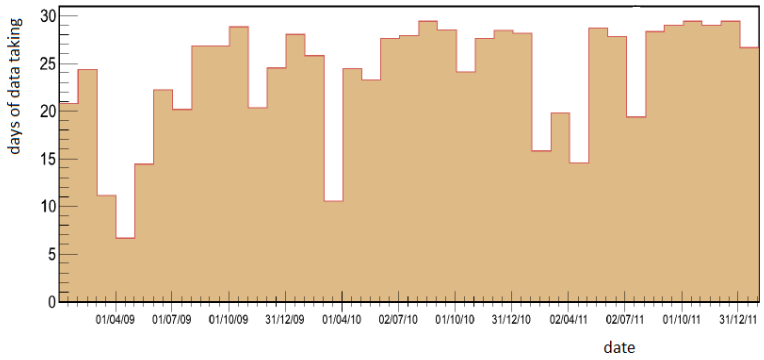

Figure 3.10.: Effective days of data taking per month during 2009-2011.

The complete detector collects an average of 5 atmospheric muons per second. The rate of neutrinos is roughly 3 per day. Figure 3.11 shows the number of events reconstructed as upgoing per one month of data taking after applying quality cuts.

3.3. Data acquisition system

A key feature of the ANTARES Data AcQuisition (DAQ) [122] system is the "all-data-to-shore" concept. All signals from the PMTs that pass a pre-defined threshold voltage, typically the equivalent of 0.3 Single Photo Electrons (SPE), are digitised at the LCM and sent to shore. In the following we discuss the relevant aspects of the DAQ system which is schematically depicted in Figure 3.12.

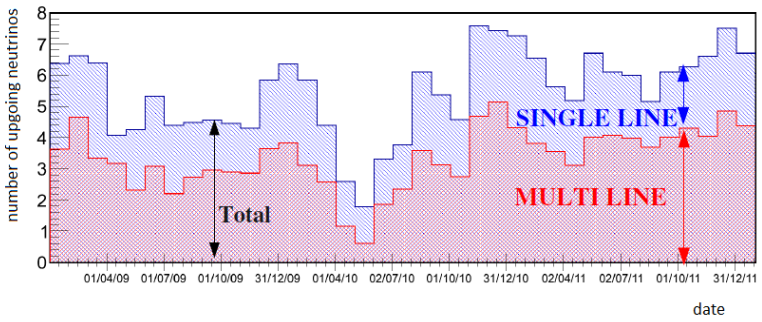

Figure 3.11.: Number of upgoing neutrinos per month during the period of data taking 2009-2011. The red histogram shows the events reconstructed with more than one detector string. The blue histogram shows the single line events.

3.3.1. Signal digitisation

The analogue signals from the PMTs are digitised by two front-end integrated circuits, called Analogue Ring Samplers (ARSs), located in the LCM. The two ARSs operate in a token ring configuration to reduce the impact of the chips dead time (about 200 ns). A local clock in each detector storey, synchronised with a 20 MHz onshore master clock, provides the time-stamp of each PMT signal above the threshold voltage. A Time to Voltage Converter (TVC) is then used to provide a measurement of the time of the signal between two consecutive clock ticks. The voltage output of the TVC is digitised by an 8-bit Analogue to Digital Converter (ADC). Thus, the timing resolution of the TVC is $(20\ \text{MHz})^{-1} \times 256^{-1} \simeq 0.2$ ns. The ARSs also integrate and digitise the charge of the analogue signal over a certain time interval (typically 25 ns). The resulting time and charge information of the PMT signal is referred to as a hit. The output of the ARSs is processed by a Field Programmable Gate Array (FPGA) which arranges the hits in dataframes with a time window of 104.858 ms.

3.3.2. Data transport

The data transport is managed by two programs run by a CPU contained in each LCM and connected to the onshore computer's farm. They control the transmission of the data by sending to shore each frame as a single packet and take care of the power supply.

The communication to shore is done using optical fibres through the TCP/IP protocol. In each sector the MLCM contains an Ethernet switch which merges the bi-directional 100 Mb/s Ethernet links from the five storeys into a single Gb/s Ethernet link. Dense Wavelength Division Multiplexing (DWDM) technique is used for the data transmission to shore. The DWDM system combines different data streams into one signal in a single fibre using different wavelengths.

3.3.3. Filtering and storage

Following the all-data-to-shore prescription, no off-shore selection of the data is done with the only exception of the ARS threshold voltage. Due to the large amount of optical background (see Section 3.5.1) and limited storage space available, an on-line filter is required on-shore to reduce the data stream. This will be explained in Section 4.1.

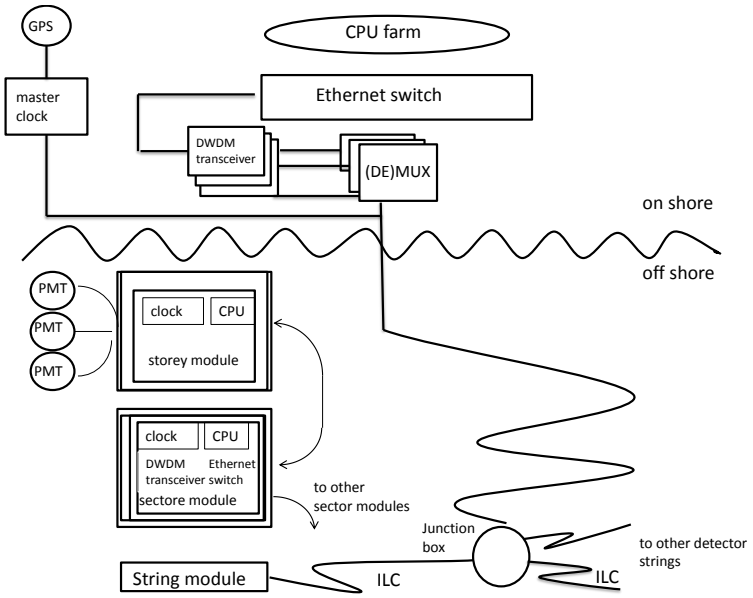

Figure 3.12.: Schematic view of the ANTARES data acquisition system.

3.4. Calibration

The calibration of the detector is crucial to achieve a good angular resolution (expected to be $< 0.3^{\circ}$ for muon events above 10 TeV [123]), since the precision of the reconstructed direction of charged particles traversing the detector depends on the accuracy of the measured photon arrival times and PMT locations. In the following, the three main calibration schemes are described.

3.4.1. Clock calibration

Several devices are used in ANTARES to perform timing calibration measurements:

- Internal Optical Module LEDs. A blue (470 nm) LED is mounted in each OM at the back of the PMT and is used to measure the relative variation of the transit time of the PMTs by illuminating the photocatode from the back. Dedicated runs for this calibration are taken once per month.

- Optical Beacons. The Optical Beacon (OB) system is used to measure the relative time offset between PMTs. It consists of four blue (470 nm) LED Optical Beacons (LOBs) placed on storeys 2, 9, 15 and 21 of each detector string in order to illuminate all the other lines and two green (532 nm) Laser Beacons mounted at the bottom of Lines 7 and 8. A LOB is made by 36 individual LEDs forming an hexagonal cylinder. It is shown in Figure 3.13 (left) together with the Laser Beacon (right).

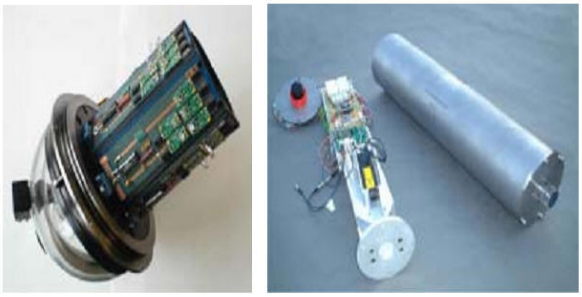

Figure 3.13.: Picture of an LED optical beacon (left) and a laser beacon (right).

The measurements obtained by the internal LEDs and OB systems have shown that the contribution of the detector electronics to the photon arrival time resolution is small. The value obtained after corrections is roughly 0.5 ns. Hence, the time resolution is mainly limited by the TTS of the PMTs ($\sigma_{\mathrm{TTS}} \simeq 1.3$ ns). Other factors which influence the timing accuracy are the scattering and the chromatic dispersion of the Cherenkov light in sea water ($\sigma \simeq 1.5$ ns for a light propagation path of 40 m) [124].

3.4.2. Positional calibration

The strings are not rigid but move due to underwater sea currents. Even relatively slow water currents of ~ 5 cm/s can drag the top storey of the lines of a few meters [125]. A frequent measurement of the position of each OM is therefore required. To achieve this task each detector line is equipped with five acoustic receivers on storeys 1, 8, 14, 20 and 25, called hydrophones. They measure high-frequency acoustic signals (40-60 kHz) emitted by transceivers placed at the BSSs. An additional emitter is located 145 m far from the detector. Measurements of the travel time between the emitters and the receivers are performed every 2 minutes. The sound velocity is monitored by dedicated oceanographic instrumentation making it possible to determine the distances between acoustic receivers and emitters. The position of each line is computed by triangulation (with respect to the emitters on the BSS).

The orientation of the storeys, i.e. the pitch, roll and the heading angles, is measured by the Tiltmeter-Compass System, a set of bi-axial tiltmeters and compasses installed in the LCM of each storey.

The shape of each detector string is reconstructed by a global fitting procedure which uses all these measurements. The accuracy with which the string positions are constrained

by the calibration is better than 10 cm [125]. Some reconstructed detector line shapes for different sea current velocities are shown in Figure 3.14.

Absolute positioning

The absolute orientation of the detector is determined via acoustic triangulation of the BSS positions with respect to a ship at the sea surface. The absolute position of the ship is measured by a GPS system. The uncertainty on the absolute pointing of the detector was estimated via Monte Carlo techniques taking into account the errors on the individual BSS positions, BSS to BSS distances and on the sound velocity [126]. The resulting uncertainty was estimated to be 0.127° horizontally and 0.035° vertically.

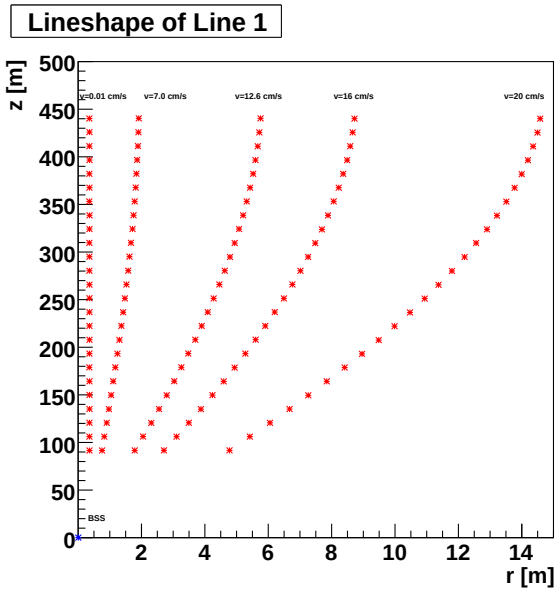

Figure 3.14.: Reconstructed shape of Line 1 for different sea current velocities.

3.4.3. Charge calibration

The charge of the PMT signal is digitised into a value called "AVC". The relation between the number of photoelectrons and the AVC is given by the so called transfer function:

$$f(\mathrm{AVC}) = \frac{\mathrm{AVC} - \mathrm{AVC}_{0\mathrm{pe}}}{\mathrm{AVC}_{1\mathrm{pe}} - \mathrm{AVC}_{0\mathrm{pe}}}. \tag{3.10}$$

where $\mathrm{AVC}_{0\mathrm{pe}}$ is the value of AVC corresponding to zero photoelectrons and $\mathrm{AVC}_{1\mathrm{pe}}$ corresponds to the single photoelectron peak. Boths values are determined by regular calibration runs.

Charge measurements in AVC channels are affected by time measurements in the TVC channel. This is known as "cross talk" effect and it is generally attributed to interference between the capacitors inside the ARS pipeline. In situ measurements are performed in order to correct this effect.

3.5. Backgrounds

ANTARES is affected by two sources of background: the interaction of cosmic rays in the atmosphere and the emission of light due to environmental activities such as bioluminescence and the decay of radioactive sea salt (optical background).

3.5.1. Optical background

Despite a depth of 2475 km, the ANTARES location is not totally dark. There is an optical background contribution of environmental origin. This background constitutes the count rate in the PMTs. An example of the count rate as a function of time is shown in Figure 3.15. The count rate can be decomposed into a continuous component, the baseline rate, which varies between 60 kHz and 70 kHz, and in short time scale (typically $\sim$1 s) bursts up to several MHz. The baseline rate is thought to be caused by three different sources: the PMT dark noise ($\sim$ 3 kHz), bioluminescence from bacteria and light from radioactive decays. Bioluminescence is the emission of light by organisms living in the deep sea. The rate of bioluminescence light varies in time and it is expected to be correlated to the number of luminescent organisms in the water and to the sea current velocity. At the ANTARES site $\sim 0.012\%$ of potassium in sea water consists of the radioactive isotope $^{40}\mathrm{K}$ which decays mainly (branching ratio of 89%) into $^{40}\mathrm{Ca}$ via β-decay emitting an electron with a maximum energy of 1.3 MeV, enough to produce Cherenkov light. Another possible reaction is via electron capture with the creation of $^{40}\mathrm{Ar}$ and the emission of a 1.46 MeV photon which can Compton scatter an electron above the Cherenkov threshold. Taking into account the salinity (S = 38.47 per mil), the disintegration rate of ^{40}K in water yields a counting rate of $\sim$30 kHz [127]. The baseline rate is shown in Figure 3.15 (top).

The bursts are due to multicellular organisms which emit light for short periods of time. The fraction of the time during which the rate of these bursts exceeds the baseline rate by at least 20% is called burst fraction. An example of the burst fraction as a function of time is shown in Figure 3.15 (bottom).

3.5.2. Cosmic ray background

Figure 3.16 (top) illustrates the two main backgrounds due to cosmic rays for a neutrino telescope: atmospheric muons and atmospheric neutrinos. Cosmic protons interacting with atmospheric nuclei create hadronic cascades of secondary particles including π^+ and π^- that decay into muons and neutrinos via

$$\begin{aligned} \pi^{\pm} &\longrightarrow \mu^{\pm} + \bar{\nu}_{\mu}(\nu_{\mu}) \\ \mu^{\pm} &\longrightarrow e^{\pm} + \nu_e(\bar{\nu}_e) + \bar{\nu}_{\mu}(\nu_{\mu}). \end{aligned} \tag{3.11}$$

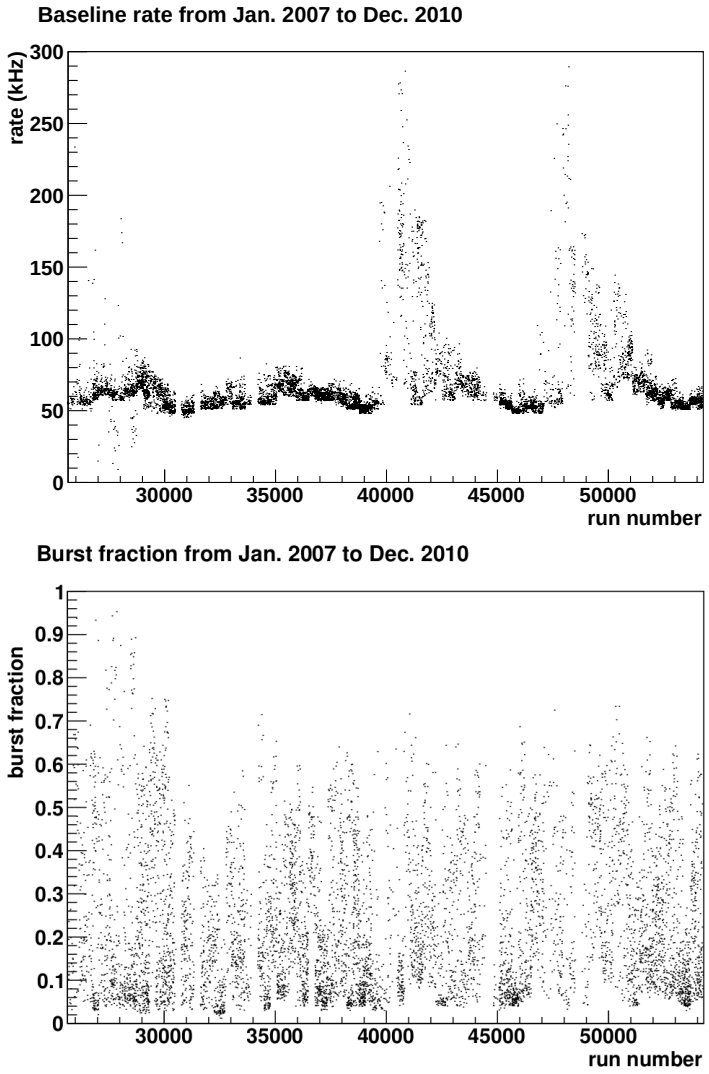

Figure 3.15.: Top: baseline rate from January 2007 to December 2010. Bottom: burst fraction for the same period.

Some muons produced in this reaction have sufficient energy to cross the atmosphere and travel for several kilometers through the sea before stopping. Despite the fact that the ANTARES PMTs face downward, many of these muons produce hits.

A significant rejection of the atmospheric muon background is possible by restricting the neutrino search to upward going tracks. The remaining background consists of downward going muons which are mis-reconstructed as upward going. The rejection of downward going bundles of muons, i.e. parallel muons coming from the same air shower, requires a stricter selection of events.

The second source of background originating from cosmic ray interactions are atmospheric neutrinos. Atmospheric neutrino background contribution is reduced in two ways:

- by looking at the energy spectrum which is expected to be flatter for astrophysical neutrinos at high energies.
- by looking for an excess of events over a certain direction as in the search for point-like sources which is the main subject of this thesis.

Figure 3.16 (bottom) shows the atmospheric muon flux and the muon flux induced by atmospheric neutrinos as a function of the cosine of the zenith angle. The atmospheric muon flux is roughly six order of magnitude larger than the flux of induced muons by atmospheric neutrinos. An enhancement of atmospheric neutrinos at the horizon ($\cos\theta \simeq 0$) can be seen. The air density decreases with the altitude therefore horizontal pions travel a larger path without interacting. This yields a larger probability to decay and to produce neutrinos.

Above 100 TeV, prompt neutrinos produced by the semi-leptonic decay of charmed mesons (for example $\mathrm{D} \rightarrow \mathrm{K} + \mu + \nu$) are expected to follow the primary cosmic ray spectrum, i.e. a harder energy spectrum compared to atmospheric neutrinos. Hence, they can be a source of background for the search of a diffuse astrophysical neutrino flux where the neutrino energy spectrum is measured. So far, prompt neutrinos have not been observed yet [128] and theoretical model predictions show very large uncertainties [129].

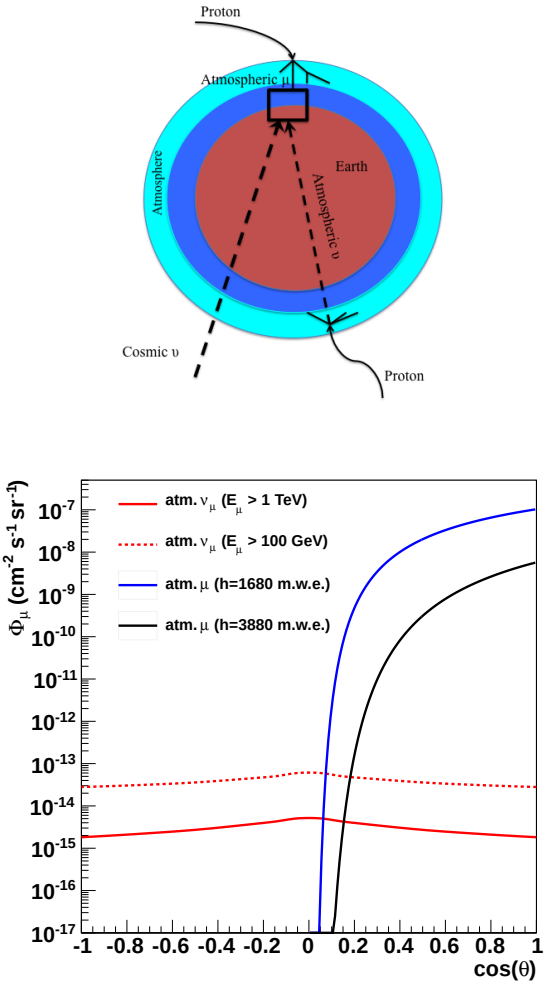

Figure 3.16.: Top: Illustration of the detection principle of neutrino telescopes. Neutrinos, after travelling through the Earth, produce up-going muons. The background consists of atmospheric muons and atmospheric neutrinos produced by the cosmic rays interactions in the atmosphere. Bottom: Atmospheric muons flux for different depths [130] and the muon flux induced by atmospheric neutrinos for different energies [131] as a function of the cosine of the zenith angle

4. Simulation and reconstruction

We can only see a short distance ahead, but we can see plenty there that needs to be done.

Alan Turing

In this chapter, the simulation of the signal and the background is described and the track reconstruction algorithm used in the analysis is presented. First, the trigger algorithms responsible for data filtering are introduced in Section 4.1. Section 4.2 presents the Monte Carlo tools: event generation and detector response. Finally, Section 4.3 focuses on the muon track reconstruction.

4.1. Triggers

All the hits exceeding a pre-defined threshold, typically the equivalent of 0.3 single photo-electrons (L0 hits) are sent to shore where they are filtered by a farm of PCs. This results in a transfer of several Gb/s to shore. Most of the hits are due to optical background from $^{40}\mathrm{K}$ decays or bioluminescence. Optical background hits are uncorrelated and induce primarily single photo-electrons hits. Hence, a first filtering is done by requiring hits with a high charge (usually > 3 photo-electrons) or coincident hits within a time window of 20 ns on separate PMTs of the same storey. Hits satisfying these criteria are called "L1 hits". With this first selection, the amount of data is reduced by a factor of 10^2 [132].

Hits originating from the same muon normally fulfill the "causality" criterion:

$$|\Delta t| \leq \frac{c}{n_g} \cdot d + 20\,\mathrm{ns} \tag{4.1}$$

where Δt is the time difference between two hits, d is the distance between the two PMTs which have recorded the two hits and c/n_g is the group velocity of light in sea water. An additional $\pm$20 ns is added to this time window to account for possible time calibration uncertainties and light scattering. A set of L1 hits which satisfies Equation 4.1 forms a cluster. A cluster of sufficient size (typically $N_{\mathrm{L1}} \geq 5$) is selected together with all L0 hits within 2.2 μs the first and the last L1 hit. This value was chosen since it corresponds to the time needed by a relativistic muon to traverse the detector.

In addition to this first level selection, dedicated triggers are applied. We describe the two main filter algorithms used for the second level of events selection:

- **3N trigger**. The condition imposed by Equation 4.1 becomes stricter if the direction of the muon track is assumed. The 3N trigger tries a number of muon track directions

looking for clusters of hits in a time window compatible with the Cherenkov emission. Since the direction of the muon is not known, the solid angle is divided in a grid with a spacing of about 10°. The arrival time t_i of a Cherenkov photon emitted by a muon is:

$$t_i = t_0 + \frac{1}{c}(z_i - \frac{r_i}{\tan(\theta_C)}) + \frac{1}{v_g}\frac{r_i}{\sin(\theta_C)}, \tag{4.2}$$

where z is the distance along the muon, θ_C is the Cherenkov angle, v_g the group velocity of light in water, r_i is the distance of closest approach between the muon and the PMT and t_0 is the time when the muon was at z=0. The second term in Equation 4.2 describes the time that it takes to the muon to travel from the initial position to the position where the photons are emitted. The last term is the time needed by the photons to reach the PMT. Figure 4.1 illustrates the topology. Hence, the 3N trigger selects clusters with pairs of hits which follow the relation

$$|t_i - t_j| \leq \frac{z_i - z_j}{c} + \frac{R_{ij}}{c}\tan(\theta_C) + 20\,\mathrm{ns}, \tag{4.3}$$

where R_{ij} is the distance between PMT$_i$ and PMT$_j$ perpendicular to the muon direction as shown in Figure 4.1.

- **T3 trigger.** The T3 trigger requires two disjunct clusters, each consisting of at least two L1 hits in three consecutive storeys within a specific time window. This time window is 100 ns in case that the two storeys are adjacent and 200 ns for next-to-adjacent storeys. A minimum number of T3 clusters is then required in a pre-defined time window. For example, for two T3 clusters (2T3) at least 4 L1 hits are needed.

For the analysis presented in this thesis we select events from either the 3N trigger or the 2T3 trigger.

4.1.1. Trigger efficiency

The performance of the trigger is usually expressed in terms of its efficiency. The trigger efficiency for the 3N and the 2T3 trigger algorithms as a function of the neutrino energy is shown in Figure 4.2. It is defined as the ratio between the number of triggered events and the total number of reconstructed events. It is derived using a Monte Carlo sample which simulates the data taking period 2007-2010.

Figures 4.3 (atmospheric neutrinos) and 4.4 (E_ν^{-2} neutrinos) shows the trigger efficiency as a function of different reconstruction parameters: the neutrino zenith angle, θ_ν, the number of hits, N_{hits}, and the reconstruction variable Λ (see Section 4.3 for its definition).

For atmospheric neutrinos, the efficiency of the 2T3 trigger is on average in the range 70%-80% while the 3N trigger has a better efficiency at higher energies. A similar behaviour is seen for astrophysical neutrinos.

The 3N trigger efficiency for astrophysical neutrinos is higher than for atmospheric neutrinos. For the 2T3 trigger instead, atmospheric and astrophysical neutrinos are selected with roughly the same efficiency.

The trigger efficiency for the 3N and 2T3 trigger algorithms for both atmospheric and signal neutrinos is also summarised in Table 4.1.

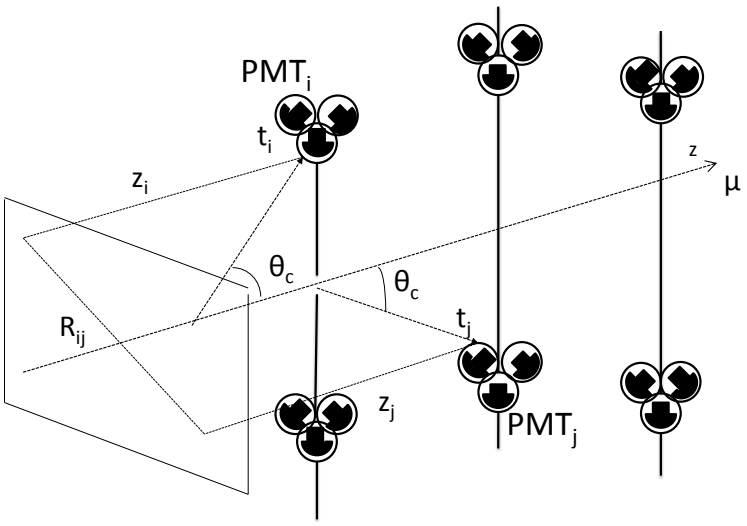

Figure 4.1.: Schematic view of a muon traversing the detector.

	atm. ν	$E_\nu^{-2}\nu$
Triggered events	100%	100%
3N events	66%	87%
2T3 events	84%	78%
3N only	14%	21%
2T3 only	33%	11%

Table 4.1.: Trigger efficiency for a Monte Carlo sample of atmospheric (second column) and signal (last column) neutrinos simulating the data taking period 2007-2010. The last two rows show the percentage of 3N (2T3) triggered events which are not accepted by the 2T3 (3N) trigger algorithm respectively.

4.2. Monte Carlo simulation

The interpretation of the data requires an accurate Monte Carlo (MC) simulation, which is used to understand the background contamination. MC simulations are also required to determine the acceptance and the angular resolution of the detector, since in the absence of a source of known size and intensity these quantities cannot readily be measured.

The MC simulation for the ANTARES detector can be divided in two stages:

- **Event generation.** Primary particles are generated at the top of the atmosphere (muons) or in a cylinder surrounding the detector (neutrinos) according to certain physical models.

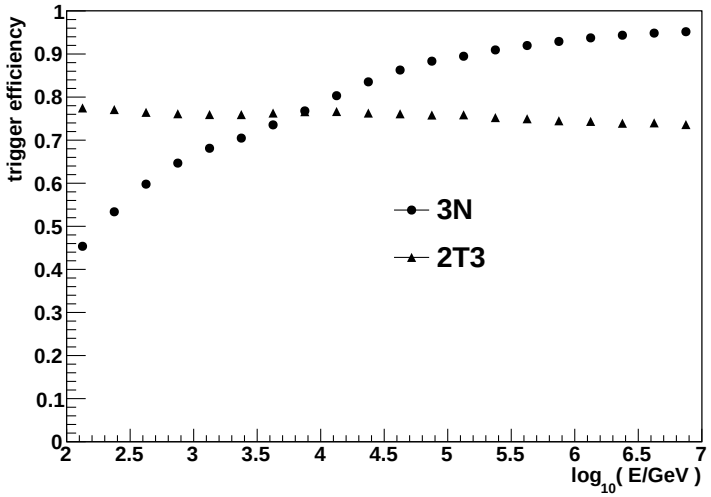

Figure 4.2.: Trigger efficiency for the 3N and 2T3 trigger algorithms defined as the ratio between the number of triggered events and the total number of reconstructed events as a function of the neutrino energy. A simulated sample of atmospheric neutrinos corresponding to the period of data taking 2007-2010 is used.

- **Light propagation and detector simulation.** The emission of Cherenkov light and the production of secondary particle showers is simulated in this phase. Then, the response of the detector to Cherenkov photons is simulated by taking into account the PMTs response, the electronic of the LCM and the triggers logic.

4.2.1. Event generation

The first step in the simulation chain is the event generation. Both neutrinos (atmospheric and cosmic) and muons are generated.

Neutrinos

Muon neutrino events are simulated using the GENHEN v6r3 [134] package. A large number of interactions[1] is generated within a cylinder around the detector. The size of this cylinder is chosen so that all the neutrinos which can produce a detectable muon inside the detector are simulated. Thus, the maximal muon range and the highest neutrino energy generated ($E_\nu^{\max} = 10^8$ GeV) are taken into account. Typically, this cylinder is 25 km in radius and height. Charged current interactions are simulated at this stage. The CTEQ6 parton distribution functions [109] are used for the cross section calculations. The probability for a neutrino to survive while traversing the Earth is given by Equation 1.23.

[1] for the analysis presented in this thesis 5×10^8 neutrinos and anti-neutrinos for each run were simulated.

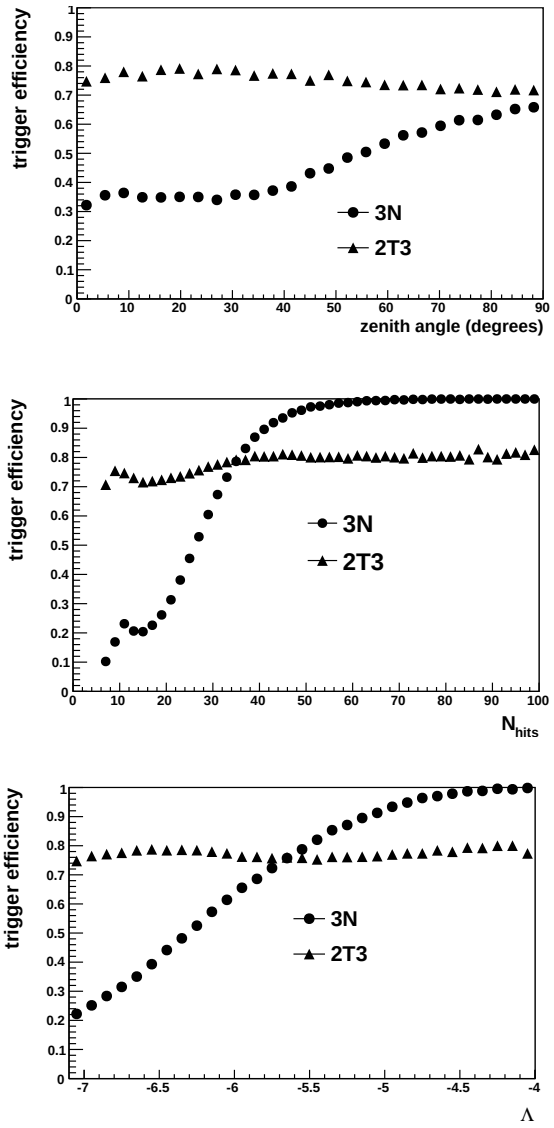

Figure 4.3.: Trigger efficiency for the 3N and 2T3 trigger algorithms defined as the ratio between the number of triggered events and the total number of reconstructed events as a function of the following parameters (from top to bottom): neutrino zenith angle, number of hits and Λ. A simulated sample of atmospheric neutrinos corresponding to the period of data taking 2007-2010 is used.

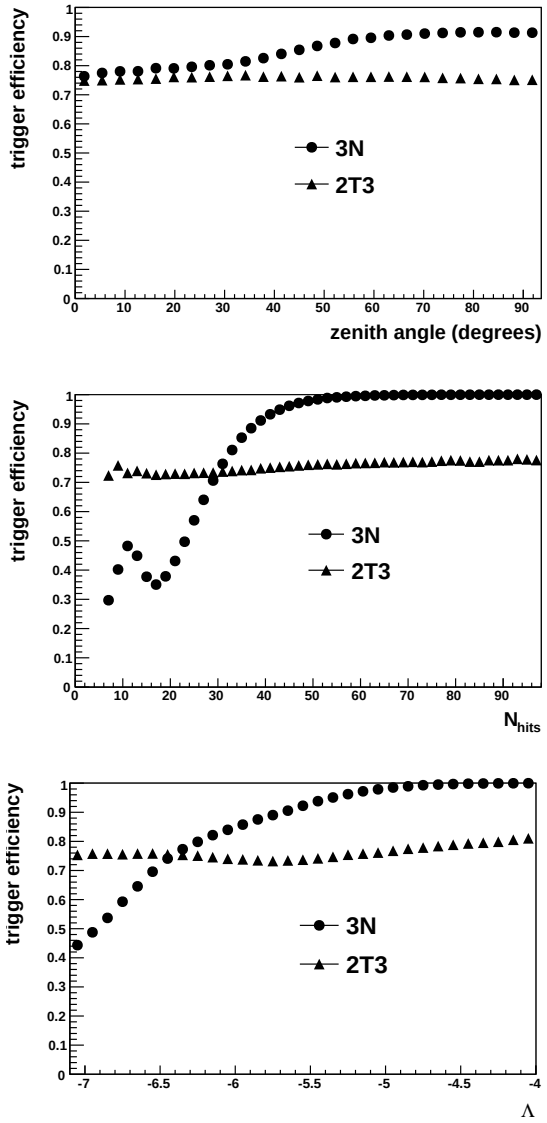

Figure 4.4.: Same as Figure 4.3 but for signal neutrinos with a spectrum proportional to E_ν^{-2}.

As was mentioned in Section 1.2.3, this probability is taken into account in the event rate calculations. The Earth density used is the Preliminary Reference Earth Model [135]. It is shown in Figure 4.5.

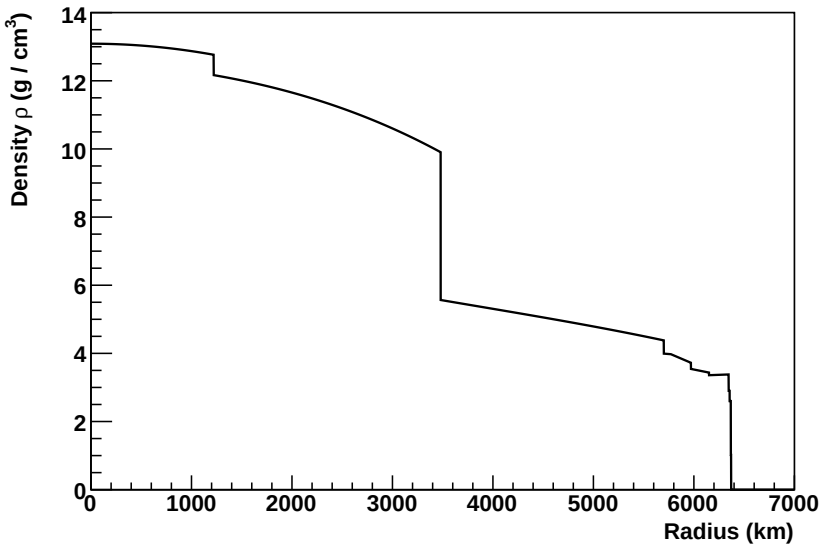

Figure 4.5.: Density profile of the Earth in the Preliminary Earth Model [135].

The neutrino directions are uniformly generated in the cosine of the zenith angle, in the range $[\cos\theta_{\rm min} = -1, \cos\theta_{\rm max} = 1]$ and in the azimuth angle in the range $[0, 2\pi]$. The generated energy follows a power law spectrum proportional to $E_\nu^{-\gamma}$, where γ is typically 1.4. The minimum and the maximum generated energies are respectively 10^2 and 10^8 GeV. In this way, roughly the same interacting neutrinos are simulated for each energy decade. It is custom to "weight" the events in order to simulate different neutrino fluxes. Hence, the same sample of generated events can be used to simulate atmospheric and various astrophysical neutrino fluxes. A generation weight, $w_{\rm gen}$, is defined as:

$$w_{\rm gen} = V_{\rm gen} \cdot t_{\rm gen} \cdot I_\theta \cdot I_E \cdot E^\gamma \cdot \sigma(E_\nu) \cdot \rho \cdot N_{\rm A} \cdot P_{\rm Earth} \tag{4.4}$$

where $V_{\rm gen}$ is the generation volume, $I_\theta = 2\pi \times (\cos(\theta_{\rm max}) - \cos(\theta_{\rm min}))$ is the angular phase space factor, $I_E = (E_{\rm max}^{1-\gamma} - E_{\rm min}^{1-\gamma})/(1-\gamma)$ is the energy phase space factor, $\rho \cdot N_{\rm A}$ the number of target nucleons per unit volume and $t_{\rm gen}$ the interval of time simulated (usually a year). The simulation of a particular neutrino flux, $\phi^{\rm test}(E_\nu, \theta_\nu)$, is done by re-weighting all the events in each energy and zenith bin by the factor $\phi^{\rm test}(E_\nu, \theta_\nu) \cdot w_{\rm gen}$.

For the analysis presented in this thesis, events are weighted according to the Bartol flux [55] for atmospheric neutrinos up to 100 TeV [136]. An energy spectrum proportional to E_ν^{-2} is adopted for the signal neutrinos unless stated otherwise.

The propagation of the muon from the neutrino interaction vertex to the so-called "can" is simulated with the MUSIC [137] package. The "can" is a cylinder which surrounds the detector for 2-3 light attenuation lengths. The Cherenkov light emitted by particles outside the can cannot reach the detector and therefore does not need to be simulated. The can

and the detector geometry for event generation are shown in Figure 4.6.

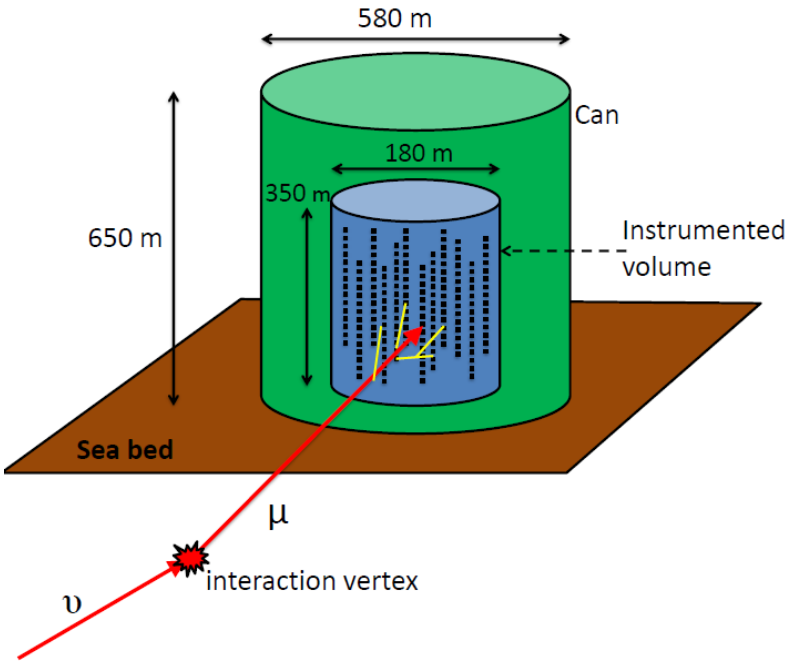

Figure 4.6.: Detector geometry for the event generation.

Atmospheric muons

Atmospheric muons events are simulated with MUPAGE v3r5 [138], which uses parametric formula to describe the flux, the angular distribution and the energy spectrum of underwater muon bundles of any multiplicity [139]. Events can be simulated for depths between 1.5 and 5 km w.e. and for zenith angles smaller than 85 degrees. The output of the program contains the values of the position, direction and energy of the muons at the can surface.

4.2.2. Light propagation and detector simulation

Light propagation

Particles are propagated inside the can using consecutively the GEASIM v4r10 [140] and the KM3 v3r7 [141] programs which are both based on the GEANT package [142].

Full GEANT tracking of hadronic showers is performed by GEASIM. For each particle, the arrival time of the Cherenkov light incident on the OMs is computed. The attenuation of the light is included, but the photon scattering is not simulated. The relative orientation of the PMTs with respect to the Cherenkov cone and the OM angular acceptance are included at this stage.

KM3 simulates the propagation of the muons in steps of 1 m. Due to the very large number of secondary electrons at high energies, the tracking of all the electromagnetic showers and the photons would require a lot of CPU time. KM3 avoids this problem by using photon tables which store the number and the arrival time of hits on OMs for different distances, positions and orientations of the OMs with respect to the track. Absorption and scattering of the light in water are both taken into account.

Detector simulation

The response of the detector is simulated with the TriggerEfficiency program [132] which adds of optical background hits to those produced by neutrinos or muons. It also simulates the electronics and the trigger algorithms.

Optical background hits are generated according to a Poisson probability distribution based on measured rates in order to take into account all the background contributions (radiactive decay and biological activities) for each run. In this way, the data taking conditions of all runs are reproduced. The condition of the detector, such as the fraction of inactive OMs due to high rate veto, are also reproduced. The electronics response is simulated by summing the number of photons detected during the time window of signal integration in the ARS chip ($\sim$ 40 ns). In order to take into account the time resolution for single electronic signals, typically 1.3 ns, the hit times are smeared with a Gaussian function with width

$$\sigma = \frac{1.3}{\sqrt{(N_\gamma)}}\ \mathrm{ns}, \tag{4.5}$$

with N_γ the number of detected photons. It was found [143] that the resulting distribution differs from the real distribution of the TTS obtained by measuring the time response of a 10 inch PMT to a single photo-electron. This discrepancy affects the agreement between data and Monte Carlo as will be explained in Section 5.1.

For each ARS, the simulated deadtime is 250 ns.

The simulation of the charge resolution of signal hits is done using a Gaussian distribution with mean 1 (1 photoelectron for a single photon) and width of 0.3 p.e. The simulation of the charge distribution of the random background is obtained from data. In the TVC calibration, the walk effect is taken into account.

After this stage, the same trigger algorithms used for the corresponding data runs are applied.

4.3. Track reconstruction

The reconstruction algorithm estimates the direction and the position of the muon with a multi-step fitting procedure [133]. The initial steps provide a starting point for the final maximisation of the track likelihood. The likelihood is defined as the probability density function of the observed hit time residuals r, given the track parameters. The time residual r_i is the difference between the observed and theoretical hit time for the assumed track parameters:

$$r_i = t_i - t_i^{th}. \tag{4.6}$$

The distribution of the hit time residuals for reconstructed neutrino tracks is shown in Figure 4.7. The peak around zero is due to Cherenkov photons emitted by a muon and detected by the OMs in the absence of scattering. Thus, their arrival time is mostly affected by the TTS of the PMT and by dispersion. The tail of the distribution is caused by scattered photons and photons from secondary electrons. Optical background photons produce a flat distribution of time residuals.

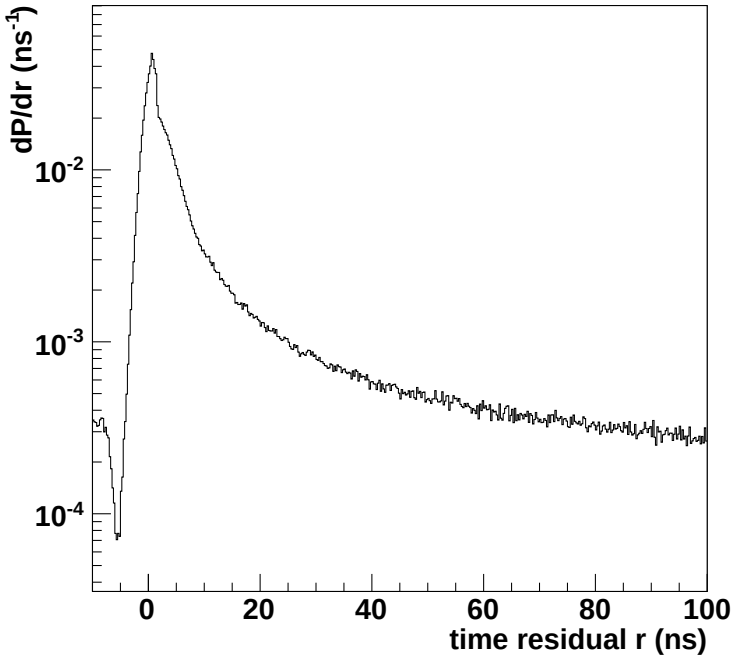

Figure 4.7.: Distribution of the reconstructed hit time residual for simulated neutrinos.

The track reconstruction starts with a linear fit through the positions associated with the hits with the hit time as independent variable. The distance of the muon track from the OM is estimated using the amplitude information and the orientation of the PMT. It is expected that a PMT recording a hit with high amplitude is located close to the track. This leads to the following relation:

$$\mathbf{y} = \mathbf{H\Theta}, \tag{4.7}$$

where $\mathbf{y} = [x_1, y_1, ..., z_n]$ is the vector of the hit positions, $\mathbf{\Theta} = [p_x, d_x, p_y, d_y, p_z, d_z]^{\mathrm{T}}$ is

the vector containing the track parameters and $\mathbf{H}$ is a matrix which contains the hit times:

$$\mathbf{H} = \begin{bmatrix} 1 & ct_1 & 0 & 0 & 0 & 0 \\ 0 & 0 & 1 & ct_1 & 0 & 0 \\ 0 & 0 & 0 & 0 & 1 & ct_1 \\ 1 & ct_2 & 0 & 0 & 0 & 0 \\ 0 & 0 & 1 & ct_2 & 0 & 0 \\ 0 & 0 & 0 & 0 & 1 & ct_2 \\ \vdots & \vdots & \vdots & \vdots & \vdots & \vdots \\ 0 & 0 & 0 & 0 & 1 & ct_n \end{bmatrix} \tag{4.8}$$

An analytical χ^2 minimisation is applied to estimate the track parameters, $\hat{\mathbf{\Theta}}$:

$$\chi^2 = [\mathbf{y} - \mathbf{H}\hat{\mathbf{\Theta}}]^{\mathrm{T}}\mathbf{V^{-1}}[\mathbf{y} - \mathbf{H}\hat{\mathbf{\Theta}}], \tag{4.9}$$

with $\mathbf{V}$ the error covariance matrix which contains the error estimates on the hit positions.

The second step of the reconstruction algorithm is the M-estimator fit. M-estimators [144, 145] maximise some function g (in this case $g(r)$) and can be considered as more general cases of maximum likelihood fits. The function maximised by the M-estimator is

$$g = \sum_i g(r_i) = \sum_i -2\sqrt{1 + r_i^2/2} + 2, \tag{4.10}$$

where the sum runs over all the hits with time residuals from -150 ns to 150 ns and distances smaller than 100 m from the first track fit result are used..

It has been found that the M-estimator fit is not as accurate as a maximum likelihood fit but it is less sensitive to the quality of the starting point.

The third step consists of a maximum likelihood fit. Hits are selected if their residuals are in the range $[-0.5 \times \mathrm{R}, \mathrm{R}]$ where R is the root mean square of the residuals used for the M-estimator fit. Coincidence hits are also selected. At this stage, a simplified version of the full likelihood is used.

Both the M-estimator and the maximum likelihood fit are repeated using nine different starting points to further increase the probability of finding the global minimum.

The last step is a maximum likelihood fit with an improved likelihood function. This final likelihood function uses parametrisations for the probability density function (PDF) of the signal hit time residuals, derived from simulations. The PDF also takes into account hits arriving late due to Cherenkov emission by secondary particles or light scattering. The probability of a background hit is also included.

The quality of the track fit is quantified by the variable

$$\Lambda \equiv \frac{\log L^{\max}}{N_{\mathrm{hits}} - 5} + 0.1 \times (N_{\mathrm{comp}} - 1) \tag{4.11}$$

where $L^{\max}$ is the maximum value of the likelihood, $N_{\mathrm{hits}} - 5$ is the number of degrees of freedom which is the number of hits used in the fit, N_{hits}, minus the number of fit parameters. N_{comp} is the number of times the repeated initial steps of the reconstruction

converged to the same result. In general, $N_{\mathrm{comp}} = 1$ for most of the badly reconstructed events while it can be as large as nine for well reconstructed events. The coefficient 0.1 in Equation 4.11 was chosen to maximise the separation in Λ between signal and mis-reconstructed downgoing muons.

In general, well reconstructed events have larger Λ. The Λ variable can thus be used to reject badly reconstructed events, in particular mis-reconstructed atmospheric muons.

Figure 4.8 shows the distribution of the reconstruction angle, α, i.e. the angle between the generated neutrino and the reconstructed muon direction, is plotted. After requiring a cut $\Lambda > -5.2$ most of the badly reconstructed events are rejected.

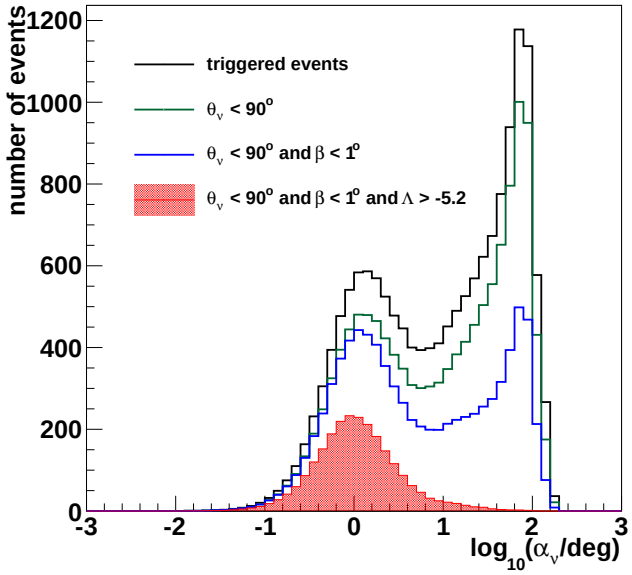

Figure 4.8.: Distribution of α, i.e. the angle between the generated neutrino and the reconstructed muon direction, for simulated atmospheric neutrinos before and after applying the event selection cuts described in Section 6.2.

Figure 4.9 (top) shows the reconstruction angle α as a function of the Λ variable for simulated atmospheric neutrinos. The bottom plot shows a profile distribution [146] of these two variables. The error bars represent the standard deviation of the α distribution. A comparison between atmospheric and E^{-2} neutrinos is shown for the same quantities.

Error estimates of the track direction are provided by the reconstruction algorithm under the assumption that the likelihood function near the fitted maximum follows a multivariate Gaussian distribution. The error estimates, which are elements of the error covariance matrix, are computed from the second derivatives of the likelihood function at the fitted

maximum:

$$[\mathbf{V}^{-1}]_{ij} = -\frac{\partial^2 \log(L)}{\partial x_i \partial x_j} \tag{4.12}$$

where $\vec{x}$ is the vector of track parameters: $\vec{x} = (p_x, p_y, p_z, \theta, \phi)$. The estimated error on the zenith and azimuth angles, $\hat{\sigma}_\theta$ and $\hat{\sigma}_\phi$, are of particular interest. Figure 4.10 shows the pull distributions for the zenith (top) and azimuth (bottom) angles. A pull is defined as the ratio between the true error on a variable and its error estimate. Ideally, the pull distribution should be Gaussian with mean zero and width $\sigma = 1$. As can be seen from Figure 4.10 the width of the two pulls is larger than one. This is due to the fact that the PDF is not a perfect description of the residuals in the Monte Carlo simulations. This is partially due to the 2 ns smearing which will be discussed in details in Section 5.1.

From the estimated errors on the zenith and azimuth angles, it is possible to compute the estimate of the error on the direction of the muon track, β, which will be used to reject mis-reconstructed atmospheric muons:

$$\beta = \sqrt{\sin^2(\hat{\theta})\hat{\sigma}_\phi^2 + \hat{\sigma}_\theta^2}. \tag{4.13}$$

The distribution of β is shown in Figure 6.9.

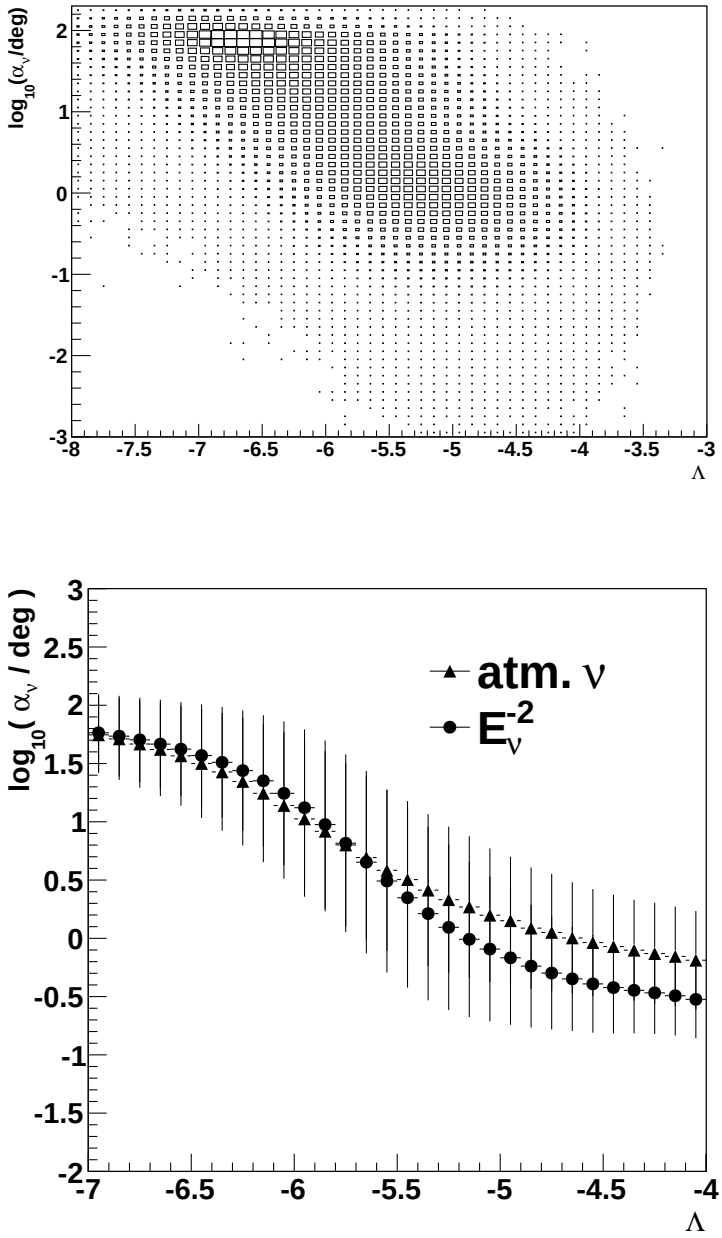

Figure 4.9.: Top: reconstruction angle α vs Λ for atmospheric neutrinos. Bottom: Profile distribution of these two quantities. A comparison between atmospheric and E^{-2} neutrinos is shown.

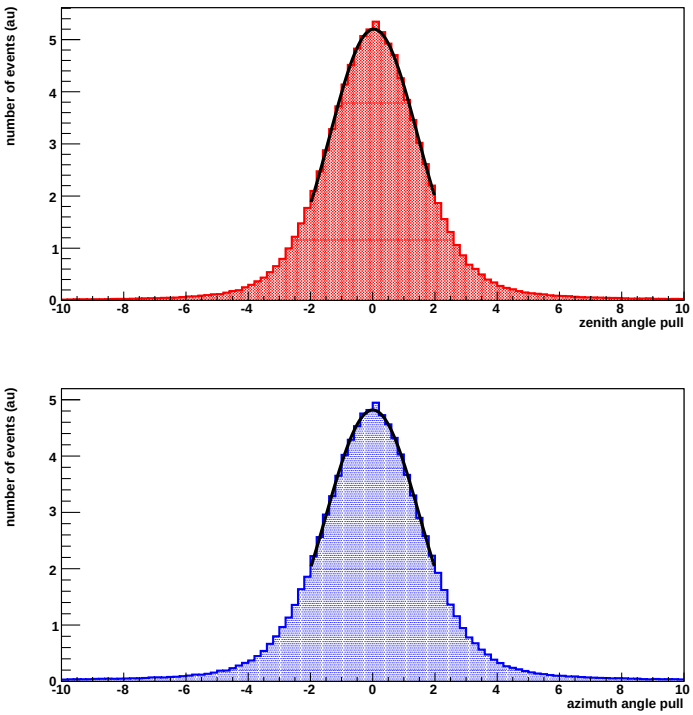

Figure 4.10.: Pull distributions for the zenith (top) and azimuth (bottom) angle for a simulated sample of neutrinos. A quality cut $\Lambda > -5.2$ is applied. A Gaussian function between -2 and 2 is used to fit the distribution. The width of the Gaussian is $\sigma = 1.41$ for the zenith angle pull and $\sigma = 1.51$ for the azimuth angle pull.

5. Systematic studies

As for me, all I know is that I know nothing.

Socrates

In this chapter we outline the main sources of systematic uncertainties in the analysis. To constrain the angular resolution and the acceptance of the detector, we have studied the agreement of Monte Carlo simulations with data while varying two quantities

- **Time resolution.** The systematic uncertainty on the angular resolution has been estimated by varying the hit time resolution. At the reconstruction stage, the hit times have been "smeared" by Gaussians with $\sigma = 1, 2$ and 3 ns.
- **OM acceptance.** The uncertainty on the detector acceptance, was studied with special Monte Carlo datasets in which the efficiency of each of the OMs was reduced by 15%.

As this study requires production of a MC sample for each variation, it was performed on a limited MC sample, corresponding to the 2008 data. The results obtained have a general validity and can be applied to the full period of data considered as was shown in [147].

Section 5.1 describes the acceptance studies, while in Section 5.2 the angular resolution studies are reported. In all the following plots, atmospheric muons have been simulated with the CORSIKA package [148] using the Bugaev model [149] for the primary flux since the MUPAGE production used for the analysis was not available yet at the time of this study.

5.1. Hit time resolution studies

In order to study the systematic uncertainty on the angular resolution, we produced new Monte Carlo sets where the hit time resolution has been increased. In this way, it is possible to estimate the impact of a degraded timing resolution on the angular resolution. A degraded timing resolution could be due to possible timing offsets, mis-alignments and inaccuracies in the light propagation model.

On the other hand, the simulations can be compared to data to constrain the magnitude of a possible timing degradation. This indirectly allows to constrain the angular resolution with data.

The distribution of Λ without any additional time smearing is shown in Figure 5.1 (top). In general, the simulations underestimate the data. However, there is a large uncertainty

on the CR flux, 50% [150] for the atmospheric muon and 30% [136] for the atmospheric neutrino flux. For high values of Λ ($\Lambda > -5.3$) the MC over-predicts the data.

Figure 5.1 (bottom) shows the Λ distribution for upgoing events. Also in this case the additional time smearing is not applied. The number of neutrino events in the region with high values of Λ is also over-predicted by the MC. The over-prediction of simulations over data is something which requires further investigation. The data contain too few well reconstructed events. This could be a hint that the assumptions in the simulation are too optimistic.

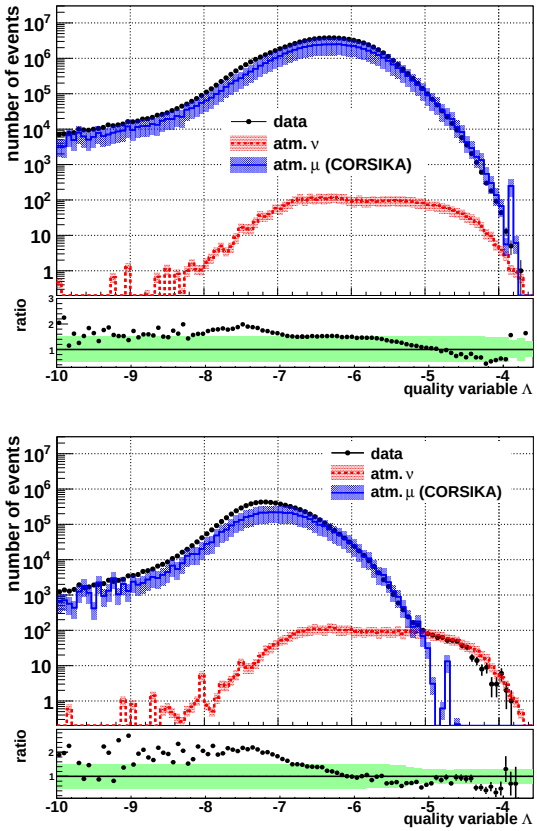

Figure 5.1.: Top: distribution of the variable Λ for reconstructed events. The hit time resolution has not been deteriorated. The bottom plot shows the same but for reconstructed upgoing events

Figure 5.2 shows the effect of increasing the hit time resolution on the distribution of Λ for all triggered events: a smearing of 1, 2 and 3 ns has been applied. Deteriorating the hit time resolution with an additional time smearing of 1 ns has a small impact as

expected[1]. A smearing of 2 ns improves the agreement between data and MC: the ratio between data and simulation is rather flat, indicating that the shape of the Λ distribution in data is well reproduced by the simulation. This is consistent with the uncertainties on both the atmospheric muon and neutrino flux normalisations. With a smearing of 3 ns, the MC underpredicts the data.

The same distributions but for upgoing events are shown in Figure 5.3. Also for this case, the best agreement between data and MC is obtained with a smearing of 2 ns.

5.2. Acceptance studies

Without applying any reduction in the OM efficiency and with a 2ns smearing, there is an overall excess of downgoing muons in data compared to the Monte Carlo of roughly a factor 1.5. This is shown in the middle plot of Figure 5.2.

Figure 5.4 shows the Λ distribution for a 15% reduction in the OM acceptance. The discrepancy between data and MC is now increased to more than a factor 2. Thus, it seems that the data favor the simulation with the default acceptance.

In order to investigate the behaviour of atmospheric neutrinos with a 15% reduction in the OM efficiency, we show in Figure 5.5 the Λ distribution for upgoing events only. The ratio between data and simulations is now around 1.5-2. Also in the case of atmospheric neutrinos the data favor the simulation with the default OM acceptance.

To quantify the agreement between data and MC in the atmospheric neutrino region, we report in Table 5.1 the values of the data-MC ratio for $\Lambda > -5.2$ and $\Lambda > -4.8$ for the different smearings and OM efficiencies.

smearing [ns]	$\mathrm{OM_{eff}} = 100\%$	$\mathrm{OM_{eff}} = 85\%$
1	0.68(0.87)	0.82(1.48)
2	0.98(1.11)	1.61(1.77)
3	1.61(1.63)	1.88(2.23)

Table 5.1.: Ratio between data and MC for $\Lambda > -5.2(-4.8)$ for different MC samples.

In the rest of this thesis, the MC with an additional hit time smearing of 2 ns and the standard OM acceptance will be used. We will refer to it as the "default" MC.

5.3. Conclusions

In the previous sections we have compared atmospheric muon and neutrino MC datasets with degraded detector performance to the data. We now investigate the behaviour of the signal MC. Figure 5.6 shows the distribution of the angle between the true neutrino direction and the reconstructed muon direction for the MC samples with different hit-time smearing. Deteriorating the hit time resolution has two effects:

[1] The TTS is approximately 1.3 ns standard deviation, and adding 1 ns in quadrature does not significantly degrade the resolution

- It decreases the angular resolution.
- It decreases the acceptance since fewer events pass the selection criteria.

These two effects are shown in Figure 5.7.

A reduction in the OM efficiency does not deteriorate the angular resolution, but decreases the acceptance of E_ν^{-2} neutrinos to roughly 12%. The atmospheric neutrino flux would instead be reduced by 40%, a value to be compared to the 30% error on its flux normalisation. We therefore set the uncertainty on the acceptance to 15%, a conservative choice.

For a time smearing of 3 ns, the simulations show a deterioration in angular resolution of roughly 30% and the number of selected neutrino events in data exceeds the simulated neutrino signal by 2σ, where σ refers to the uncertainty on the atmospheric neutrino flux model. Assuming a linear dependency, this leads to a 1σ uncertainty on the angular resolution of $\sim 15\%$.

The 2ns time smearing was introduced to constrain the systematic uncertainty on the angular resolution and at the same time improve the agreement between data and MC. It was found after completion of the analysis [143] that this original disagreement is due to the fact that the TTS of the PMTs was not parametrised correctly. This was fixed by implementing in the TriggerEfficiency program the measured time response of a 10 inch PMT to single photo-electrons. Future analyses in ANTARES will adopt this improvement. A better angular resolution is expected.

The absolute orientation of the detector is known with an accuracy of $\sim 0.1^\circ$ as mentioned in Section 3.4.2. Table 5.2 reports all the values of the systematic uncertainties of the analysis described in this thesis with the exception of the systematic uncertainties on the background rate and the number of hits used in the reconstruction which will be described in Section 7.5.1.

What?	Value
Acceptance	15%
Angular resolution	15%
Absolute orientation	0.1°
Atmospheric muons	50%
Atmospheric neutrinos	30%

Table 5.2.: Summary of the systematic errors adopted in this analysis. The first three rows show the systematic uncertainties of important detector parameters. The last two rows refer to the systematic uncertainties of the simulations.

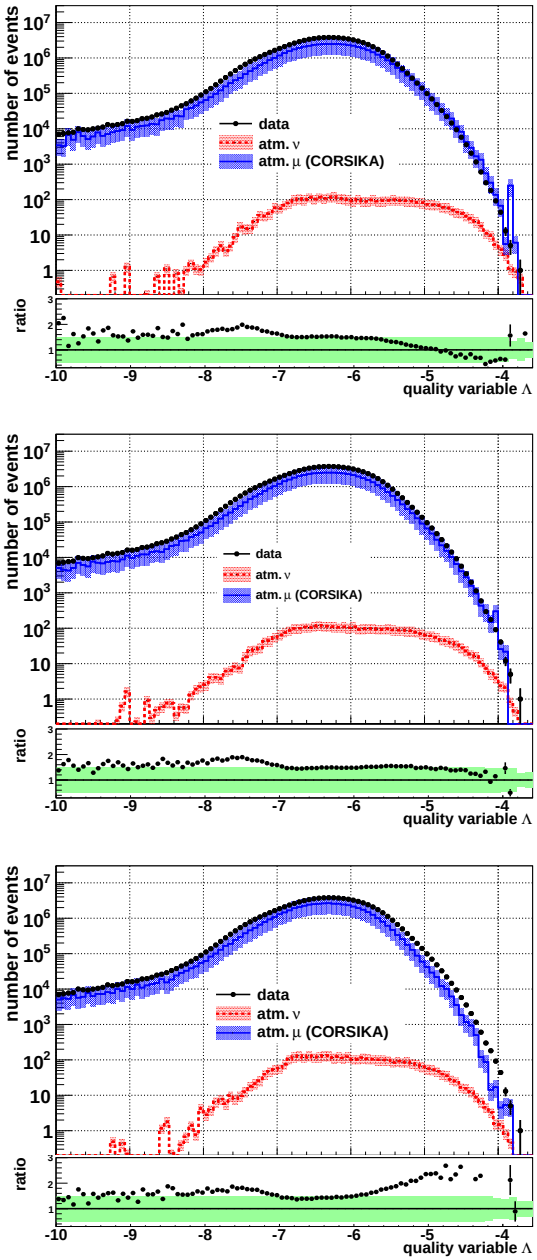

Figure 5.2.: Distribution of the variable Λ for reconstructed events. In the simulation the hit time resolution has been deteriorated by an additional 1, 2 and 3 ns in reading order.

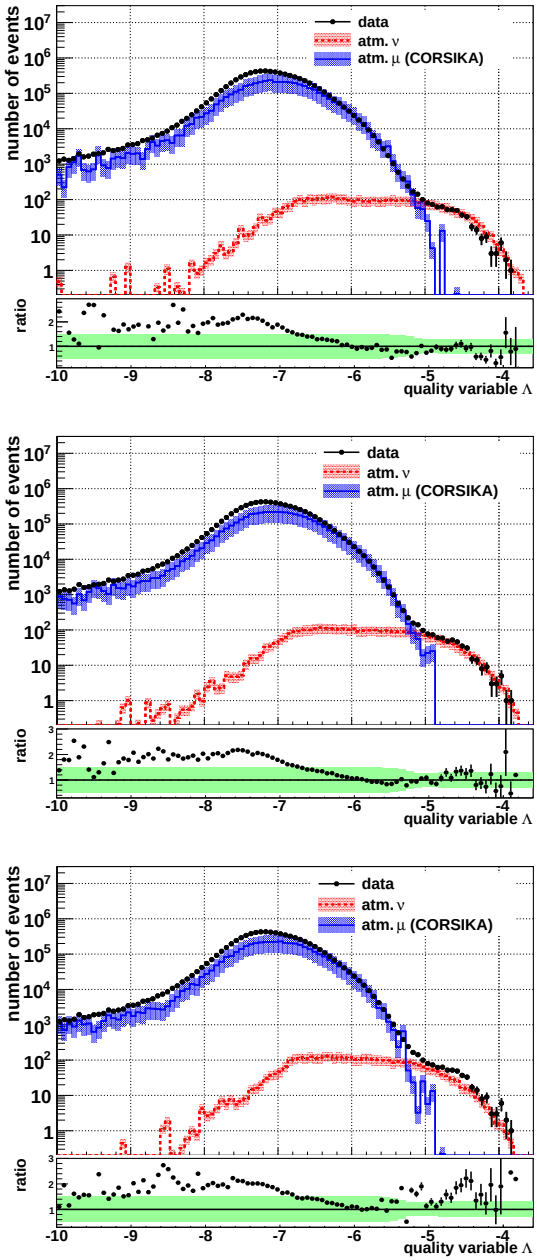

Figure 5.3.: Distribution of the variable Λ for upgoing events. In the simulations the hit time resolution has been deteriorated by an additional 1, 2 and 3 ns in reading order.

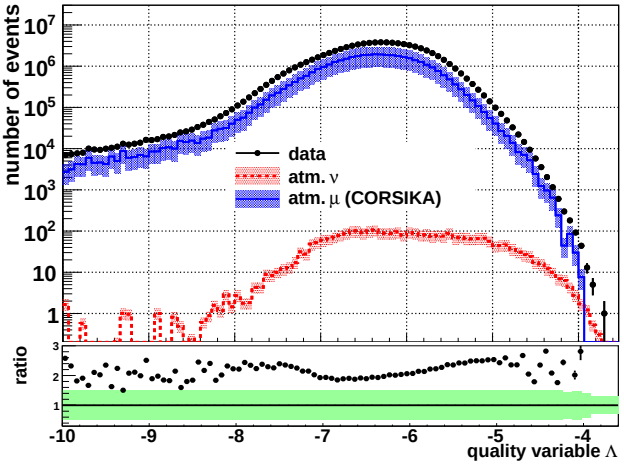

Figure 5.4.: Distribution of the quality variable Λ for all reconstructed events with the OM efficiency reduced by 15%. A 2ns smearing to the hit time resolution was also applied.

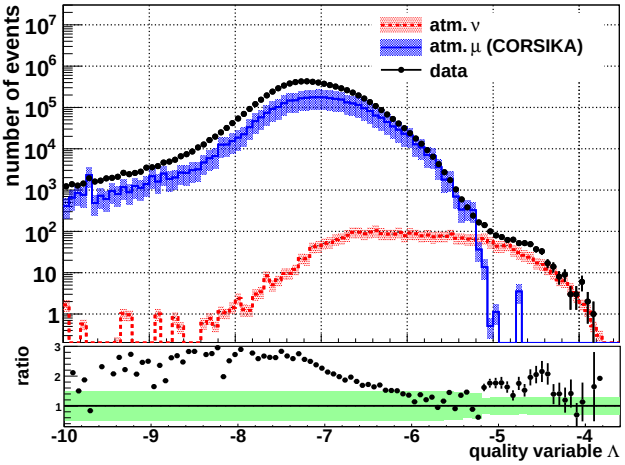

Figure 5.5.: Distribution of the quality variable Λ for upgoing events. The OM efficiency has been reduced by 15%. A 2ns smearing to the hit time resolution was also applied.

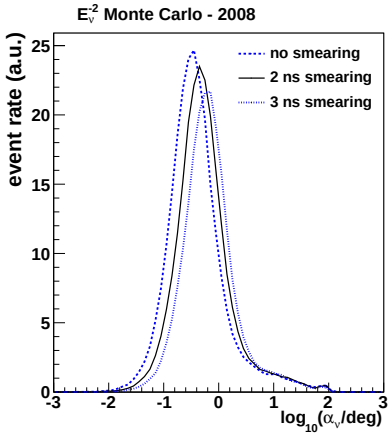

Figure 5.6.: Distribution of the reconstruction angle α for events simulated assuming a spectrum proportional to E_ν^{-2}. The solid line shows the default MC with a 2 ns smearing. The dashed line refers to the MC with no smearing of the hit time resolution and the dotted line shows the result for a MC dataset with a smearing of 3 ns. The same distribution for the MC with 1 ns smearing is not shown for clarity.

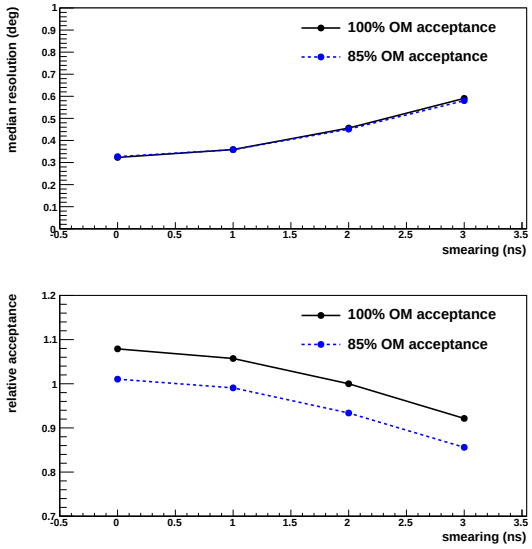

Figure 5.7.: Left: median angular resolution for signal events simulated assuming an E_ν^{-2} spectrum for the MC sets with a reduction of 15% in the OM acceptance (dashed blue line) and without it (black line). Right: acceptance relative to the default MC (with a smearing of 2 ns) for the same MCs.

6. Event selection and data/MC comparison

I have done something very bad today by proposing a particle that cannot be detected; it is something no theorist should ever do.

Wolfgang Pauli

We now present the sample of neutrino candidates used for the search for point-like sources. The agreement between data and Monte Carlo is also discussed. First, we discuss the run selection and data taking conditions for the period of data considered

6.1. Selection of the runs

The data used for the analysis presented in this thesis were collected during the period January 2007 to December 2010. The first run considered started at 12:57 on January 28th 2007. Five strings were operational at that time. The data taking continued with this detector configuration until December 7^{th} 2007 when other five lines were deployed. During the period from the 3rd of March 2008 to the 25th of May, line 4 suffered a problem which prevented any communication with the junction box. Data taking in that period continued with 9 strings. During a three day sea campaign at the end of May 2008, line 4 was re-connected together with line 11 and line 12. On the 30th of May 2008 data taking with the completed detector started. Several detector maintenance operations occured during 2009 due to problems with Line 12, 9 and 6. Line 6 was recovered on the 27th of October 2009 and re-connected only one year after. The last run used in this analysis was taken on the 31st of December 2010. The run numbers, the corresponding data taking periods and the number of detector strings for each period are summarised in Table 6.1.

The run selection consists of a set of "sanity checks" of the data. This prevents inclusion of runs with synchronisation problems in the DAQ system and with non-physical event rates. Experimental runs which are used e.g. to test new calibrations or H.V. settings are also excluded. The livetime of the excluded runs is roughly 150 days.

The livetime of the selected 7419 runs is 813 days (of which 183 days correspond to the five line period as summarised in Table 6.2). The duty cycle is around 60% though it is increasing every year. Loss of efficiency is mainly due to periods of high bioluminescence and sea operations.

Run number	Data taking period	Number of lines
25700 - 30460	January - December 2007	5
30508 - 32491	December 2007 - March 2008	10
32529 - 34417	March - May 2008	9
34419 - 41671	May 2008 - October 2009	12
41673 - 52896	October 2009 - November 2010	11
52896 - 54250	May 2008 - December 2010	12

Table 6.1.: Data taking periods and the corresponding run numbers. The number of detector strings which were operational during each period is also shown.

Period/Configuration	Number of runs	Livetime [days]	Duty cycle
All	7419	813	58%
5 lines	1396	183	57%
12 lines	6023	630	60%
2007	1469	192	53%
2008	1987	181	50%
2009	1644	208	57%
2010	2319	232	64%

Table 6.2.: Livetime and number of runs for different data taking periods. The last column shows the data collection efficiency.

6.1.1. Sparking runs

A small number of runs contain events with an exceptionally high hit multiplicity. As an example, Figure 6.1 (left) shows the distribution of the number of hits for a run where this happens. It is believed that this is due to "sparking" OMs, i.e. OMs where the PMT suffers an high voltage surge. Although these high multiplicity events are not reconstructed with large values of Λ, meaning that they would not be selected as neutrino candidates, we veto these runs. Twenty-five runs were identified as "sparking", corresponding to roughly two days of livetime.

6.1.2. High baseline runs

In Figure 3.15 (top) we showed the distribution of the baseline for the period of data considered. Two periods of high baseline rate are clearly distinguishable. They correspond to the period of data taking May - August 2009 and August - September 2010. The Λ-distribution for events in these periods is compared to the rest of the data in Figure 6.2. It exhibits a contribution of events (around $\Lambda \simeq -7$) which is thought to consist of

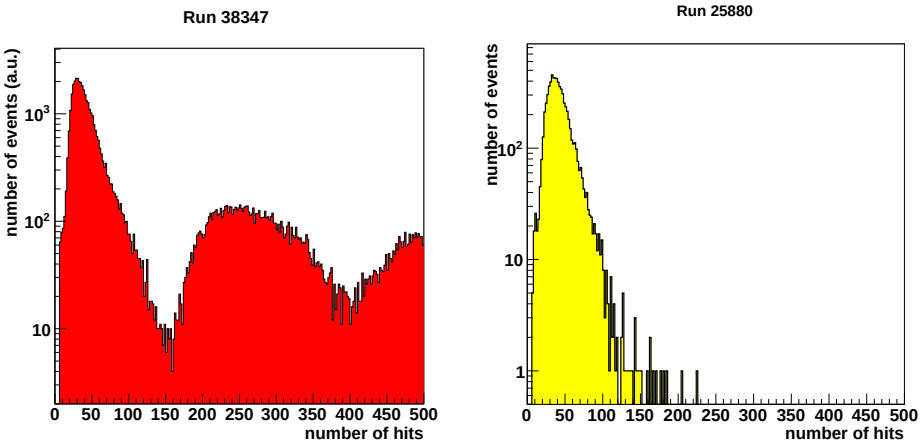

Figure 6.1.: Left: number of hits for the run 38447 showing an excess of high multiplicity. These excess is attributed to sparking OMs. Right: number of hits for run 25880 with no excess of high multiplicity.

only optical background, (the events at higher values of lambda are due to atmospheric muons). However, the selection of the sample relies on a cut on $\Lambda > -5.2$ which rejects these events.

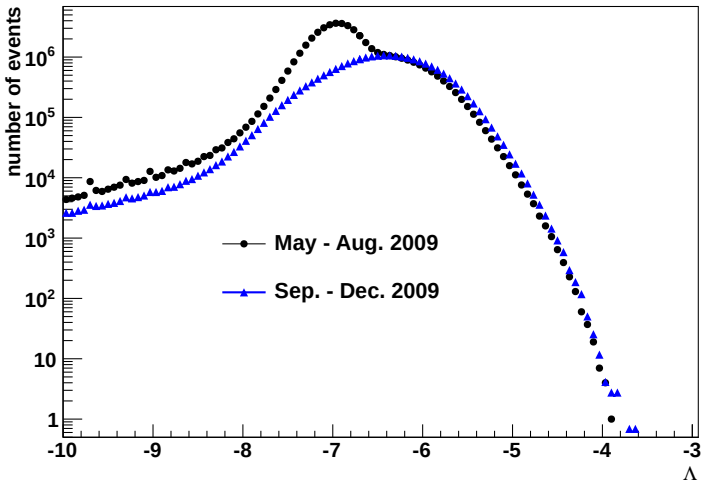

Figure 6.2.: Λ distribution for two periods of data taking. The peak around $\Lambda \simeq -7$ is explained by high optical background.

6.2. Event selection

The cuts applied to select neutrino candidates serve to reject the background due to cosmic rays. They are:

- $\theta < 90^\circ$. Neutrino candidates events are first selected requiring tracks reconstructed as upgoing. With this cut, and without applying any other, it has been estimated that 90% of the atmospheric muons and 20% of the atmospheric neutrinos are rejected.
- $\beta < 1^\circ$. The estimated angular uncertainty on the muon track direction, β, defined in Section 4.3, is required to be smaller than 1 degree. The error estimate on the direction of the reconstructed muon track is an important variable for the discrimination of the mis-reconstructed atmospheric muons. Figure 6.3 shows the distribution of β for both signal neutrinos reconstructed within 2 degrees of the true neutrino direction and for upgoing atmospheric muons. Most of the signal events have values of β smaller than 1 degree. The cut $\beta < 1^\circ$ rejects 47% of the mis-reconstructed atmospheric muons.

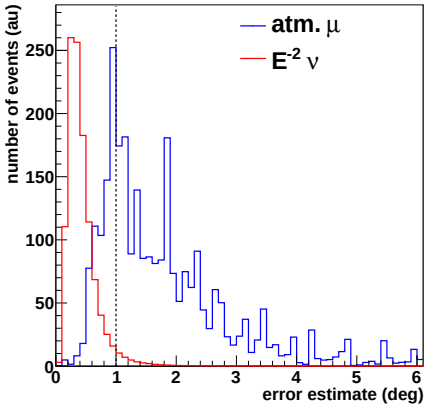

Figure 6.3.: Distribution of the estimated angular uncertainty, β, for E_ν^{-2} signal neutrinos (red) and for upgoing mis-reconstructed atmospheric muons (blue). The vertical dashed line indicates where the selection cut is applied ($\beta < 1^\circ$).

- $\Lambda > -5.2$. To further reject mis-reconstructed atmospheric muons, events with the quality variable Λ larger than -5.2 are selected. This value was chosen to optimise the neutrino flux needed to have a 50% chance of discovering the signal at the 3σ (or 5σ) significance level assuming an E_ν^{-2} spectrum. Table 6.4 shows the values of the flux needed for discovery for a ν-source at three declinations [1]. Among the three Λ cuts, $\Lambda > -5.2$ gives the lowest, i.e. best, discovery potentials.

The effect of the selection cuts on data, expected background and signal efficiency are summarised in Table 6.3

The selected sample consists of 3058 neutrino candidate events out of a total of roughly 4×10^8 triggered events. From Monte Carlo simulations, it has been estimated that the

[1] The values presented here are for a candidate list search (see Chapter 7).

Cut	Data	Atm. μ	Atm. ν	$E_\nu^{-2}\nu$[%]	$E_\nu^{-2}\nu(\alpha < 1^o)$[%]
Triggered events	3.94×10^8	3.06×10^8	1.54×10^4	100	100
$\theta < 90^\circ$	6.08×10^7	2.98×10^7	1.24×10^4	61	57
$\theta < 90^\circ + \beta < 1^\circ$	3.90×10^7	1.57×10^7	8352	44	53
$\theta < 90^\circ + \beta < 1^\circ + \Lambda > -5.2$	3058	358	2408	23	44

Table 6.3.: Number of events before and after applying the selection cuts described in the text for data (second column) and Monte Carlo simulations. The fourth column shows the percentage of signal events assuming a neutrino flux proportional to an E_ν^{-2} spectrum. The last column the same but for signal events reconstructed within 1 degree from the true direction.

$\Lambda >$	δ [°]	$n_{5\sigma}$	$\phi_{5\sigma}$ [$\mathrm{GeV}^{-1}\,\mathrm{cm}^{-2}\,\mathrm{s}^{-1}$]
-5.0	-70	4.43	6.42×10^{-8}
-5.2	-70	5.08	6.09×10^{-8}
-5.4	-70	6.42	6.7×10^{-8}
-5.0	-30	4.33	9.19×10^{-8}
-5.2	-30	4.82	8.36×10^{-8}
-5.4	-30	5.83	8.74×10^{-8}
-5.0	10	3.88	1.17×10^{-7}
-5.2	10	4.29	1.04×10^{-7}
-5.4	10	6.38	1.33×10^{-7}

Table 6.4.: For three different declinations (second column) and cuts on Λ (first column) discovery potentials are computed: mean number of signal events (fourth column) and flux (last column) needed to claim a 5σ discovery. The cut $\Lambda > -5.2$ optimises it.

atmospheric muon contamination of this sample is around 14% (see Table 6.3). A Galactic sky map of these events is given in Figure 6.4.

6.3. Data - Monte Carlo comparison

The comparison between data and simulations is an important step for the kind of analysis. Good agreement between data and MC represents a hint of good understanding of the physics processes and detector response of the experiment.

The Monte Carlo used in this analysis corresponds to a run-by-run simulation [151]. Using the measured optical background rates, OM conditions and run duration, a realistic simulation of the physics and data taking process for each run is obtained.

Figure 6.5 shows the cumulative distribution of the Λ variable for upgoing tracks. The cut $\beta < 1^\circ$ is also applied. Overall, the agreement between data and the simulations is

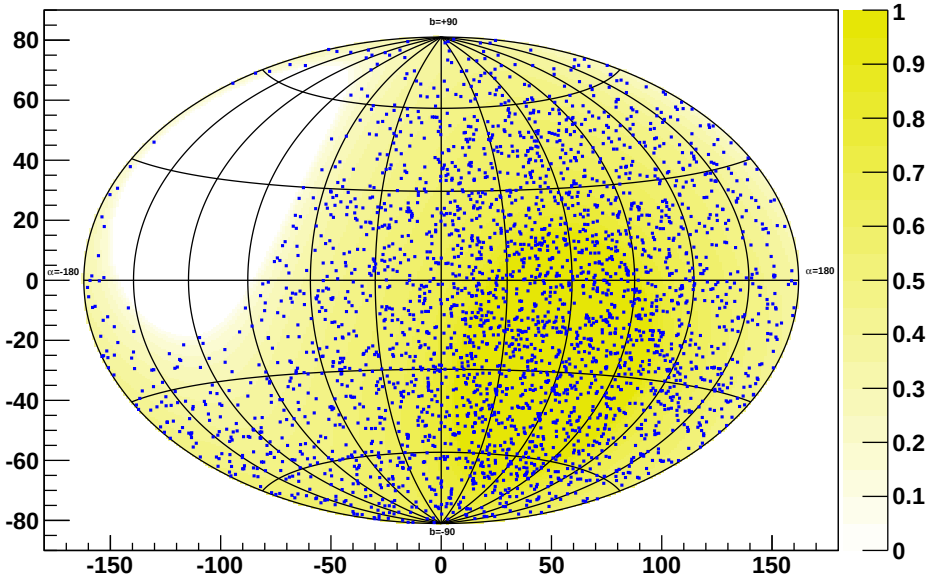

Figure 6.4.: Galactic skymap of the 3058 neutrino candidate events. The different shades of yellow indicate different visibility at the ANTARES site.

good, well within the systematic uncertainties. The excess of data compared to the Monte Carlo at the lowest value of Λ is due to the non-simulated contribution of events consisting of solely optical background as already discussed in Section 6.1.2.

Figure 6.6 shows the distribution of the selected run numbers. In general, the predictions underestimate the data and the ratio data/MC is around 1.4 for most of the period considered. The two periods of high bioluminescence responsible for the peak at $\Lambda \simeq -7$ in Figure 6.2 are clearly distinguishable from the large discrepancy between data and Monte Carlo. The zenith angle distribution with (bottom) and without quality cuts (top) is shown in Figure 6.7. The agreement between data and MC improves after requiring well reconstructed tracks. The azimuth angle distribution is shown in Figure 6.8 again for triggered events only (top) and event passing the quality cuts $\Lambda > -5.2$ and $\beta < 1^\circ$ (bottom).

Finally, in Figure 6.9 and Figure 6.10 we show the distribution of the angular error and the number of hits respectively. For the first plot, upgoing tracks with $\Lambda > -5.2$ are selected. For the distribution of the number of hits, all the final cuts are applied. Five events with large values of $N_{\rm hits}$ are not modelled by the simulations. These five events have high values of Λ, meaning that it is unlikely that they are mis-reconstructed upgoing muons. We cannot exclude that these events are due to an unknown sparking OM although this is unlikely since sparking runs have lower values of Λ. Table 6.5 shows the run number, the frame index, the values of $N_{\rm hits}$ and Λ, and the number of lines in the reconstruction for these events.

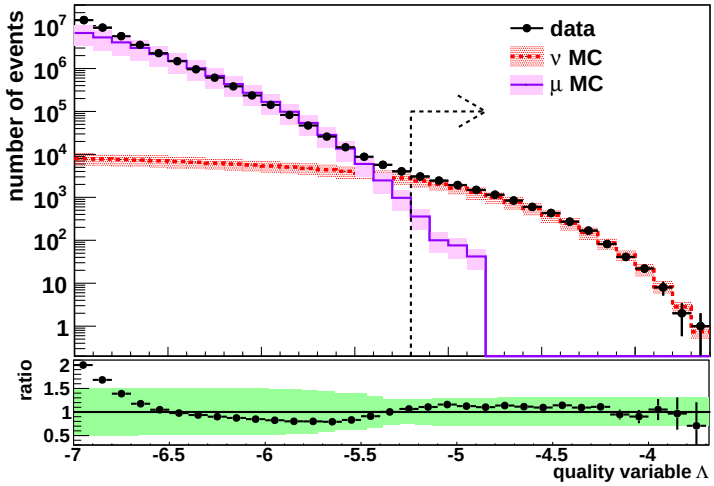

Figure 6.5.: Cumulative distribution of Λ for upgoing tracks. The cut on the angular error estimate $\beta < 1^\circ$ is also applied. The arrow shows where the selection cut is applied ($\Lambda > -5.2$). The magenta histogram represents atmospheric muons simulated with the MUPAGE package and the red histogram is for atmospheric neutrinos (upgoing and downgoing) weighted with the Bartol flux. The ratio of the data over the Monte Carlo is also shown. This is also valid for the following plots.

Evt ID	Run number	Frame index	$N_{\rm hits}$	Λ	$N_{\rm lines}$
1	35473	7183	152	-4.7	11
2	35583	58091	157	-4.8	8
3	46018	14072	150	-4.5	7
4	49420	33730	148	-4.7	9
5	28702	77100	147	-4.8	5

Table 6.5.: For the five events with large values of number of hits shown in Figure 6.10, we report in this table the run number (second column), the frame index (third column), the value of $N_{\rm hits}$ (fourth column), the value of Λ (fifth column) and the number of lines hitted by Cherenkov photons emitted by these events (last column).

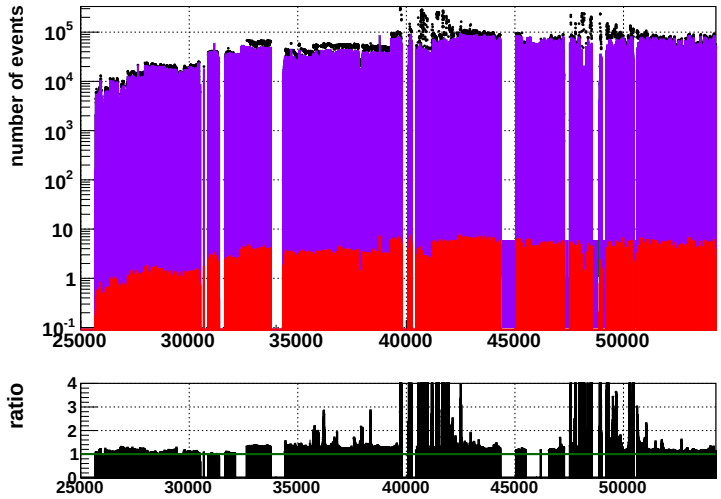

Figure 6.6.: Run number distribution of all reconstructed events passing either the 2T3 or the 3N trigger. This plot illustrated the run-by-run MC scheme as all runs in the data are simulated. Data are in general underestimated by the MC predictions. The two period of high baseline discussed in Section 6.1.2 can be identified by the large data - MC discrepancy.

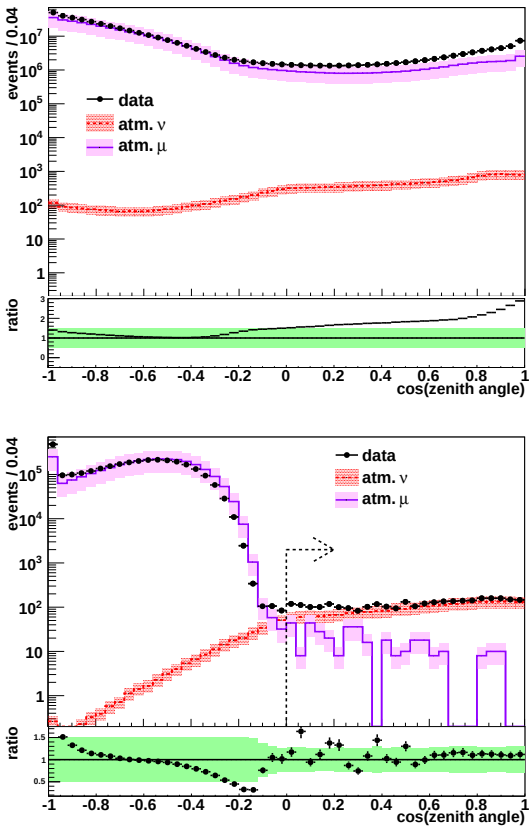

Figure 6.7.: Distribution of the cosine of the zenith angle for all triggered events (top) and for events passing the quality criteria $\Lambda > -5.2$ and $\beta < 1^\circ$ (bottom). The dashed line shows the upgoing the events. The magenta and red bands show the systematic uncertainties on the simulation that were discussed in Chapter 5. In both plots, the bottom panel shows the ratio between data and MC. The green band the total systematic uncertainty.

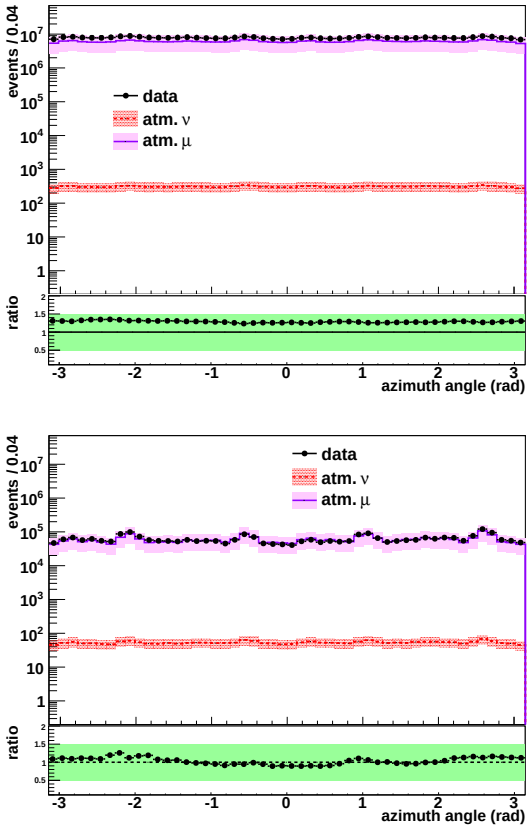

Figure 6.8.: Distribution of the azimuth angle for all triggered events (top) and for events passing the quality criteria $\Lambda > -5.2$ and $\beta < 1^\circ$ (bottom). The magenta and red bands show the systematic uncertainties on the simulation. The bottom panel in both plot shows the ratio of data over the MC. The green band indicates the total systematic uncertainty associated.

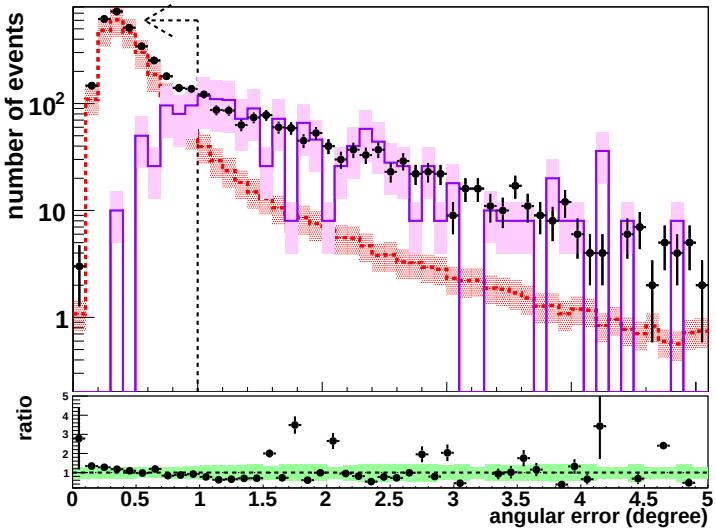

Figure 6.9.: Distribution of the angular uncertainty for reconstructed upgoing tracks after applying a quality cut $\Lambda > -5.2$. The arrow shows where the selection cut is applied.

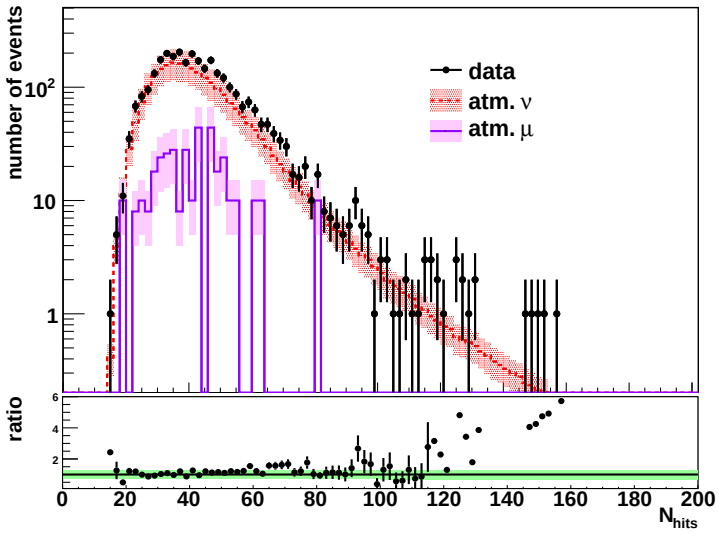

Figure 6.10.: N_{hits} distribution for upgoing selected events after applying the quality selection described in the text. Five events with large values of N_{hits} are visible at the tail of the distribution.

7. Search method

There are two possible outcomes: if the result confirms the hypothesis, then you've made a measurement. If the result is contrary to the hypothesis, then you've made a discovery.

Enrico Fermi

In this chapter we present a method to search for point-like sources of astrophysical neutrinos. It is based on an unbinned likelihood ratio method: in this way, the presence of signal events is tested by looking for an excess of events in a given direction.

Two alternative searches have been performed:

- **Full sky search.** The full sky search looks for the presence of signal events over the background anywhere in the visible sky.
- **Candidate list search.** In the candidate list search, we test for an excess of events at the locations of pre-defined candidate sources.

Throughout this chapter, we will discuss the two searches in parallel .

7.1. Hypothesis testing

The search for point-like sources of cosmic neutrinos is an example of hypothesis testing. In this context, the null hypothesis, H_0, represents the case where only background (atmospheric neutrinos and muons) is present and the alternative hypothesis, H_1, refers to the case where in addition to the background the data contain signal events.

A test statistic, $\mathcal{Q}$, is used to establish criteria to accept one hypothesis and reject the other. In a simple way, the idea is that the test statistic should have different values when H_0 is true than when H_0 is not true. The test are often performed by considering two regions: the critical region, ω, and its complement, the acceptance region, $\bar{\omega}$. If $\mathcal{Q}$ lies within the critical region then H_0 will be rejected in favour of H_1.

It can happen that H_0 is rejected even though it is true, i.e. a false discovery. This is also called type-I error, and the probability that it happens is related to the "significance" of the test, α:

$$P(\mathcal{Q} \in \omega | H_0) \equiv \alpha \equiv 1 - CL, \tag{7.1}$$

where CL is the Confidence Level of the test.

The probability to correctly reject H_0 is called the "power" of the test:

$$P(\mathcal{Q} \in \omega | H_1) \equiv \text{power}. \tag{7.2}$$

For a fixed significance, the power of the test corresponds to the sensitivity for discovering the signal.

Conversely, it is possible that the alternative hypothesis is wrongly rejected, i.e. a signal discovery is not claimed. We refer to this case as type-II error:

$$P(\mathcal{Q} \in \bar{\omega} | H_1) \equiv 1 - \text{power}. \tag{7.3}$$

7.2. Likelihood ratio method

The likelihood of the data is defined as:

$$\begin{aligned} \log \mathcal{L}_{\mathrm{s+b}} = \sum_i \log[\mu_{\mathrm{s}} \times \mathcal{F}(\alpha_{\mathrm{rec,i}}(\alpha_{\mathrm{s}}, \delta_{\mathrm{s}})) \times \mathcal{N}^{\mathrm{s}}(N^i_{\mathrm{hits}}) \\ + \mathcal{B}(\delta_i) \times \mathcal{N}^{\mathrm{bg}}(N^i_{\mathrm{hits}})] - \mu_{\mathrm{s}} - \mu_{\mathrm{bg}}, \end{aligned} \tag{7.4}$$

where the sum is over the selected events; $\mathcal{F}$ is a parametrisation of the point spread function (PSF), i.e. the PDF of reconstructing event i at an angular distance $\alpha_{\mathrm{rec,i}}$ from the source location $(\alpha_{\mathrm{s}}, \delta_{\mathrm{s}})$; $\mathcal{B}$ is a parametrisation of the background rate obtained from the distribution of the observed declination of the 3058 selected events; μ_{s} and μ_{bg} are the mean number of signal events and the total number of expected background events; N^i_{hits} is the number of hits used in the reconstruction. $\mathcal{N}^{\mathrm{s}}(N^i_{\mathrm{hits}})$ and $\mathcal{N}^{\mathrm{bg}}(N^i_{\mathrm{hits}})$ are the probabilities of measuring N^i_{hits} hits for signal and background respectively. The test statistic is defined as:

$$\mathcal{Q} = \log \mathcal{L}^{\max}_{\mathrm{s+b}} - \log \mathcal{L}_{\mathrm{b}}, \tag{7.5}$$

where $\log \mathcal{L}^{\max}_{\mathrm{s+b}}$ is the maximum value of the likelihood obtained by fitting the three free parameters $(\mu_{\mathrm{s}}, \alpha_{\mathrm{s}}, \delta_{\mathrm{s}})$, and $\log \mathcal{L}_{\mathrm{b}}$ is the likelihood computed for the background only case $(\mu_{\mathrm{s}} = 0)$. In the candidate list search, the source coordinates are fixed and the only free parameter is the mean number of signal events. In order to avoid negative values of μ_{s}, a lower limit $\mu_{\mathrm{s}} \geq 10^{-3}$ is imposed in the fit.

7.3. Ingredients for the likelihood

We now describe all the "ingredients" needed to compute the likelihood of the data, i.e. all the PDFs and parametrisations included in Equation 7.4.

7.3.1. Background rate

The number of selected events, $dN(\delta)/d\sin(\delta)$, as a function of the sine of the declination is shown in Figure 7.1. The PDF $\mathcal{B} = dN(\delta)/d\Omega$ used in the likelihood is related to this quantity via:

$$\frac{dN(\delta)}{d\Omega} = \frac{1}{2\pi} \frac{dN(\delta)}{d\sin(\delta)}. \tag{7.6}$$

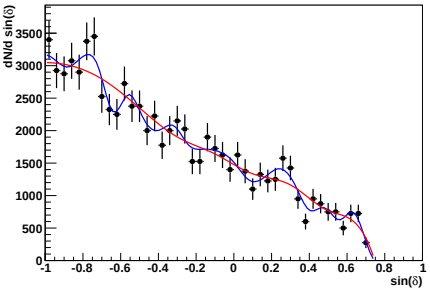

Figure 7.1.: Distribution of the sine of the declination for the selected events. The blue line shows the parametrisation used in the likelihood. The red line shows a second parametrisation used to assign the systematic uncertainty on the background rate (see Section 7.5.1).

As can be seen in Figure 7.2, the number of background events does not depend on the right ascension. This is a consequence of the large exposure and the Earth's rotation.

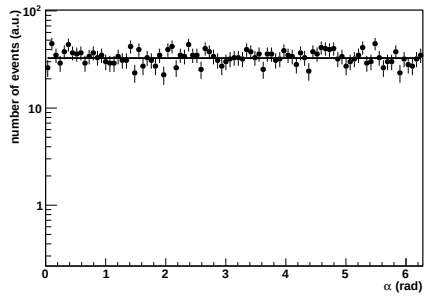

Figure 7.2.: Distribution of the right ascension of the selected events. The data can be fitted to a constant. The resulting χ^2/N_{dof} is 82.5/90.

7.3.2. Point spread function

The PSF is the probability to reconstruct an event at a distance α_{rec} from the source. Figure 7.3 (left) shows the simulated distribution $\mathcal{F} = dP(d\log(\alpha_{\mathrm{rec}}))/d\Omega$ for E_ν^{-2} neutrinos. A parametrisation was chosen to be constant for very small values of α_{rec} since all the directions that are very close to the true position of the source should have the same probability to occur.

In analogy with optical astronomy, the PSF can also be expressed in terms of the angular distances in the zenith and azimuth directions to show its spherically symmetry. This is shown in Figure 7.3 (right)

Angular resolution

The PSF describes the detector response in terms of its pointing accuracy which can be quantified by the angular resolution. The cumulative distribution of the reconstruction angle α_{rec} is shown in Figure 7.4 (left). The median of this distribution is 0.46 ± 0.10 degrees where the uncertainty was assigned following the study presented in Section 5.1. Of the selected events, roughly 83% are reconstructed better than 1 degree. If we consider

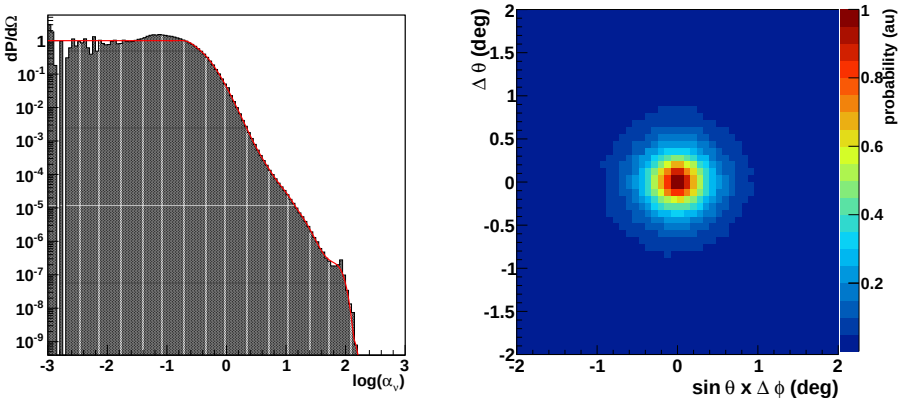

Figure 7.3.: Left: Distribution of the point spread function as a function of the reconstruction angle, α_{rec}, for simulated E^{-2} neutrinos. The red line shows the parametrisation used in the likelihood fit. Right: PSF in terms of $\delta\theta$, the difference in the zenith angle between the true neutrino direction and the reconstructed muon direction, and the angular distance on the azimuth direction. In both plots all the final cuts of the analysis are applied.

only the 12 lines period, then the angular resolution improves to 0.43 ± 0.10 degrees. Figure 7.4 (right) shows the median of the angle α_{rec} as a function of the neutrino energy.

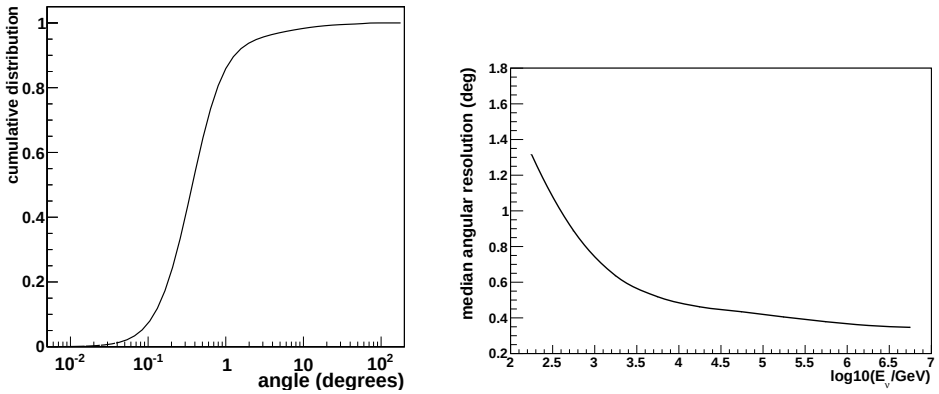

Figure 7.4.: Left: cumulative distribution of the angle between the true neutrino direction and the reconstructed muon track. A neutrino spectrum proportional to E_ν^{-2} is assumed. Right: median of this angle as a function of the neutrino energy. In both plots all the final cuts of the analysis are applied.

7.3.3. Number of hits

Astrophysical neutrinos could have a much harder spectrum compared to atmospheric neutrinos which follow an $E_\nu^{-3.7}$ spectrum in the TeV energy range[1].

Figure 7.5 (bottom) shows the correlation between the number of hits and the neutrino energy. The distribution of the number of hits is shown in Figure 7.5 (top) for data, simulated background and simulated signal. The difference in the energy spectra between signal and background translates to a different $N_{\rm hits}$ distribution.

The number of hits is used in the likelihood as energy estimator to discriminate between signal and background by exploiting the difference in the energy spectrum. Each event is "weighted" with a PDF which describes its probability to be reconstructed with a certain amount of hits. In Section 7.6 we will quantify the improvement in terms of discovery potential obtained by including the $N_{\rm hits}$ information in the likelihood.

7.3.4. Acceptance

The effective area of the detector has been defined in Chapter 1 as the ratio between the neutrino event rate and the cosmic neutrino flux. A closely related parameter is the acceptance for a given neutrino flux, defined as the constant of proportionality between the flux normalisation, k_ν, and the expected number of events. Unless otherwise stated, the relation between a neutrino flux $dN/dE_\nu dt$ and the flux normalisation k_ν is given by:

$$\frac{dN}{dE_\nu dt} = k_\nu \left(\frac{E_\nu}{\rm GeV}\right)^{-2} {\rm GeV}^{-1}\,{\rm cm}^{-2}\,{\rm s}^{-1}. \tag{7.7}$$

The acceptance can be expressed in terms of the effective area as:

$$A(\delta_\nu) = k_\nu^{-1} \int\int dt dE_\nu A_\nu^{\rm eff}(E_\nu, \delta_\nu, t) \frac{dN_\nu}{dE_\nu dt}. \tag{7.8}$$

The acceptance of this analysis for a neutrino spectrum proportional to E_ν^{-2} is shown in Figure 7.6 as a function of the sine of the declination. For a source at declination $\delta = -90(0)^\circ$, $A_\nu = 8.8(4.8) \times 10^7\ {\rm GeV}^{-1}\ {\rm cm}^2\ {\rm s}^{-1}$ which means that a total of of 8.8(4.8) neutrino candidates would be detected from a point-like source at $\delta = -90(0)^\circ$ emitting a flux of $10^{-7} \times (E_\nu/{\rm GeV})^{-2}\ {\rm GeV}^{-1}\ {\rm cm}^{-2}\ {\rm s}^{-1}$.

The acceptance is not used in the likelihood computation (nor in the pseudo-experiment generation) but it is needed to compute the sensitivity and limits on the flux.

7.4. Limit setting

When setting an upper limit, an important aspect is the treatment of the test statistic for the background only case. For most regions in the sky, we will observe that no excess is present in the data and therefore an upper limit has to be computed. For this case, the

[1] Prompt atmospheric neutrinos are expected to follow the primary cosmic ray energy spectrum, approximately $E_\nu^{-2.7}$ at TeV energies.

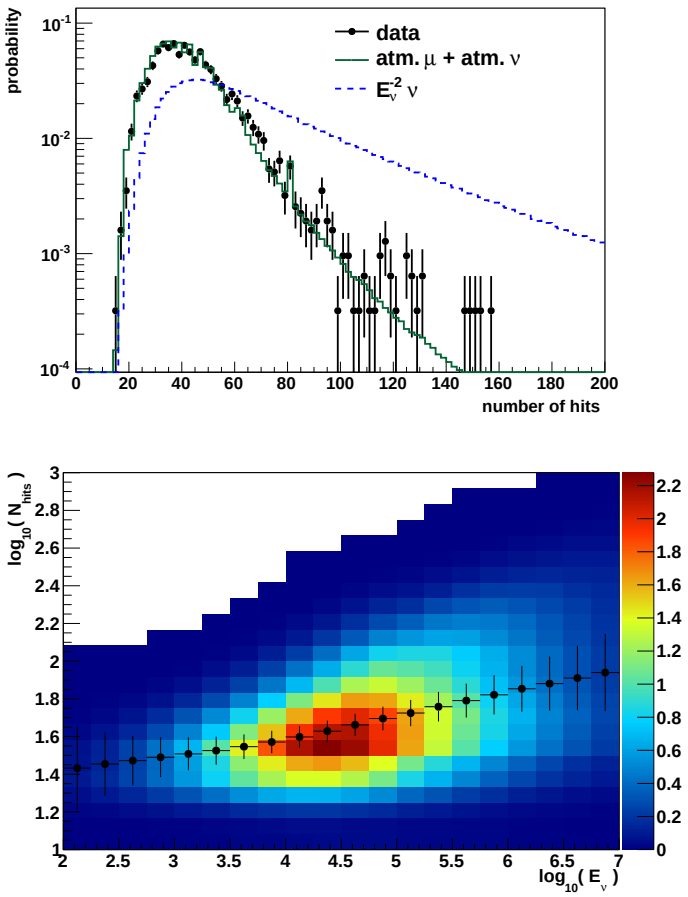

Figure 7.5.: Top: N_{hits} distribution for data (black dots), simulated background (solid green line) and simulated E_ν^{-2} signal events (dashed blue line). Bottom: N_{hits} vs E_ν for simulated signal events with a spectrum proportional to E_ν^{-2}. The distribution of the mean number of hits is superimposed.

value of test statistic could be very close to zero. Figure 7.7 illustrates this situation: the filled yellow histogram depicts the test statistic distribution for the background only case. Two values, A and B, are shown. There are two ways to treat these cases. We could say that the value A of the test statistic is more signal-like than B and so the experiment which gives B as result should have a more stringent limit. On the other hand, we could just say that since A and B are both compatible with the background and the difference is due to background fluctuations, we should set the same limit. A downward fluctuation of the background could result in a exclusion so strong that even zero signal is excluded at the chosen confidence level.

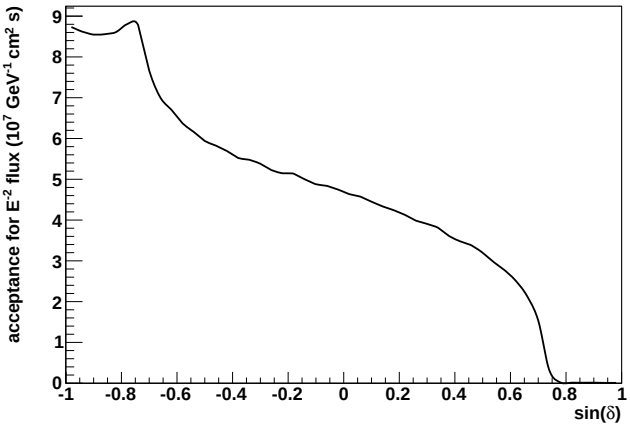

Figure 7.6.: Acceptance of the detector assuming a flux of as a function of the sine of the declination. All the final cuts of the anlysis are applied.

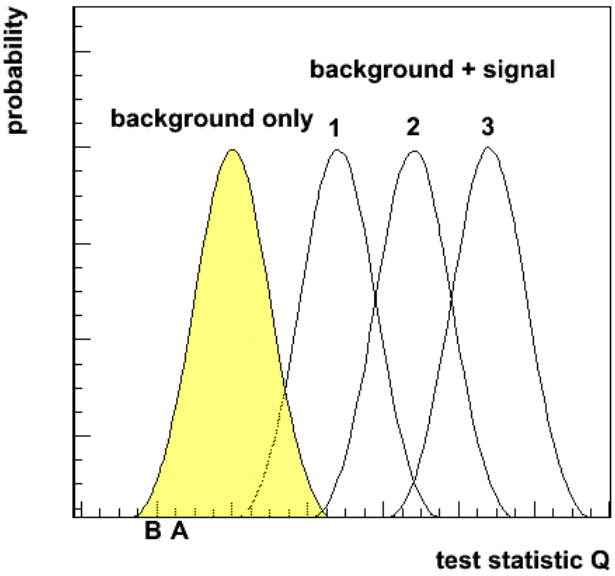

Figure 7.7.: Illustration of the test statistic distribution for two background-like experiments, A and B. See text.

To deal with this problem we adopt the Feldman-Cousins (FC) prescription [153] as procedure to set limits. The FC method prevents the exclusion of zero signal by providing exact coverage. The FC method was proposed in 1997 to solve the problem of non-physical limits. It is a classical confidence belt constructor with a new element based on a likelihood ratio ordering principle. For this analysis the ratio is given by:

$$R = \frac{P(\mathcal{Q}_{\rm obs}|\mu_{\rm s})}{P(\mathcal{Q}_{\rm obs}|\mu_{\rm s}^{\rm best})}, \tag{7.9}$$

where $P(\mathcal{Q}|\mu_{\rm s}^{\rm best})$ is the probability associated with the best estimate of $\mu_{\rm s}$.

To exploit the small variations in $\mathcal{Q}$ for the background only regime, we transform the test statistic in another function which preserves the ordering. Thus, we first define

$$\mathcal{Q}_1 = \log_{10}(\mathcal{Q} + 1.5 \times 10^3). \tag{7.10}$$

The distribution of $\mathcal{Q}_1$ is shown in Figure 7.8 (left). A second transformation $\mathcal{Q}_2(\mathcal{Q}_1)$ was done in order to make the calculation of the FC limits more stable. This function was explicitly constructed in order to have a reasonable number of entries in each bin for both the background and the signal regions. In particular, the function was chosen so that $\mathcal{Q}_2(\mu_{\rm s} = 0) + \mathcal{Q}_2(\mu_{\rm s} = 10)$ is a flat distribution between 0 and 1. Figure 7.8 (right) shows the distribution of $\mathcal{Q}_2$. Following the likelihood ratio ordering principle, a confidence belt is constructed. This is shown in Figure 7.9 as a function of the transformed test statistic $\mathcal{Q}_2$.

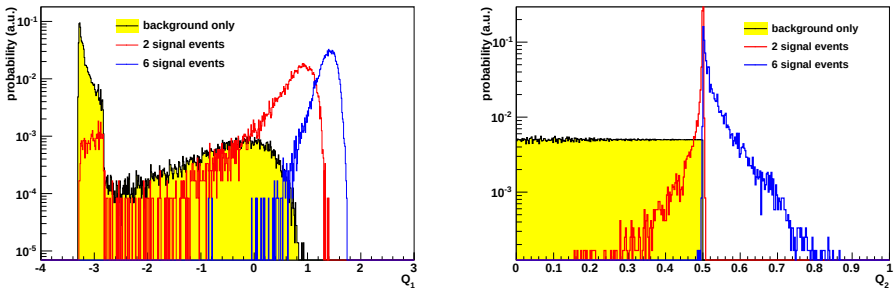

Figure 7.8.: Distribution of the variables $\mathcal{Q}_1$ (left) and $\mathcal{Q}_2$ (right) for background only experiments (yellow histogram) and for the cases where we simulate two (red histogram) and six signal events (blue histogram) at a declination $\delta = -70°$.

7.5. Pseudo-experiment generation

The limits and the sensitivity of the analysis are evaluated by generating pseudo-experiments (PE). The background and the signal are simulated at this stage. In each PE the number of background events are randomly generated by sampling the declination from the spline

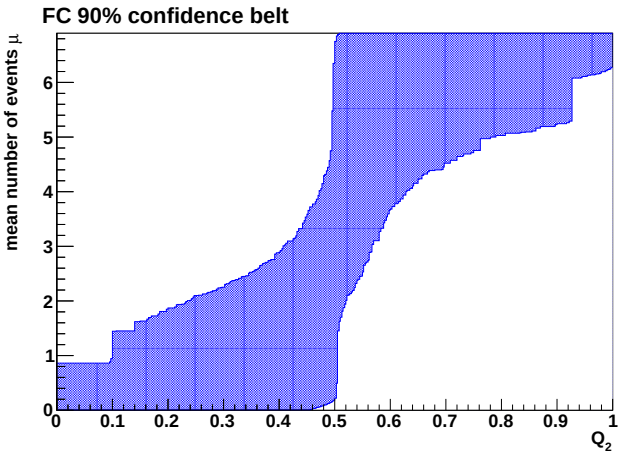

Figure 7.9.: Confidence belt obtained with the Feldman-Cousins prescription for the declination $\delta = -70°$. On the x-axis the transformed test statistic, $\mathcal{Q}_2$, is shown. The y-axis the mean number of signal events μ_s.

parametrisation $\mathcal{B}$ 7.6. The right ascension is sampled from an uniform distribution. For a given source declination, signal events (up to 20) are added by sampling $N_{\mathrm{hits,i}}$ and $\alpha_{\mathrm{rec,i}}$, from a 2-D declination distribution (see Figure 7.10).

At this stage, the systematic uncertainties on the background rate, the angular resolution, the absolute orientation and the number of hits of the detector are included.

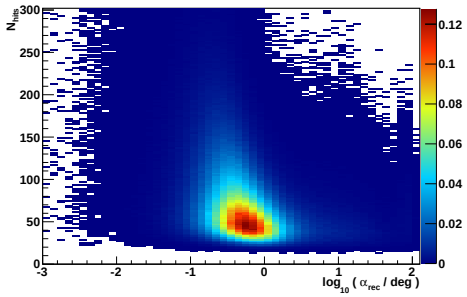

Figure 7.10.: Distribution of the number of hits, $N_{\mathrm{hits,i}}$, and the reconstruction angle, $\alpha_{\mathrm{rec,i}}$,. This distribution is used to sample the angular distance and the number of hits of an event to the source location to simulate the signal events.

7.5.1. Inclusion of systematic errors

The systematic uncertanties described in Section 5 are included generating the PE; with the exception of the systematic errors on the acceptance which are added while computing the sensitivity and the limits on the neutrino flux. The impact of these errors is also evaluated in terms of discovery potentials and sensitivities (see Section 7.5.3)

Angular resolution

The uncertainty on the angular resolution (15%) is taken into account by multiplying for each PE, the generated angular distance $\alpha_{\rm rec}$ by a scale factor, which is drawn from a Gaussian distribution with mean 1 and width equal to the $\sigma = 0.15$. The effect of including this systematic on the discovery potential is shown in Figure 7.11 for the full-sky search. A 15% uncertainty on the angular resolution has a small (less than 5%) effect. For comparison, Figure 7.11 also shows the discovery potential for PEs with a 30% systematic error on the angular resolution.

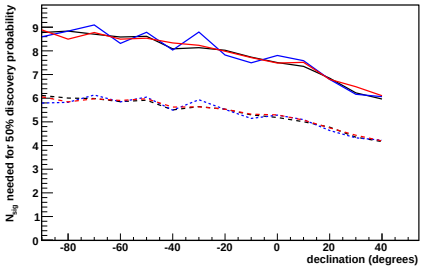

Figure 7.11.: Number of events needed for 50% probability to claim a 3σ (dashed lines) and 5σ (solid lines) discovery for experiments with 0 (red lines), 15% (black lines) and 30% (blue lines) systematic uncertainty on the angular resolution. In this last scenario statistical fluctuations are visible.

The worsening of the 3σ and 5σ discovery probabilities with a degraded angular resolution was also estimated. In this case, for a source at declination $\delta = -70^{\circ}$, the mean number of signal events needed for a 3σ and 5σ discovery assuming an angular resolution degraded by a factor 2 is roughly a factor 1.4 higher compared to that with the default angular resolution. This is shown in Figure 7.12

Absolute orientation

The uncertainty in the absolute orientation of the detector is included in a way similar to the systematic errors in the angular resolution. For each PE, the zenith and azimuth angles of all generated signal events are shifted by two random variables each drawn from a Gaussian distribution with mean 1 and width equal to the uncertainty on that variable. A negligible worsening of the discovery potential due to this systematic uncertainty has been observed.

Background rate

The background rate plotted in Figure 7.1 presents peaks and bumps which could be due to statistics or a variation in the acceptance of the detector. In order to take into account this possible effect, an alternative parametrisation, $\mathcal{S}(\delta)$, is used. This is also shown in

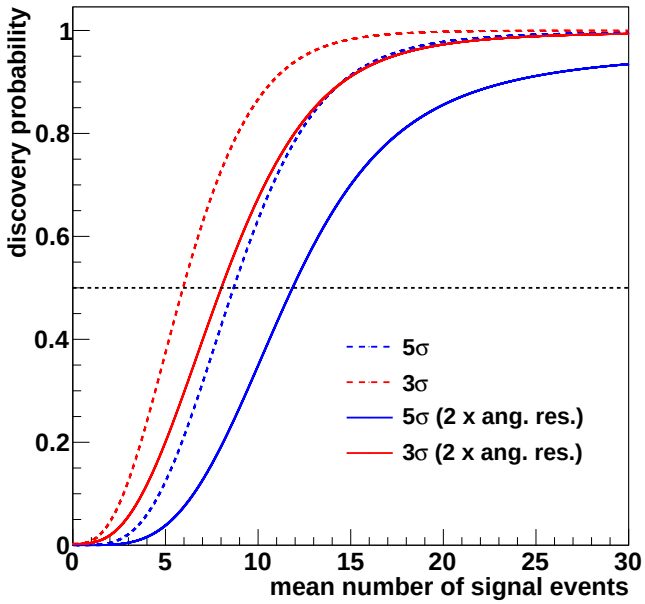

Figure 7.12.: Probability for a 3σ (red lines) and 5σ (blue lines) full-sky search discovery as a function of the mean number of signal events from a source at $\delta = -70°$. The solid lines shows the case where the angular resolution has been degraded by a factor 2.

Figure 7.1 (red line). In each PE, the background model used for generation is

$$\mathcal{B}_{\mathrm{PE}}(\delta) = \mathcal{B}(\delta) + r \times (\mathcal{S}(\delta) - \mathcal{B}(\delta)), \tag{7.11}$$

where r is a random number normally distributed. The contribution of including this systematic uncertainty was found to be less than 5% in the limits on the neutrino flux.

Number of hits

A 10% systematic uncertainty on the number of hits is included in each PE by multiplying the value of N_{hits} for all events with a random number drawn from a Gaussian with mean 1 and width equal to 0.10. The impact of this systematic error in terms of the sensitivity and limits on the neutrino flux was found to be negligible.

Acceptance

The 15% systematic uncertainty on the acceptance is included when computing the sensitivity of the analysis and (in the absence of discovery) the limits on the neutrino flux. A systematic uncertainty on the acceptance entails a reduction or increase of the number of

detected events hence on the mean number of signal events, $\mu_{\rm s}$. Assuming that the actual number of signal events, $N_{\rm s}$, is distributed according to a Poisson distribution with mean $\mu_{\rm s}$, the distribution of the test statistic $\mathcal{Q}$ can be expressed as:

$$\frac{dP(\mu_{\rm s})}{d\mathcal{Q}} = \sum_{N_{\rm s}=0}^{\infty} \frac{dP(N_{\rm s})}{d\mathcal{Q}} \frac{\mu_{\rm s}^{N_{\rm s}} e^{-\mu_{\rm s}}}{N_{\rm s}!} \equiv \sum_{N_{\rm s}=0}^{\infty} \frac{dP(N_{\rm s})}{d\mathcal{Q}} \mathcal{P}(N_{\rm s}|\mu_{\rm s}), \tag{7.12}$$

where in practice the summation goes to the maximum number of signal events simulated (20). The mean number of signal events is unknown hence we can only derive an estimate of it, $\hat{\mu}_{\rm s}$ with uncertainty $\sigma_{\mu_{\rm s}}$. Assuming that the probability for $\mu_{\rm s}$ is described by a Gaussian, $\mathcal{G}$, Equation 7.12 becomes:

$$\frac{dP(\mu_{\rm s})}{d\mathcal{Q}} = \sum_{N_{\rm s}=0}^{\infty} \frac{dP(N_{\rm s})}{d\mathcal{Q}} \int \mathcal{P}(N_{\rm s}|\mu_{\rm s}) \mathcal{G}(\mu_{\rm s}|\hat{\mu}_{\rm s}, \sigma_{\mu_{\rm s}}) d\mu_{\rm s}. \tag{7.13}$$

Equation 7.13 is then used in the limit setting code when constructing the FC confidence belts to include the systematic on the acceptance.

Figure 7.13 shows the effect of including the 15% uncertainty on the acceptance for the sensitivity. A small variation ($< 5\%$) is observed. For comparison, Figure 7.13 also shows the case where this systematic value is increased to 50%.

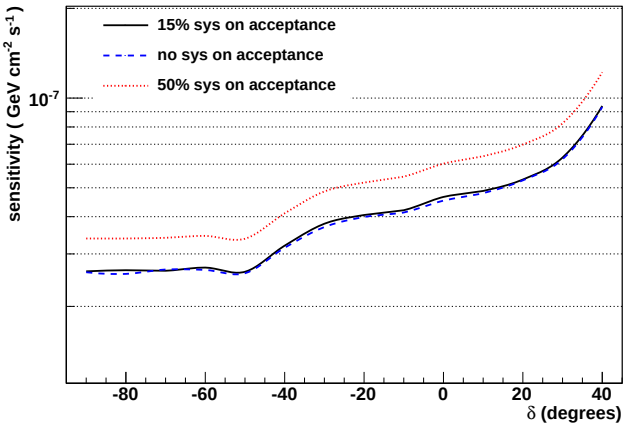

Figure 7.13.: The effect of the systematic uncertainty on the acceptance. The solid black line reports the sensitivity of the analysis with the chosen 15% value of the systematic on the acceptance. The dashed blue line shows the case where no systematic uncertainty on the acceptance is included. Finally, the dotted red line shows the extreme case where a 50% uncertainty on the acceptance is added.

7.5.2. Full sky search

The full-sky search looks for an excess of signal events anywhere in the sky. As a first step, a clustering algorithm identifies potentially significant clusters of at least four events within a cone of three degrees diameter. The use of a larger diameter or a larger/lower minimum number of events does not significantly improve the sensitivity.

For each selected cluster, the likelihood maximisation estimates the source location and the mean number of signal events. The presence of cosmic neutrinos in the data is then tested with only the cluster with the highest value of the test statistic.

Test statistic

The distribution of the highest test statistic for the full-sky search obtained from pseudo-experiments (see 7.5) is shown in Figure 7.14 (left) for the background only case and for experiments where several signal events where added to the background at a declination of $\delta = -70^\circ$. A discovery is claimed when the observed test statistic exceeds a critical

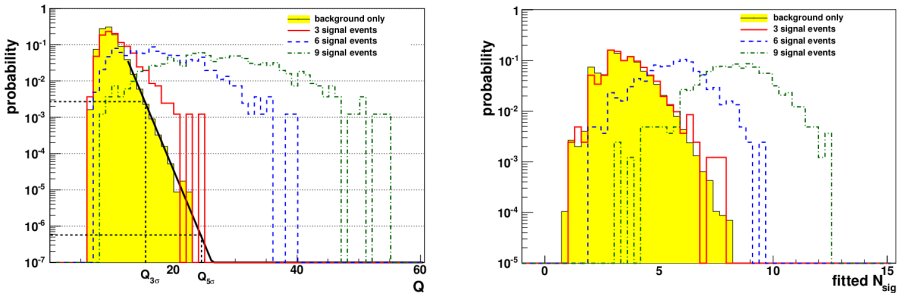

Figure 7.14.: Left: distribution of the test statistic for a full-sky search for the background only hypothesis (filled yellow histogram) and for experiments where we simulated 3, 6 and 9 signal events at a declination of $\delta = -70^\circ$ (solid red line, dashed blue line and dotted-dashed green line respectively). The vertical dashed lines show the values of $\mathcal{Q}$ corresponding to the 3σ and 5σ discovery. Right: distribution of the fitted number of signal events for the same experiments.

value determined from the distribution of $\mathcal{Q}$ for the background only hypothesis from an *a priori* confidence level such as

$$1 - \mathrm{CL} \equiv \mathrm{P}(\mathcal{Q} > \mathcal{Q}_{\mathrm{crit}} | \mathrm{H}_0). \tag{7.14}$$

Common values for the confidence level are 1-2.7 $\times 10^{-3}$ and 1-5.7 $\times 10^{-7}$ also known as 3σ and 5σ CLs respectively. The critical values $\mathcal{Q}_{3\sigma}$ and $\mathcal{Q}_{5\sigma}$ are indicated in Figure 7.14 (left) and are respectively 15.5 and 24.5. To estimate the critical value for a 5σ discovery an exponential function was fitted to the 5% tail of the distribution. The distribution of the test statistic when three signal events are added is similar to the background-only one. This can be explained by the presence of background clusters with a higher test statistic than true signal clusters.

The fitted number of signal events is shown in Figure 7.14 (right) for the same experiments considered for the $\mathcal{Q}$ distribution. For 3, 6, 9 signal events simulated the fit returns on average 3.5, 5.6 and 8.4 events respectively. This small underestimation is mainly due to the reduced size of the pre-clustering cone. Events that are more than 3 degrees away from the source are excluded from the fit (of N_{sig}).

Discovery potential

The probability to make a discovery at the 3σ and 5σ significance level is shown in Figure 7.15 as a function of the mean number of signal events , μ_{s}, for a source at declination $\delta = -70^{\circ}$. The number of events needed to claim a 3σ and 5σ discovery in 50% of the PEs is 5.8 and 8.6 respectively. These quantities are shown in Figure 7.16 (top) for all the visible declinations. From the mean number of signal events needed for a discovery, we can immediately derive the required neutrino flux by means of the acceptance (see Section 7.5.1. This is shown in Figure 7.16 (bottom). At a declination $\delta = -70^{\circ}$, a neutrino flux of roughly 6.98(10) $\times 10^{-8}$ GeV^{-1} cm^{-2} s^{-1} would be needed for a 50% discovery probability at 3(5)σ significance level.

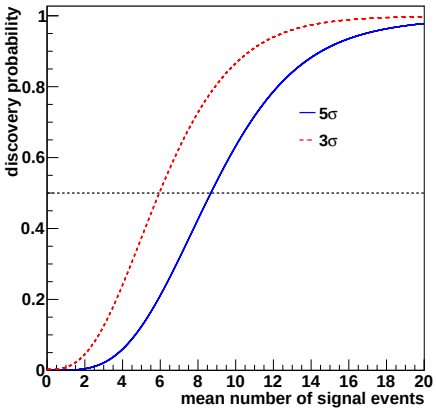

Figure 7.15.: Probability for a 3σ (dashed red line) and 5σ (solid blue line) discovery as a function of the mean number of signal events from a source at declination $\delta = -70^{\circ}$ with a neutrino flux proportional to E_{ν}^{-2}. The horizontal dotted black line corresponds to the probability to make a discovery in 50% of the PEs.

7.5.3. Candidate list search

The candidate list search looks for an excess of signal events at a number of pre-defined locations in the sky. For this search, all events within 20 degrees of the source location are selected for the fit. The likelihood is then maximised by numerically fitting the source intensity, μ_{s}, with the source coordinates fixed.

Test statistic

The distribution of the test statistic for the fixed search is shown in Figure 7.17 (left). For many experiments, no events are in the neighborhood of the source location resulting in

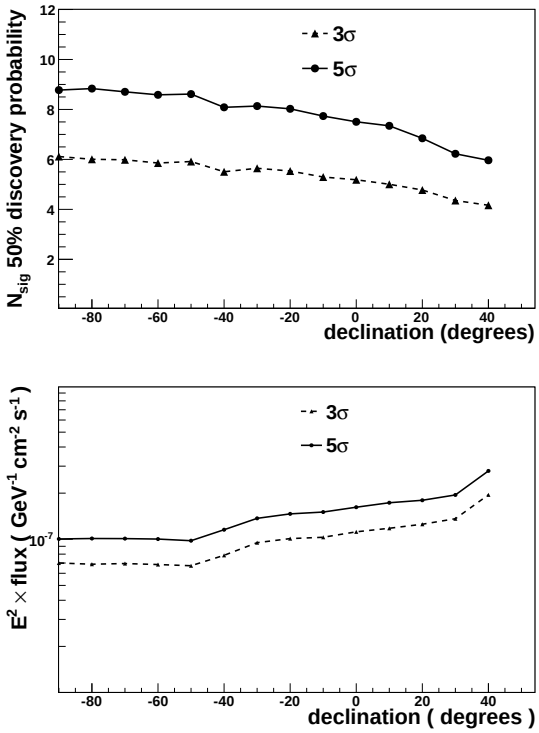

Figure 7.16.: Top: number of events needed for 50% probability to claim a 3σ (dashed line) and 5σ (solid line) discovery as a function of the source declination. Bottom: the number of events is now translated into the required neutrino flux.

a visible peak at $\mathcal{Q} = 0$. The critical values of the test statistic $\mathcal{Q}_{3\sigma} = 3.6$ and $\mathcal{Q}_{5\sigma} = 10$ are also indicated. As for the full-sky search, the tail of the distribution was fitted by an exponential function in order to extrapolate the value of $\mathcal{Q}_{5\sigma}$.

Figure 7.17 (right) shows the distribution of the fitted number of signal events. In this case the mean of the histograms with 3,6 and 9 signal events simulated is 2.8, 5.8 and 8.7 respectively.

Sensitivity

In case no signal is detected, upper limits can be computed. In particular, if a value of the test statistic, $\mathcal{Q}_{\rm obs}$, is obtained we can derive the upper limit on the mean number of signal events from the FC confidence belt. It is common in neutrino astronomy to present 90%CL upper limits together with the sensitivity of the analysis, i.e. the median of these upper limits obtained by choosing $\mathcal{Q}_{\rm obs}$ as the median of the distribution of the test statistic for the background only hypothesis. The median number of signal events that can be excluded at 90% CL is shown in Figure 7.18 (top). Figure 7.18 (bottom) shows

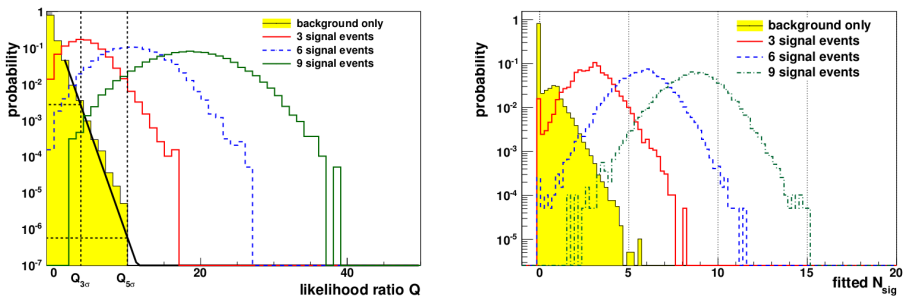

Figure 7.17.: Left: distribution of the test statistic for a fixed sky search for the background only hypothesis (filled yellow histogram) and for experiments where we simulated 3, 6 and 9 signal events at a declination of $\delta = -70^\circ$ (solid red line, dashed blue line and dotted-dashed green line respectively). The vertical dashed lines show the values of $\mathcal{Q}$ corresponding to the 3σ and 5σ discovery. Right: distribution of the fitted number of signal events for the same experiments.

the same in terms of the neutrino flux.

So far we have assumed a neutrino spectrum proportional to E_ν^{-2} which extendes over all energies. Nevertheless, the detector is primarily sensitive in the TeV range. The sensitivity of the analysis for different neutrino energy ranges is shown in Figure 7.19. In particular at the lowest declination ($\delta < -50^\circ$) the major contribution to the sensitivity comes from events in the range 1 TeV $< E_\nu <$ 100 TeV, while at positive declination the contribution of events with higher energies (30 TeV $< E_\nu <$ 3 PeV) is more important.

Candidate source list

In the fixed search, we considered in particular 51 pre-defined candidate sources. The selection of these sources was done considering their gamma-ray flux and their visibility as criteria [152]. Among the Galactic sources only TeV emitters were selected. No such requirement was adopted for the extragalactic sources since TeV gamma-rays may be absorbed by the Extragalactic Background Light [155, 156, 157]. Table 8.2 lists the selected sources.

In order to further test our algorithm, we have simulated signal events for a source at an arbitrary location ($\delta = -7^\circ$) and ran pseudo-experiments as in the fixed search for each of the 51 candidate sources considered. The results are shown in Figure 7.20 in terms of the discovery potential (right). The values of the mean number of signal events obtained for the 3σ and 5σ probabilities are 3.2 and 5.4 respectively. These numbers can be compared with the equivalent ones obtained for the full-sky search where 5.2 and 7.6 signal events where needed in 50% of the experiments to claim a discovery at a declination of $\delta = -7^\circ$. The flux required to claim a discovery is thus reduced by roughly 40% by restricting the search to 51 candidates instead of looking everywhere in the visible sky.

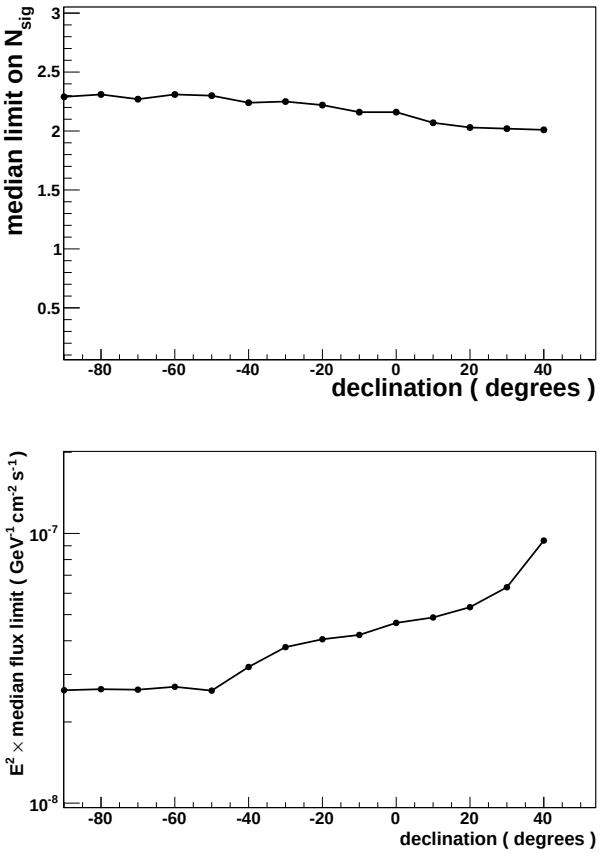

Figure 7.18.: Top: median upper limit that can be set on the mean number of signal events from an E_ν^{-2} neutrino point source as a function of the declination. Bottom: median upper limit that can be set on the neutrino flux as a function of the declination.

7.6. Improvement with $N_{\rm hits}$

We already mentioned how the number of hits are used in the likelihood to discriminate between signal and background. The idea is to consider the number of hits as a measure of the neutrino energy. Figure 7.21 shows the discovery potential at 3σ and 5σ significance level as a function of the mean number of signal events for a full-sky search. The same curves are plotted for experiments where the $N_{\rm hits}$ information was not included in the likelihood. The use of $N_{\rm hits}$ in the likelihood reduces by $\sim 25\%$ the number of events (thus the neutrino flux) needed for a discovery.

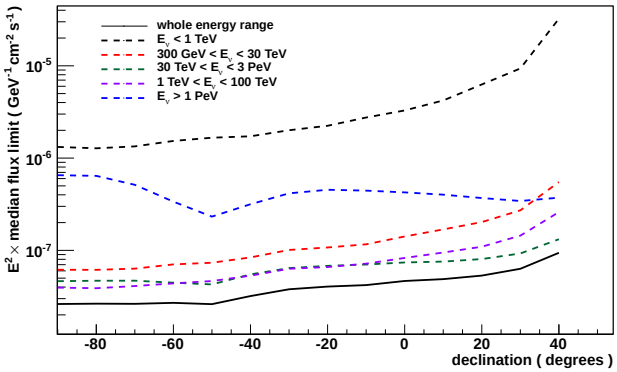

Figure 7.19.: Median sensitivity for different bands of neutrino energy as a function of the declination.

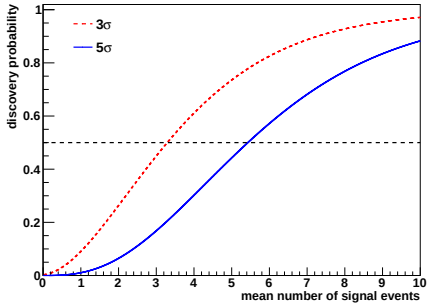

Figure 7.20.: Probability for a 3σ (dashed red line) and 5σ (solid blue line) discovery as a function of the mean number of signal events assuming a neutrino flux proportional to E_ν^{-2} emitted by a source at declination $\delta = -70°$.

7.7. Extended sources and energy cut-off

So far we have discussed point-like sources, however we also want to use the likelihood ratio method for sources that are spatially extended. In order to include the source morphology we need to modify $\mathcal{F}(\alpha_{\mathrm{rec,i}}(\alpha_\mathrm{s}, \delta_\mathrm{s}))$, the PSF of the signal, in the likelihood. In particular, we convolve the point spread function with the source distribution. Figure 7.22 shows this for the case of RX J1713.7-3946 (source extension: $\sigma_\alpha = 0.65°$, $\sigma_\delta = 0.65°$) and Vela X (source extension: $\sigma_\alpha = 0.48°$, $\sigma_\delta = 0.36°$). where the source distribution corresponds to the gamma-ray map. Hence, in the likelihood the pdf of the signal has been replaced by a term:

$$\mathcal{F}(\alpha_{\mathrm{rec,i}}(\alpha_\mathrm{s}, \delta_\mathrm{s})) \longrightarrow \int\int \mathcal{F}(\alpha_{\mathrm{rec,i}}(\alpha_\mathrm{s}, \delta_\mathrm{s})) \times \mathcal{S}(\sigma_{\alpha_s}, \sigma_{\delta_s}) d\alpha_\mathrm{s} d\delta_\mathrm{s}. \tag{7.15}$$

where the term $\mathcal{S}(\sigma_{\alpha_s}, \sigma_{\delta_s})$ represents the source distribution.

In order to evaluate the improvement of the discovery potential with the extended source hypothesis, we simulated different source distributions with a Gaussian, i.e. we model the

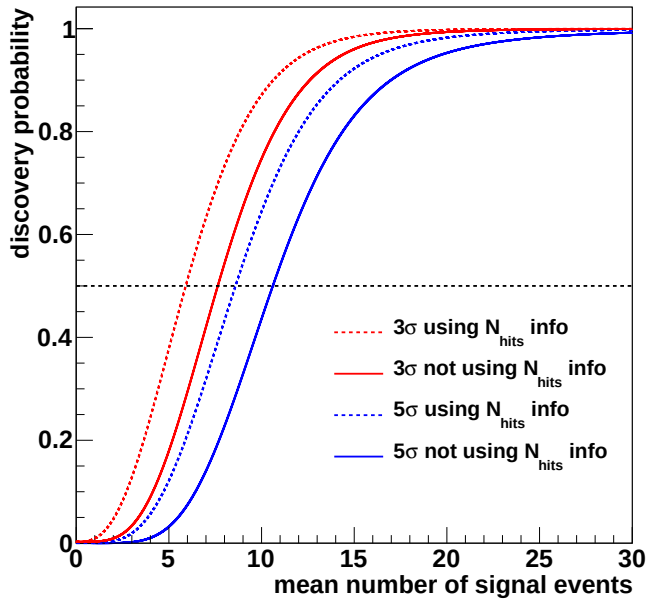

Figure 7.21.: Probability for a 3σ (red lines) and 5σ (blue lines) full-sky search discovery as a function of the mean number of signal events from a source at $\delta = -70^\circ$. The dotted lines are for the likelihood used in the analysis, the solid lines refer to the case where the number of hits information was is not used in the likelihood.

source as a two-dimensional Gaussian with a width equal to the source extension. The results are shown in Figure 7.23. For a source with a Gaussian extension $\sigma = 1^\circ$ at a declination of $\delta = -70^\circ$, the mean number of signal events (and the flux) needed to claim a 5σ discovery is a factor 1.4 higher compared to a point-like source.

We have seen in Chapter 2 how several models describe the neutrino flux from gamma-ray sources with a more complicated spectrum than the standard one proportional to E_ν^{-2}. In particular, cut-offs in the energy spectrum seem to be well supported by gamma-ray observations. For this reason, we have studied the worsening of the discovery probability for a neutrino flux model with an exponential cut-off as

$$\frac{dN}{dE_\nu} = \phi \times \left(\frac{E_\nu}{\mathrm{GeV}}\right)^{-2} e^{-\frac{E_\nu}{E_c}}, \tag{7.16}$$

with E_c the cut-off energy. The results are shown in Figure 7.24 and 7.25. For a source located at $\delta = -70^\circ$, the number of signal events needed for a 5σ discovery assuming a cut-off energy of 1 TeV is roughly a factor 2 higher compared to the hypothesis without an exponential cut-off.

The sensitivity of the analysis for different cut-off energies is shown in Figure 7.26. As

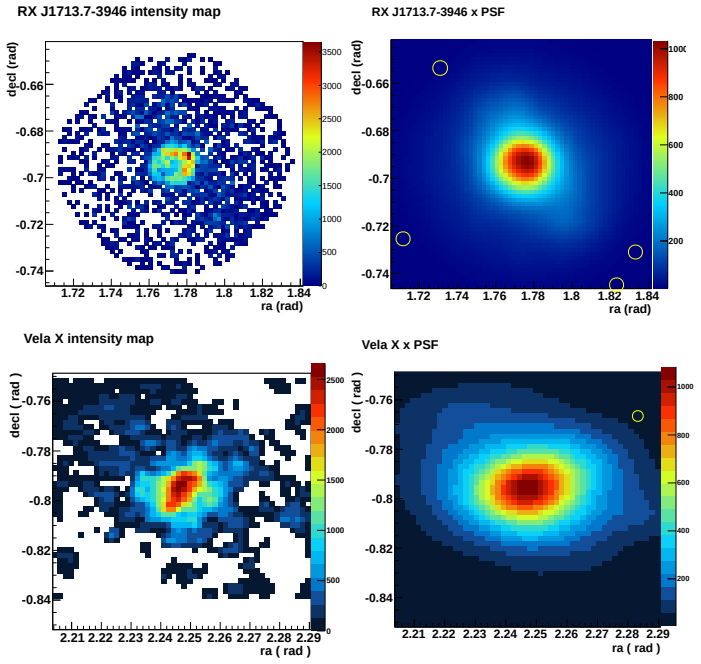

Figure 7.22.: Left: gamma-ray map of RX J1713.7-3946 (top) and Vela X (bottom) showing its extension. Data taken from [158, 159]. Right: detector PSF convoluted with the source distribution. The yellow circles indicate the events closest to the source.

expected, the larger is E_c, the closer the sensitivity is to the default one without any cut-off.

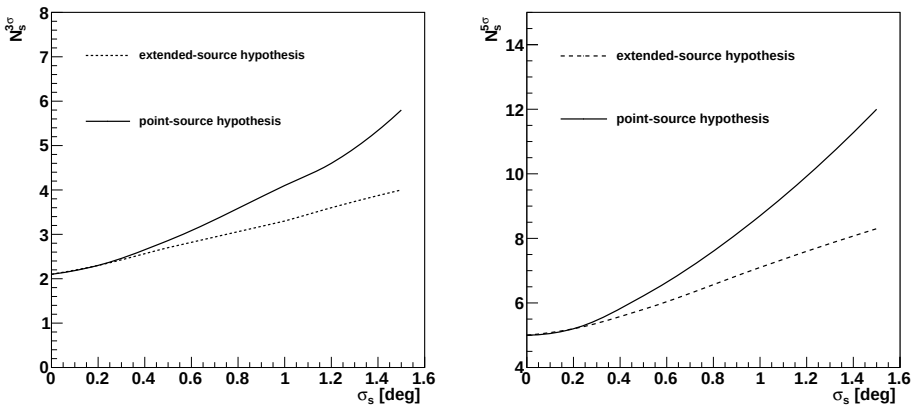

Figure 7.23.: Fixed search discovery potential in terms of the mean number of signal events needed to claim a 3σ (left) and 5σ (right) discovery as a function of the extension of a source distributed as a two-dimensional Gaussian at a declination $\delta = -70°$.

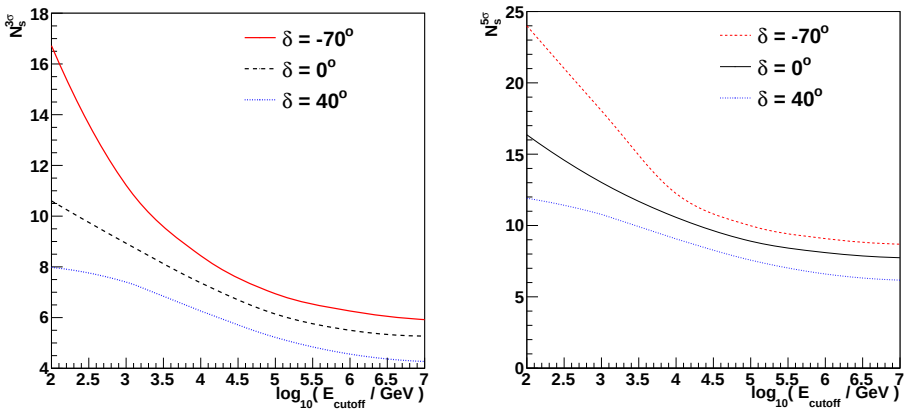

Figure 7.24.: Full-sky discovery potential in terms of the mean number of signal events needed for a 3σ (left) and 5σ discovery as a function of the energy cut-off E_c for three different source declinations.

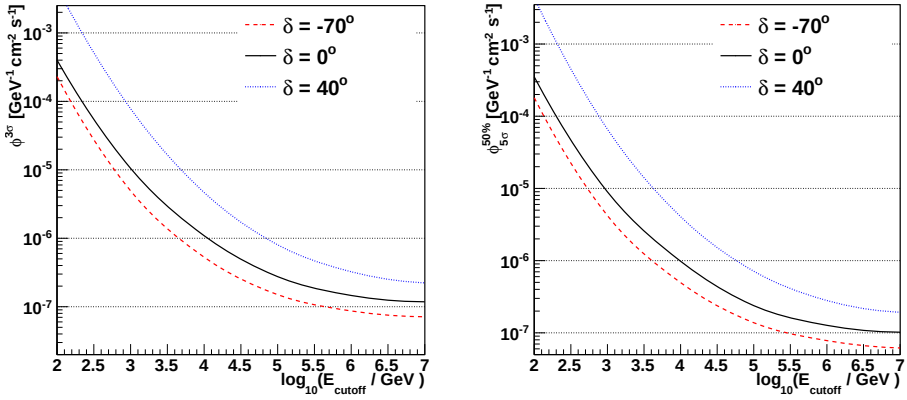

Figure 7.25.: Full-sky discovery potential in terms of the neutrino flux needed for a 3σ (left) and 5σ discovery as a function of the energy cut-off E_c for three different source declinations.

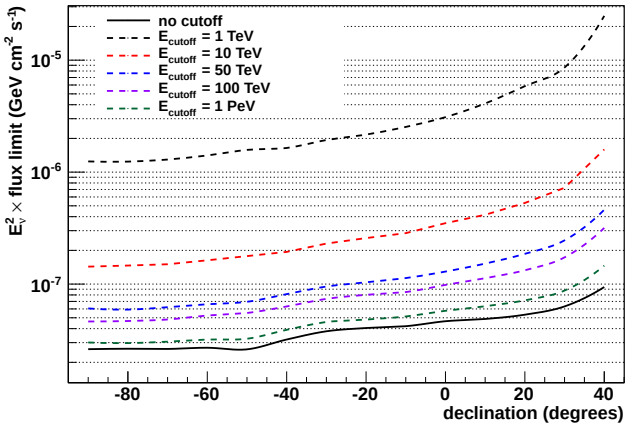

Figure 7.26.: Median sensitivity for different cut-off energies as a function of the declination.

8. Results

The search for truth is in one way hard and in another easy. For it is evident that no one can master it fully nor miss it wholly. But each adds a little to our knowledge of nature and from all the facts assembled these arise a certain grandeur.

Aristoteles

We present here the results of the two searches introduced in Chapter 7. Since no significant deviations from the background are observed, upper limits are derived. Section 8.1 and 8.2 present the results obtained for the full-sky search and the candidate list search respectively. In Section 8.3, upper limits on the neutrino emission models presented in Chapter 2 are reported.

8.1. Full-sky search

In the full-sky search we look for an excess of signal events everywhere in the visible sky. Starting from the 3058 selected events, the pre-clustering algorithm selects a total of 1413 clusters with at least 4 events within a cone of 3 degrees diameter. Figure 8.1 shows a sky map in equatorial coordinates of $\mathcal{Q}(\alpha, \delta)$.

Similarly, Figure 8.2 shows the sky map of pre-trial significances, i.e. the penalty factor due to the fact that we look at many points in the sky is not taken into account.

The most significant deviation from the background (or "hot-spot") is located at $(\alpha, \delta) = (-46.5°, -65.0°)$ where 5(9) events are within 1(3) degrees of this position. The corresponding cluster of events is shown in Figure 8.3. The maximum likelihood fit assigns $\mu_s = 5.1$ and the value of the test statistic is $\mathcal{Q} = 13.1$. The pre-trial p-value is 4.4 $\times 10^{-3}$.

Comparing the observed test statistic with the $\mathcal{Q}$ distribution for the background only hypothesis (see Figure 7.14), yields a post-trial[1] p-value of 2.6% which is equivalent to 2.2σ (adopting the two-sided convention). Therefore the result obtained is compatible with a statistical fluctuation of the background. The equatorial coordinates and other reconstruction parameters for the nine events found in the most signal-like cluster are reported in Table 8.1. Two possible counterparts of the hot-spot were found in the frequency range from radio to X-rays. The closest source is the Active Galactic Nuclei PKS 2047-655

[1] The post-trial p-value is determined as the fraction of pseudo-experiments with at least one cluster with a higher value of the test statistic.

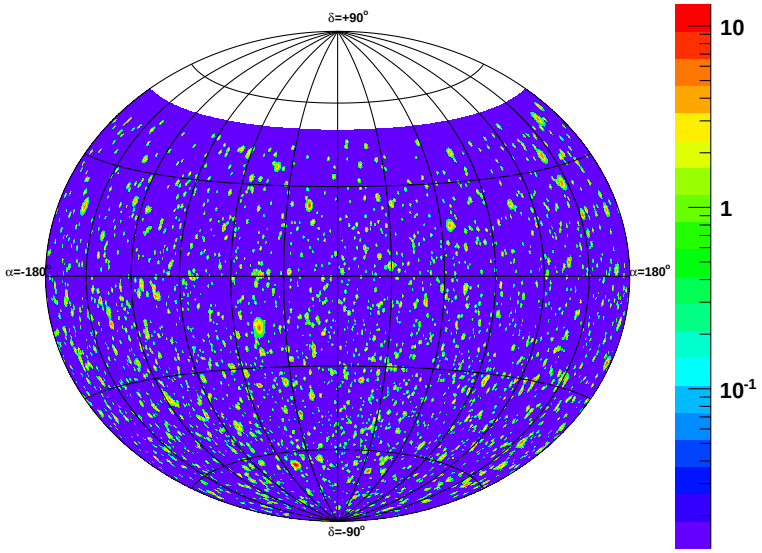

Figure 8.1.: Sky map in equatorial coordinates showing the values of the test statistic obtained for each cluster in the full-sky search.

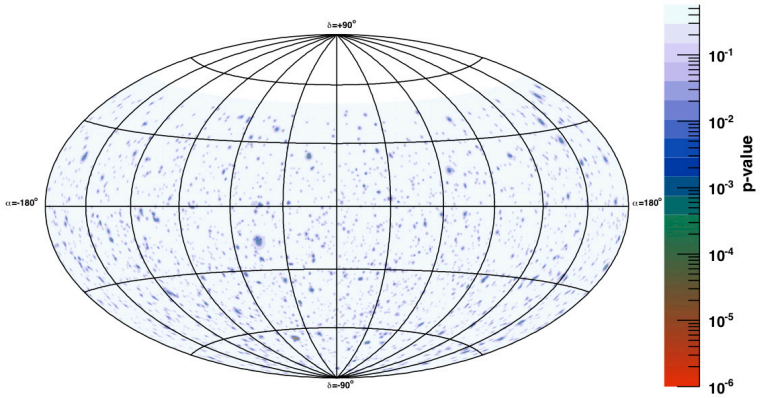

Figure 8.2.: Sky map in equatorial coordinates showing the pre-trial p-values obtained in the full-sky search.

located at a distance of 0.54 degrees from the center of the cluster (redshift $z = 2.3$). The other possible counterpart is the galaxy cluster AC 103 located at redshift $z = 0.31$ at a distance of 0.87 degrees from the center of the cluster.

The second most signal-like cluster is located at $(\alpha, \delta) = (-27..2°, -46.0°)$. In this case 7(3) events are within 1(3) degrees of this position. The value of the test statistic

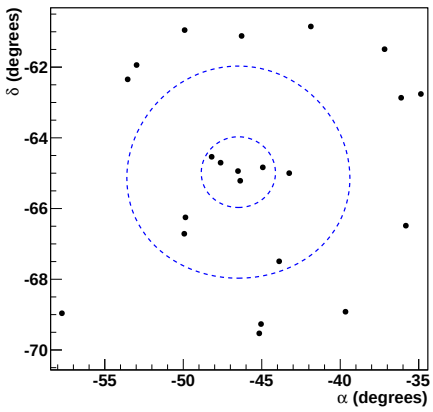

Figure 8.3.: Most signal-like cluster found in the full-sky search with 5(9) events are located within 1(3) degrees of its center.

Run number	α [°]	δ [°]	N_{hits}	Λ	N_{lines}
32168	-46.5	-64.9	56	-4.79	9
43222	-47.2	-64.7	29	-5.06	4
50225	-46.3	-65.2	48	-4.80	8
52092	-44.9	-65.8	125	-4.73	7
53607	-48.2	-64.5	117	-4.68	10
37402	-49.9	-66.7	41	-4.26	5
38431	-49.8	-66.3	34	-5.16	9
43022	-43.9	-67.5	42	-4.99	6
47660	-43.2	-65.0	48	-5.08	9

Table 8.1.: Run number (first column), equatorial coordinates, number of hits used in the reconstruction, value of Λ and number of lines used in the reconstruction (last column) for the nine events of the most signal like cluster in the full-sky search. The line separates the five events which are within 1 degree from the fitted source position.

for this cluster is $\mathcal{Q} = 8.5$ which leads to a post-trial p-value of 0.8.

8.1.1. Multi-wavelength observation of the hot-spot

The ANTARES collaboration have proposed to the H.E.S.S. collaboration to observe the region around $(\alpha, \delta) = (-46.5°, -65.0°)$ in order to search for a possible gamma-ray excess at this location. The H.E.S.S. telescope detects gamma-rays in the 100 GeV - 100 TeV energy range with a field of view of 5 degrees.

A two hour observation was made in November 2012. The data have been taken in so-called "wobble" mode, i.e. the source direction is located with a pointing offset of 0.5°

in declination relative to the center of field of the camera.

The result is shown in Figure 8.4. Unfortunately, no significant excess of gamma-rays was found and an upper limit on the gamma-ray flux was derived [160] and compared with a prediction (red line) obtained by converting the neutrino flux into a flux of gamma-rays. The conversion relies on Monte Carlo simulations and was derived following the assumptions made in [95]. It is likely that the ANTARES excess is due to a background fluctuation.

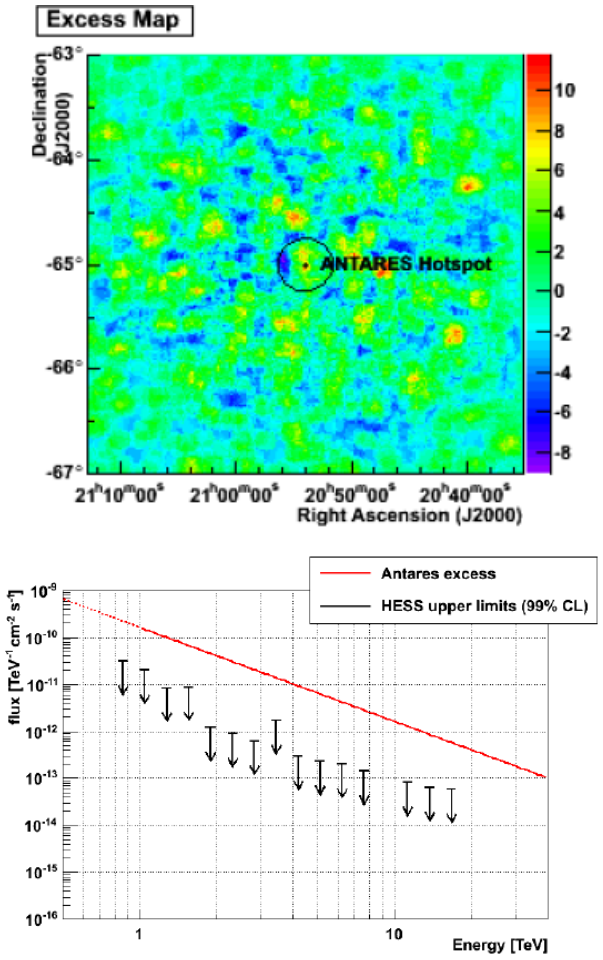

Figure 8.4.: Top: Map of the very high-energy gamma-ray events exceeding the background expectation at the location of the most signal-like cluster found with the full-sky search. Bottom: upper limit on the gamma-ray flux.

8.2. Candidate list search

The results of the candidate list search are reported in Table 8.2 and shown in Figure 8.6. The most signal-like source in the list is HESS J1023-575, a source coincident with the young stellar cluster Westerlund 2. Three events are located within 1 degree from the source as shown in Figure 8.5.

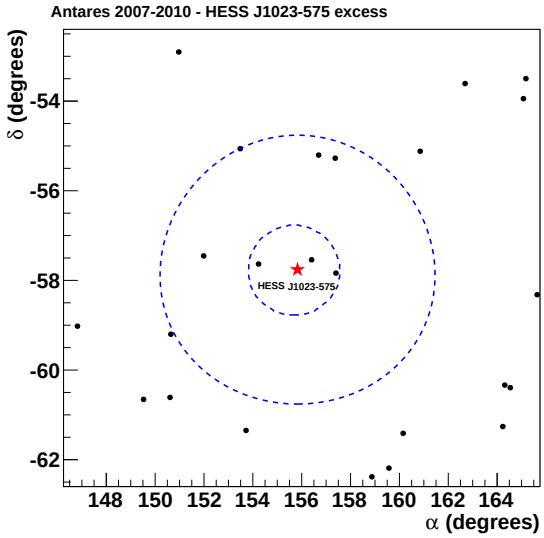

Figure 8.5.: Most signal-like source found in the candidate list search. Three events are within 1 degree from the source. The fit returns $\mu_{\rm s} = 2.0$ with a corresponding test statistic of $\mathcal{Q} = 2.4$, compatible with a background fluctuation.

The fit yields $\mu_{\rm s} = 2.0$ and the corresponding test statistic is $\mathcal{Q} = 2.4$. The probability to have such a fluctuation in one of the candidates in the absence of a signal was determined from pseudo-experiments to be 41%, fully compatible with a background fluctuation. Upper limits at 90% CL, using the FC prescription, are then derived for the normalisation on a neutrino flux proportional to E_ν^{-2} for each of the candidate sources considered. These limits are shown in Figure 8.6. Limits from other neutrino experiments are also indicated. For some sources in the Southern sky the limits set in this analysis are the most restrictive. We remind that for the Southern sky the IceCube detector is more sensitive to ultra high-energy neutrinos with $E_\nu > 1\,\mathrm{PeV}$ [59] which are not relevant for Galactic sources. For this analysis 80% of the signal events has 4 TeV $< E_\nu <$ 700 TeV. To illustrate this, the neutrino flux needed for a 5σ discovery as a function of the neutrino energy for both ANTARES and IceCube is shown in Figure 8.7 for three declinations in the Southern sky. It can be seen that the discovery potentials of ANTARES and IceCube cover different energy ranges.

Table 8.2. Results from the search for high-energy neutrinos from sources in the candidate list. The equatorial coordinates $(\alpha_{\rm s}, \delta_{\rm s})$ in degrees, p-value $({\rm p})$ probability and the 90% C.L. upper limit on the E_ν^{-2} flux intensity $\phi^{90\%{\rm CL}}$ in units of $10^{-8}{\rm GeV}^{-1}{\rm cm}^{-2}{\rm s}^{-1}$ are given (sorted in order of increasing p-value) for the 51 selected sources. When it is not quoted, the p-value is 1.

Source name	$\alpha_s[^\circ]$	$\delta_s[^\circ]$	p	$\phi^{90\%CL}$	Source name	$\alpha_s[^\circ]$	$\delta_s[^\circ]$	p	$\phi^{90\%CL}$
HESS J1023-575	155.83	-57.76	0.41	6.6	SS 433	-72.04	4.98	–	4.6
3C 279	-165.95	-5.79	0.48	10.1	HESS J1614-518	-116.42	-51.82	–	2.0
GX 339-4	-104.30	-48.79	0.72	5.8	RX J1713.7-3946	-101.75	-39.75	–	2.7
Cir X-1	-129.83	-57.17	0.79	5.8	3C454.3	-16.50	16.15	–	5.5
MGRO J1908+06	-73.01	6.27	0.82	10.1	W28	-89.57	-23.34	–	3.4
ESO 139-G12	-95.59	-59.94	0.94	5.4	HESS J0632+057	98.24	5.81	–	4.6
HESS J1356-645	-151.00	-64.50	0.98	5.1	PKS 2155-304	-30.28	-30.22	–	2.7
PKS 0548-322	87.67	-32.27	0.99	7.1	HESS J1741-302	-94.75	-30.20	–	2.7
HESS J1837-069	-80.59	-6.95	0.99	8.0	Centaurus A	-158.64	-43.02	–	2.1
PKS 0454-234	74.27	-23.43	–	7.0	RX J0852.0-4622	133.00	-46.37	–	1.5
IceCube hotspot	75.45	-18.15	–	7.0	1ES 1101-232	165.91	-23.49	–	2.8
PKS 1454-354	-135.64	-35.67	–	5.0	Vela X	128.75	-45.60	–	1.5
RGB J0152+017	28.17	1.79	–	6.3	W51C	-69.25	14.19	–	3.6
Geminga	98.31	17.01	–	7.3	PKS 0426-380	67.17	-37.93	–	1.4
PSR B1259-63	-164.30	-63.83	–	3.0	LS 5039	-83.44	-14.83	–	2.7
PKS 2005-489	-57.63	-48.82	–	2.8	W44	-75.96	1.38	–	3.1
HESS J1616-508	-116.03	-50.97	–	2.7	RCW 86	-139.32	-62.48	–	1.1
HESS J1503-582	-133.54	-58.74	–	2.8	Crab	83.63	22.01	–	4.1
HESS J1632-478	-111.96	-47.82	–	2.6	HESS J1507-622	-133.28	-62.34	–	1.1
H 2356-309	-0.22	-30.63	–	3.9	1ES 0347-121	57.35	-11.99	–	1.9
MSH 15-52	-131.47	-59.16	–	2.6	VER J0648+152	102.20	15.27	–	2.8
Galactic Center	-93.58	-29.01	–	3.8	PKS 0537-441	84.71	-44.08	–	1.3
HESS J1303-631	-164.23	-63.20	–	2.4	HESS J1912+101	-71.79	10.15	–	2.5
HESS J1834-087	-81.31	-8.76	–	4.3	PKS 0235+164	39.66	16.61	–	2.8
PKS 1502+106	-133.90	10.52	–	5.2	IC443	94.21	22.51	–	2.8
					PKS 0727-11	112.58	11.70	–	1.9

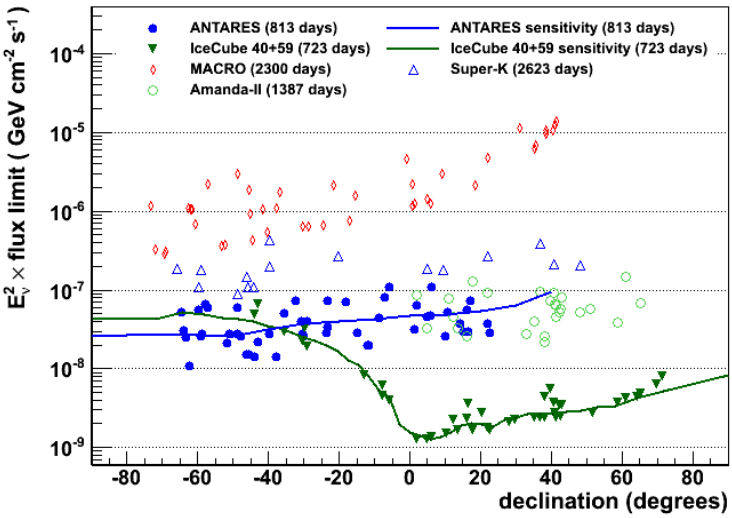

Figure 8.6.: Upper limits set on the normalisation of a neutrino flux proportional to E_ν^{-2} for the 51 candidate sources considered (see also Table 8.2). For a comparison, upper limits from other neutrino experiments are also included [161, 162, 163, 164]. The sensitivity of the analysis is shown as a solid line.

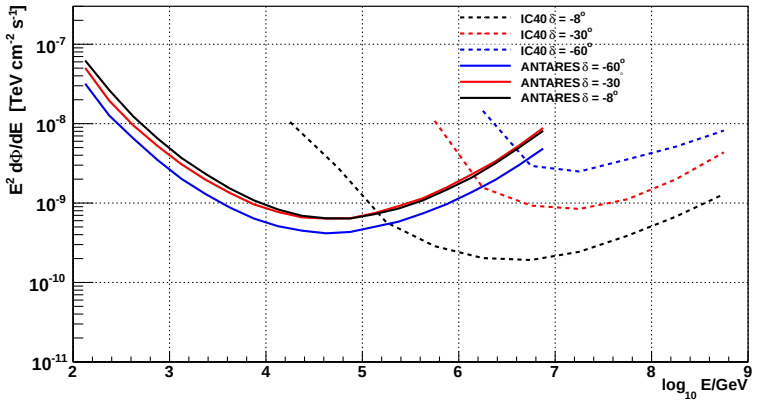

Figure 8.7.: Neutrino flux needed for a 5σ discovery as a function of the neutrino energy for ANTARES (solid line) and IceCube (dashed line) for three declinations in the Southern sky. In this plot, the discovery potential for IceCube with a 40 strings configuration is shown [59].

8.3. Limits on models of astrophysical neutrino emission

In Chapter 2 we presented three Galactic objects which are considered as promising sources of cosmic rays and neutrinos: RX J1713.7-3946, Vela X and the Crab Nebula. These sources are included in the candidate list search and 90% CL upper limits on the normalisation of a neutrino flux proportional to E_ν^{-2} was derived in the previous section.

We now present 90%CL upper limits on the flux normalisation obtained by assuming the models of astrophysical neutrino emission based on gamma-ray flux presented in Chapter 2. For RX J1713.7-3946 and Vela X the measured source extension is taken into account as explained in Section 7.7. Results are shown in Table 8.3 and Figure 8.8 in terms of the Model Rejection Factor (MRF) [165], i.e. the ratio between the 90% CL upper limit and the expected number of signal events. Since the MRF is > 1, the results are not sensitive enough to exclude the models. For RX J1713.7-3949 and Vela X, the limits derived are the most restrictive for the emission models considered.

Source	$\mu_{\rm s}^{90\%CL}$(PNT,E_ν^{-2})	Models	$\mu_{\rm s}^{90\%CL}$ (EXT)	MRF
RX J1713.7-3946	1.88	Kistler & Beacom	1.00	3.8
		Kappes et al.	1.11	8.8
		Morlino et al.	1.07	9
Vela X	1.29	Kistler & Beacom	1.25	3.1
		Kappes et al.	1.25	9.1
		Villante & Vissani	1.47	2.6
Crab	1.57	Kistler & Beacom	1.17	12
		Kappes et al.	1.95	37
		Amato et al.	2.02	26

Table 8.3.: Upper limits on the mean number of signal events, $\mu_{\rm s}$, expected from models of astrophysical neutrino emission for the three sources considered. Also shown are the upper limits on $\mu_{\rm s}$ obtained for the candidate list search which assumes a point-like source and a neutrino flux proportional to E_ν^{-2} (second column). The last column shows the MRF derived.

8.4. KM3NeT

The KM3NeT consortium recently started the construction of a multi-km^3 size neutrino telescope in the Mediterranean Sea [166]. The larger size of KM3NeT will make possible to investigate the Galactic plane with a much better sensitivity than ANTARES.

The expected number of events from RX J1713.7-3946 and Vela X assuming the model from Kappes et al. is shown in Table 8.4. Roughly 6 and 8 years of data taking are required for a 5σ discovery for RX J1713-3946 and Vela X respectively [167, 168].

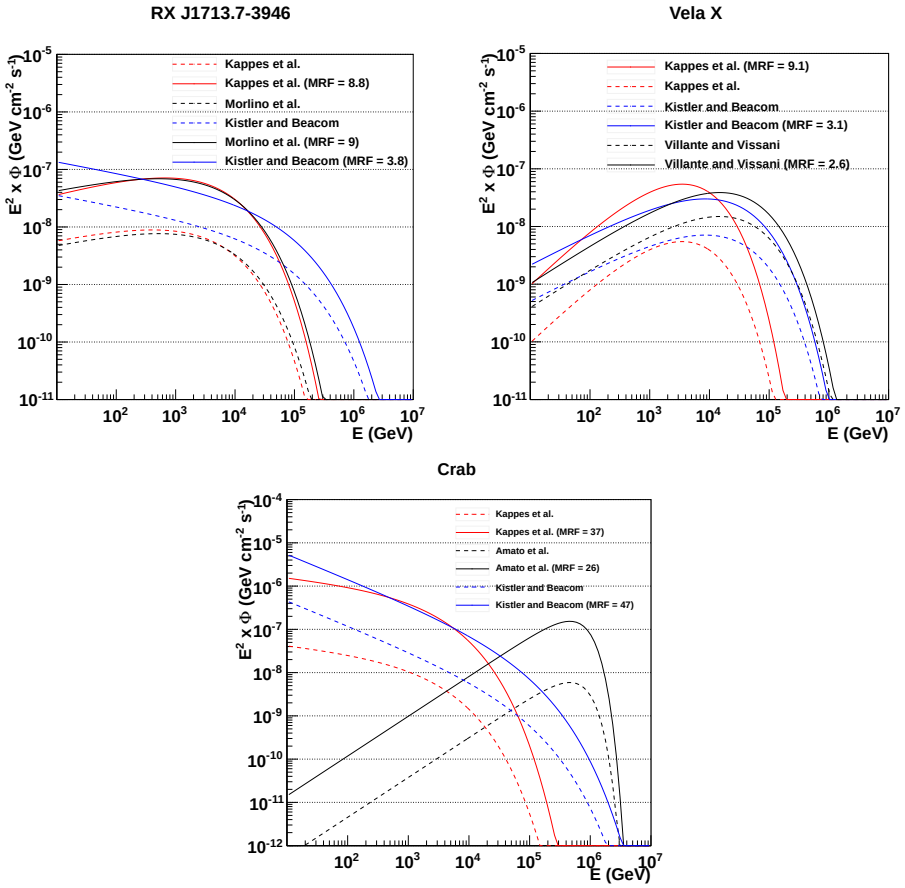

Figure 8.8.: For each of the models of astrophysical neutrino emission described in Section 2 (solid lines), an upper limit has been derived (dashed lines). The sources considered are RX J1713.7-3946 (top left), Vela X (top right) and the Crab SNR (bottom). More detailed results are reported in Table 8.3.

Source	$N_{\rm s}$	$N_{\rm b}$	$N_{\rm yr}^{5\sigma}$
RX J1713.7-3946	30	27	5.8
Vela X	25	23	7.5

Table 8.4.: Number of signal (second column) and background events (third column) according to the Kappes et al. model expected with the KM3Net detector. The last column shows the expected number of years of data taking needed for a 5σ discovery.

8.5. Conclusions and outlook

A search for cosmic neutrino point sources has been presented using data taken from 2007 to 2010 with the ANTARES telescope. A likelihood ratio method has been used in order to search for an excess of signal events over the background composed by atmospheric neutrinos and atmospheric muons. In addition to the position of the reconstructed events, the likelihood takes into account the information of the number of hits as an estimate of the neutrino energy. This improves the discovery potential by roughly 25%.

Two searches have been performed:

- **Full-sky search.** No statistically significant excess of signal has been found. The most signal-like cluster is located at $(\alpha, \delta) = (-46.5°, -65°)$ where 9 signal events are withing a 3 degrees cone. The likelihood fit assigns $\mu_s = 5.1$. The test statistic for this cluster is $\mathcal{Q} = 13.1$ which yields to a p-value of 2.6% with a significance of 2.2σ (two-sided convention).

- **Candidate list search.** The most signal-like source in the candidate list search is HESS J1023-575. The post-trial p-value is 41%, compatible with a background fluctuation. Since no significant excess of events was found, 90% CL upper limits were derived using the FC prescription. For some of the sources in the Southern sky, these limits are at the time of writing the most restrictive, assuming a neutrino flux proportional to E_ν^{-2}.

In this thesis, we also investigated the discovery potential for a neutrino flux model with an exponential cut-off and the inclusion of a possible source extension in the likelihood algorithm. These studies yield to the results presented in Section 7.7. Limits for specific models of astrophysical neutrino emission which deviates from the standard E^{-2} spectrum were computed for three sources: RX J1713.7-3946, Vela X and the Crab SNR. For some of the models considered, the results obtained are the most stringent.

A potential improvement for this analysis is the inclusion of shower events, originating from electron and tau neutrinos, will guarantee a significant improvement in terms of discovery probability ($\sim$ 30% assuming an optimistic $1/3$ as ratio between shower and muon events and 1% contribution from the muon neutrinos background) [169]. Another aspect which would be worth to investigate is the extension of the search to downgoing events [174]. The huge amount of background due to cosmic rays can be reduced by an energy selection (atmospheric muons and neutrinos have a softer spectrum compared to astrophysical neutrinos). The extension of the field of view with the selection of high-energy events would guarantee the possibility to search neutrinos from two very interesting SNRs: Cassiopea A and Tycho. For both sources, the gamma-ray data are well fitted by functions derived from hadronic models [170, 171] and a flux of neutrinos is expected [172].

Finally, a "stacking" search of astrophysical neutrinos from SNRs associated with giant molecular clouds would give interesting results. In Section 1.3 we have reported the recent results from the Fermi-LAT collaboration which identify the SNRs associated with giant molecular clouds IC 443 and W44 as sources of cosmic rays. There are however other sources of the same type whose gamma-ray emission seems to be well described by hadronic

models. Models describing the neutrino emission from these sources have been proposed in [172, 173], unfortunately the flux derived is well below the ANTARES sensitivity. A stacking analysis has the opportunity to search for cosmic neutrinos from this particular type of sources only, with the advantage to improve the significance of the neutrino signal from all sources which is proportional to $\sum_{i=1}^{N} S_i / \sqrt{\sum_{i=1}^{N} B_i}$ where N is the total number of sources, S_i the expected signal from the i-th source and B the total background.

The predicted neutrino flux from these sources assuming the model by Mandelartz and Becker Tjus [173] is shown in Figure 8.9. For comparison the ANTARES E_ν^{-2} upper limits derived for W28, W44, IC443 and W51C are also shown.

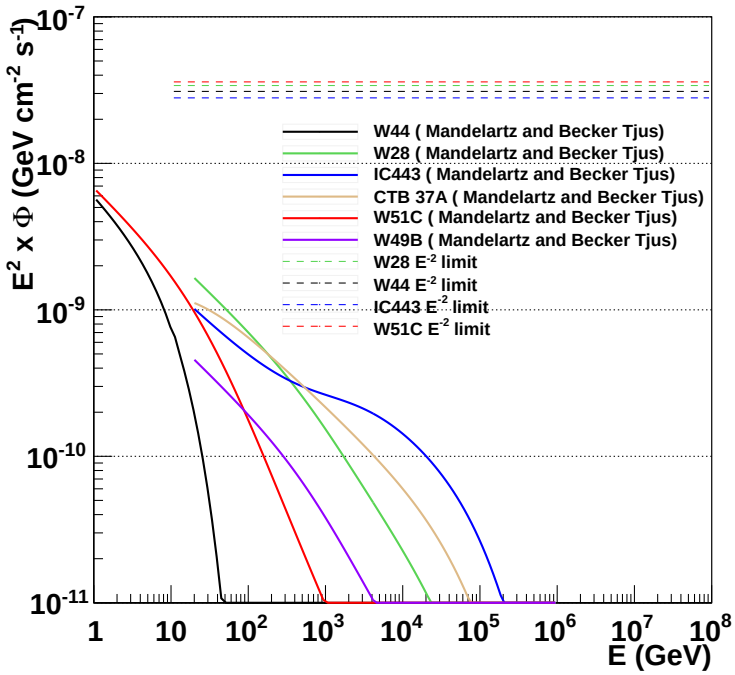

Figure 8.9.: Neutrino flux expected from six supernova remnants associated with giant molecular clouds assuming the model proposed by Mandelartz and Becker Tjus. For W28, W44, IC443 and W51 the ANTARES E_ν^{-2} upper limits are also shown.

Appendices

A. Spectral functions

Several spectral functions have been introduced in this thesis. This appendix lists the main point source spectral models used to fit gamma-ray data. Typical units are $\mathrm{GeV}^{-1}\ \mathrm{cm}^{-2}\ \mathrm{s}^{-1}$.

- **Power-law.** The power-law function can be expressed as:

$$\frac{dN}{dE} = N_0 \left(\frac{E}{E_0}\right)^{\gamma}. \tag{A.1}$$

  where N_0 is the normalization factor, E_0 the energy scale and γ the spectral index. In neutrino astronomy the default spectral index is $\gamma = -2$.

- **Broken power-law.** The broker power-law function has the form:

$$\frac{dN}{dE} = N_0 \times \begin{cases} (E/E_b)^{\gamma_1} & \text{if E} < \text{E}_\text{b} \\ (E/E_b)^{\gamma_2} & \text{otherwise} \end{cases} \tag{A.2}$$

  where E_b is the breaking energy, i.e. the energy at which the spectral index changes from γ_1 to γ_2.

- **Smoothly broken power-law.** The function is a low energy power-law with spectral index γ_1 which smoothly changes its spectral index to γ_2 at breaking energy E_b:

$$\frac{dN}{dE} = N_0 \left(\frac{E}{E_0}\right)^{\gamma_1} \left(1 + \left(\frac{E}{E_b}\right)^{\frac{\gamma_1-\gamma_2}{\beta}}\right)^{-\beta} \tag{A.3}$$

  where β is the smoothness of the break.

- **Exponential cut-off.** The function follows a power-law and rapidly decreases up to a maximum energy E_c:

$$\frac{dN}{dE} = N_0 \left(\frac{E}{E_0}\right)^{\gamma} e^{-E/E_c} \tag{A.4}$$

B. Run selection

In Chapter 6 we have briefly discussed the selection of the runs used in the analysis. In this appendix we describe this selection with more details.

Depending on the detector status and the optical background during data taking, physics runs are divided in the following four categories, called also Quality Basic (QB) flags [177]:

- **QB = 1.** Basic selection of runs for physics analyses.
- **QB = 2.** At least 80% of active OMs.
- **QB = 3.** Baseline rate $\leq$ 120 Hz and burst fraction $\leq$ 0.4.
- **QB = 4.** Baseline rate $\leq$ 120 Hz and burst fraction $\leq$ 0.2.

These run sets are cumulative, meaning that runs satisfying the condition QB = i with i = 2,3,4 satisfy the condition QB = i - 1 as well. All runs with QB $\geq$ 1 were chosen for the analysis. Among other criteria, the runs with QB $\geq$ 1 require these conditions:

1. Apparent run duration close to the effective run duration: $0 \leq \mathrm{T_{app}} - \mathrm{T_{eff}} \leq 450\,\mathrm{s}$. The apperent duration of a run is the time window between the start and the end of that run. The efficient duration corresponds to the livetime of the run, i.e. the product of the number of recorded frames and the frame duration (104.858 ms).
2. No runs which present synchronization problems.
3. No runs with double frames.
4. Muon rate between 0.01 Hz and 100 Hz.

Figure B.1 shows the QB flag for these runs.

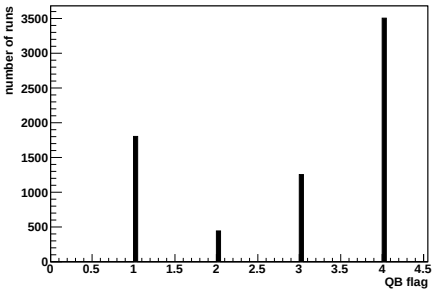

Figure B.1.: Number of selected runs for each of the QB flags.

B.0.1. SCAN runs

For some runs the data taking conditions were not recorded in the database. This makes it very hard to reliably simulate these data. Hence, these runs, flagged as "SCAN", are not included in the final selection. The integrated livetime of the "SCAN" runs is roughly 60 days. It is likely that a large number of these runs were taken under stable conditions, but additional work is required to select such runs. Experts in the ANTARES collaboration are working towards a possible inclusion of "SCAN" runs in all the analyses.

C. Calibration and alignment

Each selected run is calibrated within the SeaTray framework (see for example Chapter five of [178] for a detailed description). The calibration is performed by reading all the necessary parameters from the ANTARES database. In this way for each run the most appropriate calibration set is chosen. Different calibrations were used for different data taking periods as summarised in Table C.1.

The alignment procedure is assigned using a standard calibration software (version 0.994). For a total of 82 runs no valid alignment was found. Hence, the reconstruction of these runs was not possible. However, this is not a big loss since the livetime covered by these runs is roughly few hours.

First run	Last run	Label
25669	26796	2007:L5:v6.0
26770	27658	2007:L5:V6.0-bis
27659	28803	2007:L5:V6.1
28980	29761	2007:L5:V6.1-bis
29762	30427	2007:L5:V6.2
30508	31374	2007:L10:V7.0
31675	32491	2008:L10:V7.1
32529	33756	2008:L10:V7.2
34346	34976	2008:L12:V6.0
35000	36215	2008:L12:V6.1
36218	37475	2008::12:V6.2
37591	38759	2009:L12:V6.3-interlineoffset
38760	39589	2009:L12:V6.4
39590	40809	2009:L12:V6.6
40841	42425	2009:L12:V6.7
42477	42686	2009:L12:V7.1
42756	43282	2009:L12:V7.2
43285	44315	2009:L12:V7.3
45054	45565	2009:L12:V8.1
45459	47263	2010:L12:V2.0
47536	48064	2010:L12:V2.1
48484	49942	2010:L12:V2.2
50225	50955	2010:L12:V2.3
50958	52301	2010:L12:V2.4
52305	52853	2010:L12:V2.5
53074	53483	2010:L12:V2.7
53484	54045	2010:L12:V2.8
54049	54250	2010:L12:V2.9

Table C.1.: Versions of the calibration sets used and the range of runs which they were applied to.

Bibliography

[1] E. C. Krupp, *Echoes of the Ancient Skies: The Astronomy of Lost Civilizations*, Astronomy Series, Courier Dover Publications, 2003.

[2] V. Hess, Observations in low level radiation during seven free balloon flights, *Phys. Zeit*, **12**:1084-1091, 1912.

[3] J. Bl$\ddot{u}$mer, R. Engel and J. R. H$\ddot{o}$randel, *Cosmic rays from the knee to the highest energies*, Progress in Particle and Nuclear Physics, **63**:293, 2009.

[4] K. Nakamura *et al.*, Review of particle physics, *J. Phys.*, G **37**, 075021 (2010).

[5] D. J. Bird *et al.*, Astrophys. J. *The Cosmic ray Energy Spectrum Observed by the Fly's Eye*, **424**:491, 1993.

[6] V. Berezinsky, A. Gazizov, and S. Grigorieva, *Dip in UHECR spectrum as signature of proton interaction with CMB*, Phys. Rev. D**74**, 043005, 2006.

[7] K. Greisen, *End to the Cosmic-Ray Spectrum?*, Phys. Rev. Lett. **16**:748, 1966.

[8] G. Zatsepin and V. Kuzmin, *Upper limit of the spectrum of cosmic rays*, JETP Lett. **4**:78-80, 1966.

[9] C. Bonifazi, *Angular Resolution of the Pierre Auger Observatory*, Proceedings of 29th ICRC, Pune, 2005.

[10] P. Abreu *et al.*, *Update on the correlation of the highest energy cosmic rays with the nearby extragalactic matter*, Astopart. Phys., **34**: 314-326, 2010.

[11] A. Cuoco and S. Hannestad, *Ultra-high energy Neutrinos from Centaurus A and the Auger hot spot*, Phys. Rev. D, **78**, 023007, 2008.

[12] E. Fermi, *On the Origin of the Cosmic Radiation*, Phys. Rev., **75**:1169-1174, 1949.

[13] G. F. Krymskii, *A regular mechanism for the acceleration of charged particles on the front of a shock wave*, Akademiia Nauk SSSR Doklady, **234**: 1306-1308, 1977.

[14] R. D. Blandford and J. P. Ostriker, *Particle Acceleration by Astrophysical Shocks*, Astrophys. J., **221**: L29-L32, 1978.

[15] J. N. Bahcall, A. Dar and T. Piran, *Neutrinos from the Supernova in the LCM*, Nature, **326**:135-136, 1987.

[16] http://www-sk.icrr.u-tokyo.ac.jp/sk/index-e/html

[17] K. S. Hirata *et al.*, *Observation in the Kamiokande-II detector of the neutrino burst from supernova SN1987A*, Phys. Rev. D, **38**:448-458, 1988.

[18] R. M. Bionta *et al.*, *Observation of a neutrino burst in coincidence with supernova SN1987A in the Large Magellanic Cloud*, Phys. Rev. Lett., **58**:1494, 1987.

[19] E. N. Alekseev *et al.*, *Possible detection of a neutrino signal on 23 February 1987 at the Baksan underground scintillation telescope of the institute of nuclear research*, JETP Lett., **45**:589-592, 1987.

[20] R. Claus *et al.*, *A wave shifter light collector for a water cherenkov detector*, Nucl. Instrum. Meth., **A261**:540-542, 1987.

[21] E. N. Alekseev *et al.*, *The Baksan underground scintillation telescope*, Phys. Part. Nucl., **29**:254-256,1998.

[22] G. Pagliaroli, F. Vissani, M. L. Costantini and A. Ianni, *Improved analysis of SN1987A antineutrino events*, Astropart. Phys., **31**:163-176, 2009.

[23] J. Becker, *High energy neutrinos in the context of multimessenger physics*, Phys. Rep., **458**:173-246, 2008.

[24] J. Alvarez-Muniz and F. Halzen, *Possible High-energy neutrinos from the cosmic accelerator RX J1713.7-3946*, ApJ, **576**:L33-L36, 2002.

[25] A. G. Cocco, G. Mangano and M. Messina, *Capturing Relic Neutrinos with β-decaying Nuclei*, J. Cosm and Astr. Phys., **6**:15, 2007.

[26] B. Pontecorvo, *Inverse β-process*, Report PD-205, Chalk River, Canada, unpublished.

[27] P. Anselmann *et al.*, *Solar neutrinos observed by GALLEX at Gran Sasso*, Phys. Lett. B **285**:376-389, 1992.

[28] http://www.sno.phy.queensu.ca

[29] V. Antonelli, L. Miramonti, C. Pen$\tilde{a}$-Garay and A. M. Serenelli, *Solar Neutrinos*, to be published in Special Issue on Neutrino Physics, Advances in High Energy Physics Hindawy Publishing Corporation 2012.

[30] T. Kashti and E. Waxman, *Flavoring Astrophysical Neutrinos: Flavor Ratios Depend on Energy*, Phys. Rev. Lett., **95**:181101, 2005.

[31] W. Bednarek, G. F. Burgio and T. Montaruli, *Galactic discrete sources of high energy neutrinos*, New. Astron. Rev., **49**:1, 2005.

[32] M. L. Costantini and F. Vissani, *Expected neutrino signal from supernova remnant RX J1713.7-3946 and flavor oscillations*, Astropar. Phys., **23**:477-485, 2005.

[33] K. Bernlor *et al.*, *The optical system of the H.E.S.S. imaging atmospheric Cherenkov telescopes, Par I: layout and components of the system*, Astropart. Phys., **20**:111-128, 2003.

[34] R. Cornils *et al.*, *The optical system of the H.E.S.S. imaging atmospheric Cherenkov telescopes, Par II: mirror alignment and point spread function*, Astropart. Phys., **20**:129-143, 2003.

[35] http://veritas.sao.arizona.edu/

[36] C. Baixeras, *The MAGIC Telescope*, Nucl.Phys.B (Proc.Suppl.), **114**:247-252,2003.

[37] F. Aharonian *et al.*, *Detection of TeV gamma-ray emission from the shell-type supernova remnant RX J0852.0-4622 with H.E.S.S.*, Astron. and Astrophys., **437**:L7, 2005.

[38] F. Aharonian *et al.*, *A detailed spectral and morphological study of the gamma-ray supernova remnant RX J1713.7-3946*, Astron. and Astrophys., **449**:223-242,2006.

[39] A. M. Hillas *et al.*, *The Spectrum of TeV Gamma Rays from the Crab Nebula*, ApJ, **503**:744,1998.

[40] W. B. Atwood *et al.*, *The Large Area Telescope on the Fermi Gamma-Ray Space Telescope*, ApJ, **697**:1071, 2009.

[41] M. Ackermann *et al.*, *Detection of the Characteristic Pion-decay Signature in Supernova Remnants*, Science, **339**:807-811, 2013.

[42] F. Aharonian *et al.*, *First detection of a VHE gamma-ray spectral maximum from a Cosmic source: H.E.S.S. discovery of the Vela X nebula*, Astron. and Astrophys., **448**:L43-L47,2006.

[43] F. Aharonian *et al.*, *3.9 day orbital modulation in the TeV gamma-ray flux and spectrum from the X-ray binary LS 5039*, Astron. and Astrophys., **460**:743-749,2006.

[44] J. Albert *et al.*, *Variable Very-High-Energy Gamma-Ray Emission from the Microquasar LS I +61 303*, Science, **312**:1771-1773,2006.

[45] C. Distefano *et al.*, *Neutrino Flux Predictions for know Galactic Microquasars*, ApJ, **575**:378-383, 2002.

[46] S. Adrián-Martínez *et al.*, *A time dependent search for neutrino emission from microquasars with the ANTARES neutrino telescope*, t.b.s., 2013.

[47] F. Aharonian *et al.*, *Very high energy gamma rays from the direction of Sagittarius A**, Astron. and Astrophys., **425**:L13-L17,2004.

[48] F. Aharonian *et al.*, *Very high energy gamma rays from the composite SNR G0.9+0.1*, Astron. and Astrophys., **432**:L25-L29,2005.

[49] F. Acero *et al.*, *Localising the VHE gamma-ray source at the Galactic Center*, MNRAS, **402**:1877-1882, Issue 3,2009.

[50] M. D. Kistler and J. F. Beacom, *Guaranteed and Prospective Galactic TeV Neutrino Sources*, Phys. Rev. D., **74**:063007,2006.

[51] C. Lunardini and S. Razzaque, *High Energy Neutrino Emission from the Fermi Bubbles*, Phys. Rev. Lett., **108**:221102, Issue 22, 2012.

[52] F. Halzen and E. Zas, *Neutrino fluxes from active galaxies: a model independent estimate*, Astrophys. J., **488**:669, 1997.

[53] F. W. Stecker, *Note on high-energy neutrinos from active galactic nuclei*, Phys. Rev. D., **72**:107301,2005.

[54] J. K. Becker, P. L. Biermann and W. Rhode, *The diffuse neutrino flux from FR-II radio galaxies and blazars: a source property based estimate*, Astropart. Phys., **23**:355-368, 2005.

[55] V. Agrawal *et al.*, *Atmospheric neutrino flux above 1 GeV*, Phys. Rev. D., **53**:1314-1323, 1996.

[56] R. Abbasi *et al.*, *A Search for a Diffuse Flux of Astrophysical Muon Neutrinos with the IceCube 40-String Detector*, Phys. Rev. D., **84**:082001, 2011.

[57] J. A. Aguilar *et al.*, *Search for a diffuse flux of high-energy ν_μ with the ANTARES neutrino telescope*, Phys. Lett. B., **696**:16-22,2011.

[58] J. Becker, P. L. Biermann, J. Dreyer and T. M. Kneiske, *Cosmic Rays VI: Starburst galaxies at multiwavelengths*, A&A, 2009, arXiv:0901.1775.

[59] R. Abbasi *et al.*, *Time integrated search for Point-like Sources of Neutrinos with the 40-string IceCube Detector*, Ap.J., **732**:18, 2011.

[60] K. Murase, S. Inoue and S. Nagataki, *Cosmic rays above the second knee from clusters of galaxies and associated high-energy neutrino emission*, Ap. J., **689**:L105-L108, 2008.

[61] E. Waxmann and J. N. Bahcall, *High Energy Neutrinos from Astrophysical Sources: An Upper Bound*, Phys. Rev. D., **59**, 023002, 1999.

[62] E. Waxmann and J. N. Bahcall, *High energy astrophysical neutrinos: the upper bound is robust*, Phys. Rev. D., **64**, 023002, 2001.

[63] K. Mannheim, R. J. Protheroe and J. P. Rachen, *On the cosmic ray bound for models of extragalactic neutrino production*, Phys. Rev. D., **64**, 2001.

[64] P. Sreekumar *et al.*, *EGRET Observations of the Extragalactic Gamma-Ray Emission*, Ap.J., **494**:523-534, 2000.

[65] T. J. Galama *et al.*, *An unusual supernova in the error box ot the gamma-ray burst of 25 April 1998*, Nature, **395**:670-672, 2008.

[66] E. Waxmann and J. Bahcall, *High energy neutrinos from cosmological gamma-ray burst fireballs*, Phys. Rev. Lett., **78**:2292-2295, 1997.

[67] D. Guetta *et al.*, *Neutrinos from individual gamma-ray bursts in the BATSE catalog*, Astropart. Phys., **20**:429-455, 2004.

[68] R. Abbasi *et al.*, *An absence of neutrino associated with cosmic-ray acceleration in γ-ray bursts*, Nature, **484**:351, 2012.

[69] R. Abbasi *et al.*, *Search for muon neutrinos from gamma-ray bursts with the IceCube neutrino telescope*, Ap.J., **710**:346-359, 2010.

[70] M. Tavani *et al.*, *The AGILE mission*, Astron. and Astrophys., **502**:995-1013, 2009.

[71] P. Nolat *et al.*, , ApJS, **199**:31-77, 2012.

[72] F. Aharonian *et al.*, *The H.E.S.S. survey of the Inner Galaxy in very high-energy gamma-rays*, Ap.J., **636**:777-797, 2006.

[73] J. A. Hinton and W. Hofman, *Teraelectronvolt Astronomy*, ARA&A, **47**, Issue 1, 523-565, 2009.

[74] D. Ellison *et al.*, *Particle Acceleration in Supernova Remnants and the Production of Thermal and Nonthermal Radiation*, ApJ, **712**:861, 2008.

[75] Z. R. Wang, Q.-Y. Qu and Y. Chen, *Is RX J-1713.7-3946 the remnant of the AD393 guest star?*, Astron. and Astrophys., **318**:L59-L61, 1997.

[76] Y. Fukui *et al.*, PASJ, **55**:L61, 2003.

[77] E. Pfeffermann and B. Aschenbach, *Rosat observation of a new supernova remnant in the constellation scorpius*, Roentgenstrahlung from the Universe, 267-268, 1996.

[78] T. Tanaka *et al.*, *Study of Nonthermal Emission from SNR RX J1713.7-3946 with Suzaku*, ApJ., **685**, 988, 2008.

[79] H. Muraishi *et al.*, *Evidence for TeV gamma-ray emission from the shell type SNR RX J1713.7-3946*, A&A, **354**:L57-L61, 2000.

[80] F. Aharonian *et al.*, *Primary particle acceleration above 100 TeV in the shell-type Supernova Remnant RX J1713.7-3946 with deep H.E.S.S. observations*, Astron. and Astrophys., **464**:235-243, 2007.

[81] A. A. Abdo *et al.*, *Observations of the young Supernova remnant RX J1713.7-3946 with the Fermi Large Area Telescope*, ApJ, **734**:28, 2011.

[82] V. N. Zirakashvili and F. A. Aharonian, *Nonthermal radiation of young supernova remnants: the case of RX J1713.7-3946*, ApJ, **708**:965-980, 2010.

[83] M. A. Malkov, *Asymptotic Particle Spectra and Plasma Flows at Strong Shocks*, ApJL, **511**:53, 1999.

[84] T. Inoue *et al.*, *Toward understanding the cosmic-rays acceleration at young supernova remnants interacting with interstellar clouds: possible applications to RX J1713.7-3946*, ApJ, **744**:71, 2012.

[85] R. Dodson *et al.*, *The Vela Pulsar's Proper Motion and Parallax Derived from VLBI Observations*, ApJ, **596**:1137, 2003.

[86] A. Abramowsky *et al.*, *Probing the extent of the non-thermal emission from the Vela X region at TeV energies with H.E.S.S.*, submitted to Astron. and Astrophys. .

[87] O. C. de Jager, P. O. Slane & S. LaMassa, *Probing the radio to X-ray connection of the Vela X PWN with Fermi LAT and H.E.S.S.*, ApJ, **689**:125, 2008.

[88] T. C. Weekes *et al.*, *Observation of TeV gamma rays from the Crab nebula using the atmospheric Cerenkov imaging technique*, ApJ, **342**: 379, 1989.

[89] P. Goret *et al.*, *Observations of TeV gamma rays from the Crab nebula*, Astron. and Astrophys., **270**:401-406, 1993.

[90] P. Baillon *et al.*, *Gamma ray spectrum of the Crab nebula in the multi TeV region*, Astropart. Phys., **1**: 341-355, 1993.

[91] F. Aharonian *et al.*, *Observations of the Crab Nebula with H.E.S.S.*, Astropart. Phys., **22**:109-125, 2004.

[92] M. Tavani *et al.*, *Discovery of powerful γ-ray flares from the Crab Nebula*, Science, **331**:736-739, 2011.

[93] A. A. Abdo *et al.*, *γ-ray flares from the Crab Nebula*, Science, **331**:739-742, 2011.

[94] R. Zanin *et al.*, *MAGIC measurement of the Crab Nebula spectrum over three decades in eenergy*, Proceedings of the 32nd ICRC, 2011.

[95] A. Kappes *et al.*, *Potential Neutrino Signal from Galactic γ-Ray Sources*, ApJ, **656**:870-878, 2007.

[96] S. R. Kelner, F. A. Aharonian and V. V. Bugayov, *Energy spectra of gamma-rays, electrons and neutrinos produced at proton-proton interactions in the very high energy regime*, Phys. Rev. D., **74**:3, 2006.

[97] G. Morlino, P. Blasi and E. Amato, *Gamma Rays and Neutrinos from SNR RX J1713.7-3946*, Astropart. Phys., **31**:376-382, 2009.

[98] E. Amato and P. Blasi, *A general solution to non-linear particle acceleration at non-relativist shock waves*, MNRAS, **364**:L76-L80, 2005.

[99] E. Amato and P. Blasi, *Non linear particle acceleration at non-relativistic shock waves in the presence of self-generated turbulence*, MNRAS, **371**:1251-1258, 2006.

[100] F. L. Villante and F. Vissani, *How precisely neutrino emission from supernova remnants can be constrained by gamma ray observations?*, Phys. Rev. D,**78**:103007, 2008.

[101] B. Link and F. Burgio, *Flux predictions of high-energy neutrinos from pulsars*, MNRAS, **371**:375-379, 2006.

[102] E. Amato, D. Guetta and P. Blasi, *Signatures of high energy protons in pulsar winds*, Astron. and Astrophys., **402**:827-836, 2003.

[103] Y. Gallant and J. Arons, *Structure of relativistic shocks in pulsar winds: a model of the wisps in the Crab Nebula*, ApJ, **435**:230-260, 1994.

[104] M. A. Markov, *On high energy neutrino physics*, Proceedings of the 10^{th} International Conference on High Energy Physics, 1960.

[105] S. L. Glashow, *Resonant scattering of antineutrinos*, Phys. Rev., **118**:316, 1960.

[106] R. Gandhi *et al.*, *Ultrahigh-energy neutrino interactions*, Astropart. Phys, **5**:81, 1996.

[107] R. Gandhi *et al.*, *Neutrino interactions at ultrahigh energies*, Phys. Rev. D**58**, 093009, 1998.

[108] H. L. Lai *et al.*, *Improved Parton Distributions from Global Analysis of Recent Deep Inelastic Scattering and Inclusive Jet Data* Phys. Rev. D., **55**, 1280, 1997

[109] J. Pumplin *et al.* (CTEQ Collaboration), *New generation of parton distributions with uncertainties from global QCD analysis*, JHEP, **07**:12, 2002.

[110] S. Klimushin, E. Bugaev and I. Sokalsky, *Precise parametrizations of muon energy losses in water*, Proceedings of the 28th ICRC, 2001.

[111] P. A. Cherenkov, *Visible radiation produced by electrons moving in a medium with velocities exceeding that of light*, Phys. Rev., **52**:378, 1937.

[112] J. V. Jelley, *Cherenkov radiation and its application*, Pergamon Press, Oxford, UK.

[113] J. G. Learned and S. Pakvasa, Astropart. Phys., **3**:267, 1995.

[114] T. De Young, S. Razzaque and D. F. Cowen, *Astrophysical tau neutrino detection in kilometer-scale Cherenkov detectors via muonic tau decay*, Astropart. Phys., **27**:238-243, 2007.

[115] H. Hanada et al., *A highly sensitive optical detector for use in deep underwater*, Nucl. Instrum. Meth., **A408**:425-437, 1998.

[116] The Baikal Collaboration, *The Baikal neutrino project: Status report*, Nucl. Phys. B (Proc. Suppl.), **91**:438, 2001.

[117] J. A. Aguilar *et al.*,, *Transmission of light in deep sea water at the site of the ANTARES neutrino telescope*, Astroparticle Physics, **23**:131, 2005.

[118] C. Spiering, *Neutrino astrophysics in the cold: AMANDA, Baikal and IceCube*, Physica Scripta, **T 121**:112, 2005.

[119] P. Coyle, *The ANTARES Deep-Sea Neutrino Telescope: Status and First Results*, Proceedings of the 31^{st} International Cosmic Rays Conference, Lódź, Poland, 2009, e-Print: arXiv:1002.0754 [astro-ph.HE].

[120] P. Amran *et al.*, *The ANTARES optical module*, Nucl. Instrum. Methods, **A484**:369, 2002.

[121] J. A. Aguilar *et al.*, *AMADEUS - The Acoustic Neutrino Detection Test System of the ANTARES Deep-Sea Neutrino Telescope*, NIMA, **626**:128-143, 2011.

[122] J. A. Aguilar *et al.*, *The data acquisation system for the ANTARES neutrino telescope*, Nucl. Instrum. Meth., **A 570**:107-116, 2007.

[123] J. Ageron *et al.*, *The ANTARES optical beacon system*, Nucl. Instrum. Meth., **A 578**: 498, 2007.

[124] J. Aguilar *et al.* (ANTARES Collaboration), *Transmission of light in deep sea water at the site of the ANTARES neutrino telescope*, Astropartile Physics, **23**:131-135, 2005.

[125] A. Brown, *Positioning system of the ANTARES neutrino telescope*, Proceedings of the 31th ICRC, Lódź, 2009, e-Print: arXiv:0908.0814 [astro-ph.HE].

[126] G. Halladjian, *Recherce de neutrinos cosmiques de haute-energie emis par des sources ponctuelles avec ANTARES*, Ph.D. Thesis, 2010.

[127] D. Zaborov, Ph.D. Thesis, 2010.

[128] R. Abbasi *et al.*, *A search for a diffuse flux of astrophysical neutrinos with the IceCube 40-strings detector*, Phys. Rev. D, **84**, 082001, 2011.

[129] E. Zas, F. Halzen and R. A. Vaśquez, *High energy neutrino astronomy: horizontal air showers versus underground detectors*, Astroparticle Physics, **1**:297, 1993.

[130] Y. Becherini, A. Margiotta, M. Sioli and M. Spurio, *A parameterisation of single and multiple muons in deep water and ice*, Astroparticle Physics, **25**:1-13, 2006.

[131] V. Agrawal *et al.*, *Atmospheric neutrino flux above 1 GeV*, Phys. Rev. D, **53**:1314, 1996.

[132] M. de Jong, *The ANTARES Trigger Software*, Antares Internal Note, 2005.

[133] A. J. Heijboer, *Track reconstruction and point source searches with ANTARES*, Ph.D. Thesis, 2004.

[134] D. Bailey, *Monte Carlo tools and analysis methods for understanding the ANTARES experiment and predicting its sensitivity to Dark Matter*, Ph.D. Thesis, 2002.

[135] Parameters of the Preliminary Reference Earth Model are given by Adam Dziewonsky, Earth Structure, Global, in: *The Encyclopedia of Solid Earth Geophysics*, David E. James, ed. (Van Nostrand Reinhold, New York, 1989) p.331.

[136] G. D. Barr, T. K. Gaisser, P. Lipari, S. Robbins and T. Stanev, *Three-dimensional calculation of atmospheric neutrinos*, Phys. Rev. D., **70**:023006, 2004.

[137] P. Antonioli *et al.*, *A three-dimensional code for muon propagation through the rock: MUSIC*, Astropart. Phys., **7**:357-368, 1997.

[138] G. Carminati *et al.*, *Atmospheric MUons from PArametric formulas: A fast GEnerator for neutrino telescopes*, Comp. Phys. Comm., **179**:915-923, 2008.

[139] Y. Becherini *et al.*, *A parameterisation of single and multiple muons in the deep water or ice*, Astropart. Phys., **25**:1-13, 2006.

[140] J. Brunner, *Geasim: User manual*, ANTARES Internal Note.

[141] S. Navas and L. Thompson, *KM-A7 User Guide and Reference Manual*, ANTARES Internal Note, 1999.

[142] GEANT program manual, CERN program library long writeup, W5013, 1993.

[143] A. Heijboer, *TTS Analysis*, Antares Collaboration Meeting, September 2011, Bamberg.

[144] W. H. Press *et al.*, *Numerical recipes in C*, Cambridge University Press, 1993.

[145] Z. Zhang, *Parameter estimation techniques: A tutorial with application to conic fitting*, Image and Vision Computing Journal, **15**:59, 1997.

[146] http://root.cern.ch/root/html/TProfile.html

[147] C. Bogazzi, *Point source search with 2007-2010 data*, Antares Internal Note, 2011.

[148] E. V. Korolkova and L. Thompson, *Monte Carlo simulation of cosmic ray muons at sea level with corsika*, Antares Internal Note, 2003.

[149] E. V. Bugaev *et al.*, *Prompt leptons in cosmic rays*, Nuovo Cimento, **12**:41-73, 1988.

[150] J. A. Aguilar *et al.*, *Zenith distribution and flux of atmospheric muons measured with the 5-line ANTARES detector*, Astropart. Phys., **34**:179, 2010.

[151] C. Riviere, Run-by-run Monte Carlo simulation for ANTARES: v2, Antares Internal Note, 2012.

[152] S. Adrián-Martínez *et al.*, Search For Cosmic Neutrino Point Sources with Four Years of Data from the ANTARES Telescope, ApJ, **760**:53, 2012.

[153] G. J. Feldman and R. D. Cousins, *Unified approach to the classical statistical analysis of small signals*, Phys. Rev. D, **57**:3873-3889, 1997.

[154] S. Adrián-Martínez *et al.*, First Search for Point Sources of High Energy Cosmic Neutrinos with the ANTARES detector, ApJL, **743**:14, 2011.

[155] A. I. Nikishov, Soviet. Phys. JETP, **14**:393, 1962.

[156] R. L. Gould and G. P. Schreder, *Opacity of the Universe to High-Energy Photons*, Phys. Rev. Lett., **16**:252, 1966.

[157] J. V. Jelley, *High-energy gamma-ray absorption in space by 3.5 °K microwave field*, Phys. Rev. Lett., **16**:479, 1966.

[158] Fits data from: http://www.mpi-hd.mpg.de/hfm/HESS/pages/publications/auxiliary/VelaX_auxinfo.h
.

[159] Fits data from: http://www.mpi-hd.mpg.de/hfm/HESS/pages/publications/auxiliary/auxinfo_rxj1713

[160] F. Schussler *et al.*, *Multimessenger analysis of the ANTARES neutrino excess*, Proceedings of the 33rd ICRC, Rio de Janeirio, July 2013.

[161] M. Ambrosio *et al.*, *Neutrino astronomy with the MACRO detector*, ApJ, **546**:1038, 2001.

[162] E. Thrane *et al.*, *Search for astrophysical neutrino point sources at Super-Kamiokande*, ApJ, **704**:503, 2009.

[163] R. Abbasi *et al.*, *Search for point sources of high energy neutrinos with final data from AMANDA-II*, Phys.Rev. D., **79**, 062001, 2009.

[164] T. Montaruli, *IceCube point source results and CR composition sensitivity*, talk at NuSKY, Trieste, 2011.

[165] G. C. Hill and K. Rawlins, *Unbiased cut selection for optimal upper limits in neutrino detectors: the model rejection potential technique*, Astropart. Phys., **19**:393, 2003.

[166] A. Margiotta, *The KM3NeT project: status and perspectives*, Geosci. Instrum. Method. Data Syst., **2**:35-40, 2013.

[167] R. Coniglione, *KM3NeT detection perspective of RX J1713.7-3946*, KM3NeT Collaboration Meeting, Marseille, 2013.

[168] R. Coniglione, *Discovery potential of Galactic sources*, KM3NeT Collaboration Meeting, Marseille, 2013.

[169] S. Schulte, *Update on NIKHEF point sources analysis*, ANTARES Collaboration Meeting, Marseille, June 2013.

[170] A. A. Abdo *et al.*, *FERMI-LAT discovery of GeV gamma-ray emission from the young supernova remnant Cassiopea A*, Apj, **710**:L92-L97, 2010.

[171] G. Morlino and D. Caprioli, *Strong evidence for hadron acceleration in Tycho's supernova remnant*, A&A, **538**:A81, 2012.

[172] Q. Yuan, P-F. Yin and X-J. Bi, *Neutrino emission of Fermi supernova remnants*, Astropart. Phys., **35**:33-38, 2011.

[173] M. Mandelartz and J. Becker-Tjus, *A statistical study of Galactic SNR source spectra detected at $>$ GeV energies*, ArXiv e-print, http://arxiv.org/abs/1301.2437

[174] S. Gkaitatzis, *Point Source Searches Using High-Energy Down-going Neutrinos with the ANTARES Telescope*, University of Amsterdam, 2011.

[175] http://www.aps.org

[176] C. Sutton, *Spaceship Neutrino*, Cambridge University Press, 1992.

[177] V. van Elewyck, *Data quality*, talk at the ANTARES Collaboration Meeting, November 2010, Amsterdam.

[178] E. Presani, *Neutrino induced showers from gamma-ray bursts*, Ph.D. Thesis, 2011.

Summary

During these four years of research as a Ph.D. student, I have tried several times to explain to my family and friends what I was doing. I am not sure I succeeded since many times I was not able to finish the conversation. Though I have to admit, the look on their face when I introduced "mysterious" topics such as cosmic rays acceleration and the ANTARES detection principle was pretty funny. This summary is probably my last attempt to explain them what I did in The Netherlands in the last four years, so I hope that a more expert reader will not be disappointed if I will first start with a general introduction to astronomy and cosmic rays. After this, I will focus on ANTARES and start to explain how it is possible to detect this elusive particle, called neutrino, with a big detector at the bottom of the sea. Finally, the third and last part of this summary will describe the results obtained.

1. Multimessenger astronomy

Almost a thousand years ago, in 1054 A.D., Chinese, Japanese and Arab astronomers observed the presence of a new "guest" star in the constellation Taurus. At the time, astronomers used the term "guest" to identify bright celestial objects which temporarily appear in the sky where no star had previously been observed. Although it was clear that this guest star was somehow different from what we now called comets, they could not know what they were observing: a supernova explosion.

When a massive star burns up all of its hydrogen fuel, it begins a gravitational collapse. The equilibrium is broken, the radiation pressure from the nuclear reactions can no longer sustain the gravitational pressure due to the star's own mass. Due to the collapse, the density and the temperature of the star increase reaching the critical values which start the process of helium burning. This restores the equilibrium. After the helium is also exhausted, the collapse continues until the fusion of heavier elements of the iron group starts. This mechanism, which strongly depends on the initial mass of the star, continues until the fusion reactions stop and the star collapses under its own gravitational pressure. This implosion may give rise to ejection of stellar matter into the interstellar space and the release of an enormous amount of energy. The material is ejected at a velocity up to 30.000 km/s and a shock wave is created by the interaction of the material with the interstellar medium. This shock wave sweeps up the surrounding shell of gas and dust, creating what is now called a remnant. A neutron star, or a black hole if the star was very massive, is now formed.

This is what happened to the "guest" star observed in 1054 A.D.. We now refer to this supernova remnant as the Crab Nebula which is shown in Figure 1. The Crab Nebula is located at a distance of approximately 2 kpc from the Earth, which means that the light emitted by this object travels for 6523 years before reaching our planet.

Summary

In the last 50 years, the Crab Nebula has become one of the most studied object of our Galaxy mainly due to its brightness and historical importance. These observations were made at different wavelengths: from the radio to the visible band, and from x-ray to the gamma-ray band.

What is more important for the work presented in this thesis is that the Crab Nebula and other Galactic supernovae are responsible for the acceleration of cosmic rays. Beside supernovae other objects are considered possible candidate sources like the Galactic plerions and microquasars or the extra-Galactic gamma-ray bursts and active galactic nuclei.

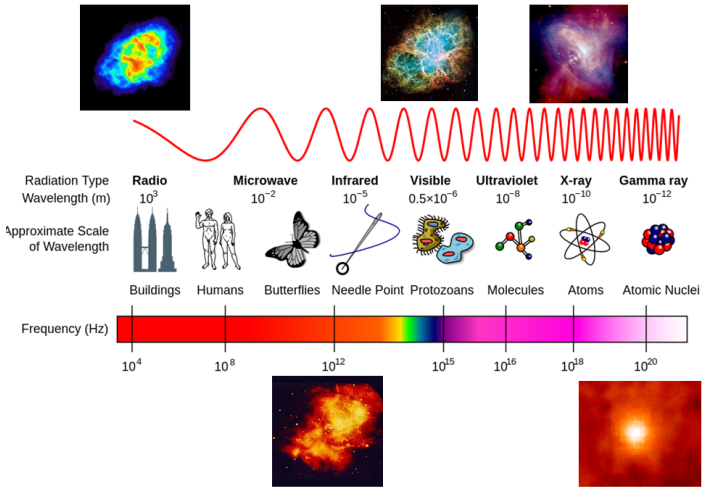

Figure 1.: A schematic representation of the electromagnetic spectrum with pictures of the Crab Nebula observed at different wavelengths.

Cosmic rays

Cosmic rays are energetic particles which continuously hit and penetrate the Earth's atmosphere. They were discovered at the beginning of the 20th century by Victor Hess who carried three electrometers to an altitude of 5.3 km using balloons with the purpose to investigate the ionisation of the atmosphere (see Figure 2). To his surprise, he observed that the ionisation rate at the highest altitudes was larger than at the ground. The only possible explanation was that the radiation comes from above, with extra-terrestrial origin.

One century after their discovery, there are still many open questions about cosmic rays. Are supernovae the sources responsible for the acceleration of cosmic rays? How does this acceleration work exactly? What are the "knee" and the "ankle" of the energy spectrum? One way to answer these question is to search for and detect astrophysical neutrinos. This is the subject of this thesis.

Figure 2.: Victor Hess ready to measure the ionisation of the atmosphere with his balloon. Picture taken from [175].

Neutrino production

Neutrinos are neutral particles which interact only via the weak force. Their existence was first proposed in 1930 by Wolfgang Pauli to explain the conservation of energy and angular momentum in beta decay. Very famous is the comment said by Pauli about it: "I have done a terrible thing, I have postulated a particle that cannot be detected" [176]. Fortunately (for this thesis), this statement was proven wrong 25 years later when Reines and Cowan detected antineutrinos created in a nuclear reactor by beta decay.

The reader would probably ask at this point: "What is the relation between cosmic rays and neutrinos?". The answer of this question is the key to understand my work. Neutrinos and cosmic rays share the same origin, i.e., they are created by the same sources. The production of high-energy neutrinos is due to the interaction of accelerated cosmic rays, mostly nucleons, with dense matter or photons field near the cosmic-ray source. The nucleon-photon interactions are for example:

$$p + \gamma \to \Delta^+ \to \pi^0 + p,$$
$$p + \gamma \to \Delta^+ \to \pi^+ + n.$$

$$n + \gamma \to \Delta^0 \to \pi^0 + n,$$
$$n + \gamma \to \Delta^0 \to \pi^- + n.$$

The main channels for nucleon-nucleon processes are:

$$p + p \to p + p + \pi^0,$$
$$\to p + n + \pi^+.$$

$$p + n \to p + n + \pi^0,$$
$$\to p + p + \pi^-.$$

All these reactions produce so-called pions, the lightest mesons. Pions are unstable particles, therefore they decay. Charged pions decay into muons, a lepton similar to the electron but more massive, producing a muon neutrino. The decay of the muons into electrons generates another muon neutrino, and an additional electron neutrino. Neutral pions decay into two gamma-ray photons:

$$\begin{aligned}
&\pi^0 \to \gamma + \gamma \\
&\pi^+ \to \mu^+ + \nu_\mu \to e^+ + \nu_e + \bar{\nu}_\mu + \nu_\mu \\
&\pi^- \to \mu^- + \bar{\nu}_\mu \to e^- + \bar{\nu}_e + \nu_\mu + \bar{\nu}_\mu.
\end{aligned}$$

Beside neutral pion decay, there are other processes which contribute to gamma-ray emission. It is common to distinguish between the hadronic process, i.e., the π^0 decay, and leptonic processes such as synchrotron emission and inverse Compton scattering. The typical gamma-ray energy spectrum for a source can be divided in two parts. The low-energy range is dominated by synchrotron emission. Inverse Compton emission and neutral pion decay contribute to the high-energy part of the spectrum, usually up to tens of TeV. The detection of TeV gamma-rays from a specific source is considered the first hint for a possible neutrino emission, however there is no way to distinguish a-priori whether the photons detected are of leptonic or hadronic origin. Many theoretical models are trying to explain the spectral energy distribution for several candidate sources of cosmic rays. These models strongly depend on source parameters, such as the magnetic field and the proton density, which can only be inferred. For hadronic models, it is clear that the detection of a signal of astrophysical neutrinos could constrain the interval of allowed parameters assumed. While cosmic rays are deflected by Galactic and extra-Galactic magnetic fields, and gamma-rays interact with the cosmic microwave background, neutrinos point back to their source.

2. Neutrino astronomy with ANTARES

The detection of astrophysical neutrinos was first proposed in the 1960's by the Russian physicist Moisei Aleksandrovich Markov [104]. He suggested to "install detectors deep in a lake or sea water and determine the direction of the charged particles with the help of Cherenkov radiation". The idea is that neutrinos emitted by an astrophysical source interact with matter via charged current interactions and create leptons[1]. While travelling in the water, these leptons emit Cherenkov radiation.

This concept was adapted by the ANTARES collaboration to build the first neutrino telescope in the Mediterranean Sea. ANTARES is a three-dimensional array of 885 photomultiplier tubes looking 45° downward and distributed along 12 detection strings. An illustration of ANTARES is shown in Figure 3.

The detector performance is expressed in terms of the angular resolution and the acceptance, and is obtained by simulations. For the data analysed in this work, assuming a neutrino flux proportional to E_ν^{-2}, the angular resolution derived from simulations is 0.46±0.10 degrees. The effective area, i.e. the equivalent area of a 100% efficient detec-

[1] Neutral current interactions are also possible, however they are not considered in this work.

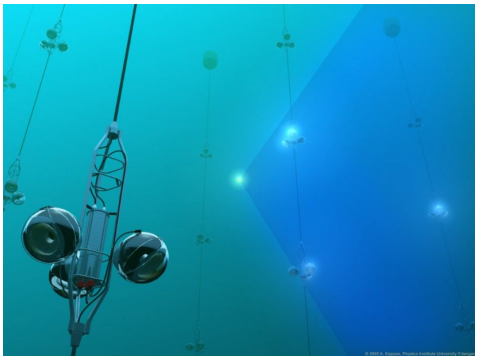

Figure 3.: Illustration of the ANTARES detector. Credits to Alexander Kappes.

tor, increases with the neutrino energy and is roughly 0.1, 1 and 10 m^2 at 1, 100 and 10000 TeV respectively.

3. My work

During my four years with ANTARES, I was involved in the search for point-like sources of astrophysical neutrinos. The presence of an excess of cosmic neutrinos above the background is tested by looking for clusters of events in a given direction. Therefore, a good angular resolution is necessary.

The analysis presented in this thesis is based on four years of data collected from January 2007 to December 2010. The total observation time equals 813 days.

Neutrino candidates were selected by applying three different cuts. First, only tracks reconstructed as upgoing are selected. Cuts on the reconstruction quality variables, β and Λ, are then applied in order to reject misreconstructed atmospheric muons. These cuts were chosen in order to optimise the discovery potential, i.e., the neutrino flux needed to have a 50% chance of discovering the signal with a 5σ significance level assuming an E_ν^{-2} spectrum. The final sample consists of 3058 neutrino candidates. Simulations predict 358 ± 179 atmospheric muons and 2408 ± 72 atmospheric neutrinos.

The search is based on a likelihood ratio method. The null hypothesis is represented by the background only case (only atmospheric muons and neutrinos in data). The alternative hypothesis refers to the case where in addition to the background a signal is also present with a flux proportional to E_ν^{-2}.

The sensitivity of the analysis was evaluated with the generation of pseudo-experiments to simulate the signal and the background. Thus, it was possible to derive the simulated distributions of the test statistic for the two hypotheses. A discovery is claimed when the observed test statistic exceeds a critical value. This value is determined from the distribution of the test statistic for the background only case for the 3σ (or 5σ) confidence level.

Two alternative searches were performed. In the candidate list search, the presence of an excess of signal events was tested at the location of 51 a-priori defined candidate sources. In the full-sky search, I looked for an excess of signal over the background anywhere in the

visible sky.

For the first time within the ANTARES collaboration, an estimate of the neutrino energy, i.e. the number of hits, has been included in the likelihood, in order to improve the discrimination between signal and background. The inclusion of the number of hits in the likelihood reduces the number of events (thus, the signal) needed for a 5σ discovery by $\sim$ 25% as shown in Figure 7.21.

In addition to these two searches, the algorithm has been tested in the presence of extended sources and neutrino fluxes described by an exponential cut-off functions. Simulations show that for a source with Gaussian extension $\sigma_{\rm source} = 1^{\circ}$, the flux needed for a 5σ discovery is roughly 1.4 higher compared to point-like sources. Assuming a neutrino flux parametrised by an exponential cut-off function (with cut-off energy $E_{\rm cutoff} = 1{\rm TeV}$) yields a discovery probability a factor 2 higher compared to the standard E_{ν}^{-2} case

Models of neutrinos emission for three Galactic sources, RX J1713.7-3946, Vela X and the Crab Nebula, were also tested. For RX J1713.7-3946 and Vela X the extension of the source was also taken into account. For this purpose, a convolution of the point spread function and the source extension has been included in the likelihood calculation. The results of this convolution is shown in Figure 7.22 for both RX J1713.7-3946 and Vela X. The source extension was directly derived from gamma-rays data published by the H.E.S.S. collaboration.

Results

In both the full-sky and the candidate list search, no significant excess of signal events was found. In the full-sky search the most significant cluster is located at $(\alpha, \delta) = (-46.5^{\circ}, -65.0^{\circ})$ where 5(9) events were found within 1(3) degrees of these coordinates. The value of the test statistic associated with this cluster is 13.1. This translates to a (post trial) p-value, i.e. the probability to obtain a test statistic at least as extreme as the one actually observed, of 2.6%.

In the candidate list search the most signal-like source is HESS J1023-575 where the fit yields 2 signal events. The post trial p-value of this cluster is 41%. Upper limits at 90% confidence level were then derived using the Feldman and Cousins prescription, assuming a neutrino flux proportional to E_{ν}^{-2}. These limits are shown in Figure 8.6 were they are compared with other published limits from various experiments. For some sources in the Southern sky, the limits obtained are the most restrictive ones. In this hemisphere the larger neutrino telescope IceCube, located at the South Pole, is sensitive to ultra high-energy neutrinos, $E_{\nu} > 1$ PeV, while in this analysis 80% of the signal events have 4 TeV $< E_{\nu} < 700$ TeV.

Upper limits were also derived assuming the different models discussed in Chapter 2 for RX J1713.7-3946, Vela X and the Crab Nebula. As an example, Figure 8.8 (bottom) shows the results obtained for the Crab Nebula. The limits obtained are quite above the predictions. This is mainly due to the low visibility of the Crab Nebula at the ANTARES site. More promising are the limits obtained for RX J1713.7-3946 and Vela X, as discussed in Chapter 8.

Although no excess of signal events was found, the work presented in this thesis is a step toward the first detection of TeV neutrinos from astrophysical sources. Perphaps the

ANTARES detector is too small to achieve such a discovery; however, with IceCube already running and KM3NET in construction the future of neutrino astronomy is bright. Let's just wait and see.

Samenvatting

Gedurende mijn promotie onderzoek van de afgelopen vier jaar heb ik verscheidene keren geprobeerd om mijn vrienden en familie uit te leggen waar ik mee bezig was. Ik weet niet zeker of dat gelukt is want vaak kon ik de conversatie niet afronden. Maar ik moet toegeven dat het leuk was om hun reactie te zien bij mijn introductie van "mysterieuze" onderwerpen zoals de versnelling van kosmische straling en het detectie principe van ANTARES. Deze samenvatting is waarschijnlijk mijn laatste poging om hen uit te leggen wat ik vier jaar heb uitgespookt in Nederland. Daarom hoop ik dat de ervaren lezer het mij niet kwalijk neemt dat ik begin met een algemene introductie in de astronomie en kosmische straling. Daarna ga ik verder met de beschrijving van ANTARES en leg ik uit hoe een quasi ongrijpbaar deeltje, genaamd het neutrino, gedetecteerd kan met een enorme detector op de bodem van de zee. In het laatste gedeelte van deze samenvatting sluit ik af met een beschrijving van de resultaten die ik heb behaald tijdens mijn onderzoek.

4. Astronomie met behulp van verschillende boodschappers

Bijna duizend jaar geleden, in 1054, observeerden Chinese, Japanse en Arabische astronomen een nieuwe "gastster" in het sterrenbeeld Stier. In die tijd was het gebruikelijk om een tijdelijk helder hemelobject dat nog niet eerder bekend was aan te duiden als "gastster". Alhoewel het de astronomen duidelijk was dat het hier niet ging om een komeet konden zij nog niet vermoeden wat ze precies gezien hadden: een supernova explosie.

Wanneer alle waterstof in een zware ster is gefuseerd, stort de ster ineen onder invloed van de zwaartekracht. Het evenwicht tussen enerzijds de stralingsdruk door kernreacties in de ster en anderzijds de gravitationele druk door haar eigen massa, is dan verstoord. Door de ineenstorting loopt de druk en de temperatuur in de ster tot dusdanig kritische waarden op dat helium-fusie processen opstarten. Dit herstelt het evenwicht, maar slechts tijdelijk. Nadat ook alle helium in de ster is gefuseerd ondervindt de ster opeenvolgende ineenstortingen, tot aan de fusie van zware elementen van de ijzer-groep. De precieze tijdsduur van de ineenstortingen hangt af van de initiële massa van de ster, en komt ten einde als alle fusie reacties zijn afgelopen, waarna de ster ineenstort onder haar eigen massa. Bij deze laatste implosie komt een enorme hoeveelheid energie vrij waarbij materiaal van de ster de interstellaire ruimte ingeblazen kan worden. Dit materiaal kan snelheden tot 30,000 km/uur bereiken, waardoor schokgolven kunnen worden gevormd door de interactie van het materiaal met het interstellaire medium in de omgeving van de ster. Deze schokgolven creëren sferische schillen van gas en stof die wij supernova overblijfsels noemen. Uiteindelijk kan, afhankelijk van de initiële massa van de ster, daarnaast een neutronenster of zwart gat worden gevormd.

Dit is wat er is gebeurd met de eerder genoemde "gastster". We noemen dit supernova overblijfsel tegenwoordig de Krab Nevel, zoals te zien is in Figuur 1. De Krab Nevel bevindt zich op een afstand van 2 kpc van de Aarde, wat betekent dat het licht dat wordt uitgezonden door dit object er 6523 jaar over doet om ons te bereiken.

In de afgelopen 50 jaar is de Krab Nevel uitgegroeid tot een van de meest waargenomen objecten in ons sterrenstelsel, vooral door haar helderheid en historische achtergrond. Deze waarnemingen zijn gedaan bij verschillende golflengten: van radiogolven tot zichtbaar licht, en van röntgen tot gamma straling.

Wat van belang is voor het onderzoek van mijn proefschrift is dat de Krab Nevel en andere galactische supernovae waarschijnlijk verantwoordelijk zijn voor de versnelling van kosmische straling. Behalve supernovae, moeten ook andere objecten als mogelijke versnellingsbronnen worden gezien, zoals galactische plerionen en microquasars, of extragalactische gammaflitsers en actieve galactische nucleï.

Kosmische straling

Kosmische straling bestaat uit energetische deeltjes die continu de atmosfeer van de Aarde bombarderen. Ze zijn in het begin van de twintigste eeuw ontdekt door Victor Hess, die drie electrometers tot een hoogte van 5.3 km meenam in ballonnen om zo de ionisatie van de atmosfeer te onderzoeken (zie Figuur 2). Tot zijn verbazing ontdekte hij dat de ioniserende stralings intensiteit toenam met de hoogte van de ballon. Als mogelijke verklaring stelde hij dat de straling van boven afkomstig moest zijn, en dus van buitenaardse afkomst moest zijn.

Een eeuw na zijn ontdekking zijn er nog steeds veel vragen over kosmische straling onbeantwoord. Zijn supernovae inderdaad de bronnen die verantwoordelijk zijn voor de versnelling van kosmische straling? Hoe werkt het versnellingsmechanisme precies? Waardoor komen de "knie" en "enkel" in het energie spectrum van de kosmische straling? Een manier om antwoorden op deze vragen te vinden is het detecteren van astrofysische neutrinos. Dit is het onderwerp van dit proefschrift.

Neutrino productie

Neutrino's zijn neutrale deeltjes die alleen een wisselwerking met andere deeltjes kunnen aangaan via de zwakke kernkracht. Hun bestaan werd gepostuleerd door Wolfgang Pauli in 1930, om het behoud van energie en impulsmoment in beta verval te verklaren. Een voor natuurkundigen bekende uitspraak van Pauli over het neutrino is: "Ik heb iets vreselijks gedaan, ik heb een deeltje gepostuleerd dat niet ontdekt kan worden" [176]. Gelukkig (voor dit proefschrift) werd deze uitspraak 25 jaar later door Reines en Cowan ontkracht, na hun geslaagde poging om antineutrino's afkomstig van beta verval in een kernreactor, te detecteren.

De lezer kan zich op dit moment afvragen: "Wat is de relatie tussen kosmische straling en neutrino's?" Het antwoord op deze vraag is de sleutel tot het waarom van mijn onderzoek. Neutrino's en kosmische straling hebben dezelfde oorsprong. Dat wil zeggen, ze worden gecreëerd door dezelfde astrofysische bronnen. Hoog-energetische neutrino's kunnen worden geproduceerd door de interactie van hoog-energetische kosmische straling,

voornamelijk nucleonen, met materie of licht dichtbij de bron. Bijvoorbeeld door een aantal nucleon-foton interacties en nucleon-nucleon processen.

Al deze reacties produceren zogenaamde pionen (π), lichte hadronen. Pionen zijn onstabiele deeltjes, dat wil zeggen ze vervallen in andere deeltjes. Een geladen pion vervalt in een muon (een lepton dat lijkt op een electron maar zwaarder) en een muon-neutrino. Een muon vervalt weer in een electron, een muon-neutrino-antineutrino paar, en een electron-neutrino. Neutrale pionen vervallen in twee fotonen.

Naast pion verval zijn er ook andere processen die bijdragen aan de emissie van gamma straling. Het is gebruikelijk om onderscheid te maken tussen hadronische processen, dat wil zeggen π^0 verval, en leptonische processen zoals emissie van synchrotron straling en inverse Compton verstrooiing. Het typische energie spectrum van een bron van gamma straling kan gesplitst worden in twee delen. Het laag-energetische gedeelte wordt bepaald door emissie van synchrotron straling. Inverse Compton verstrooiing en neutraal pion verval dragen bij aan het hoog-energetische gedeelte, tot tientallen TeV. De detectie van TeV gamma straling van specifieke bronnen wordt beschouwd als een eerste indicatie voor mogelijke neutrino emissie, hoewel het a priori niet mogelijk is om te bepalen of de gedetecteerde fotonen een leptonische of hadronische oorsprong hebben. Verschillende theoretische modellen kunnen gebruikt worden om de energie verdeling van mogelijke bronnen van kosmische straling te voorspellen. Deze modellen hangen sterk af van bron-afhankelijke parameters zoals het magnetische veld en de proton dichtheid, die slechts indirect bepaald kunnen worden. Kosmische straling wordt beïnvloed door galactische en extra-galactische magnetische velden, terwijl gamma straling een wisselwerking met de alom aanwezige kosmische achtergrond straling ondervindt. Dit geldt echter niet voor neutrino's, die altijd direct terugwijzen naar hun bron.

5. Neutrino astronomie met ANTARES

De detectie van astrofysische neutrino's werd in 1960 voor het eerst overwogen door de Russische natuurkundige Moisei Aleksandrovich Markov [104]. Hij stelde voor "om detectoren diep in een meer of in de zee te installeren en om de richting van geladen deeltjes te bepalen met behulp van Cherenkov straling". Het achterliggende idee is dat astrofysische neutrino's een wisselwerking via de zwakke wisselwerking ondervinden met materie rondom de detectoren, waarbij geladen leptonen worden geproduceerd[2]. Als geladen leptonen zich met hoge snelheid door water bewegen zullen zij Cherenkov straling te weeg brengen.

Dit concept is overgenomen door de bedenkers van ANTARES: het realiseren van een onder-water neutrino telescoop, op de bodem van de Middellandse Zee. ANTARES is een drie-dimensionale verzameling van 885 lichtsensoren die ieder onder een hoek van 45° naar beneden zijn gericht en aan 12 kabels zijn gemonteerd. Een illustratie van ANTARES is te zien in Figuur 3.

De kwaliteit van een telescoop wordt doorgaans uitgedrukt in termen van hoekresolutie en detectie efficiëntie, en kan worden bepaald door middel van simulatie. Voor de meetgegevens die zijn geanalyseerd in dit proefschrift, is de hoekresolutie $0.46 \pm 0.10^\circ$

[2] Neutrale zwakke stroom interacties zijn ook mogelijk, maar deze worden in dit proefschrift buiten beschouwing gelaten.

aangenomen dat de neutrino flux evenredig is met E_ν^{-2}. Het effectieve oppervlak van de detector neemt toe als functie van de neutrino energie en bedraagt ongeveer 0.1, 1 en 10 m^2 voor een neutrino's energie van respectievelijk 1, 100 en 10000 TeV.

6. Mijn onderzoek

Gedurende mijn vier jaar in de ANTARES groep ben ik betrokken geweest bij de zoektocht naar puntbronnen van astrofysische neutrino's. De aanwezigheid van kosmische neutrino's boven de achtergrond is onderzocht door te kijken naar clusters van neutrino's uit een bepaalde richting. Hiervoor is een optimale hoekresolutie van groot belang.

De analyse zoals gepresenteerd in dit proefschrift is gebaseerd op vier jaar meten tussen, januari 2007 tot december 2010. De totale meettijd bedraagt 813 dagen.

Neutrino's zijn geselecteerd door het toepassen van een aantal criteria. Ten eerste zijn alleen opgaande neutrino sporen in beschouwing genomen. Vervolgens zijn selectie criteria toegepast met betrekking tot de kwaliteit van het gereconstrueerde spoor, om zo verkeerd gereconstrueerde atmosferische muonen te verwerpen. Deze criteria zijn gekozen om de waarschijnlijkheid van een ontdekking te maximaliseren. Deze waarschijnlijkheid woordt uitgedrukt in de neutrino flux die nodig is om met 50% kans een signaal met 5σ significantie waar te nemen. De aanname is dat de flux een E_ν^{-2} spectrum volgt. De selectie omvat 3058 neutrino's. Ter vergelijking, simulaties voorspellen 358 ± 179 atmosferische muonen en 2408 ± 72 atmosferische neutrino's in de selectie.

De zoektocht naar astrofysische neutrino's is gebaseerd op een kansberekening. De nul hypothese komt overeen met de mogelijkheid dat de data selectie alleen achtergrond bevat (atmosferische muonen en neutrino's). De andere hypothese neemt de mogelijkheid in rekening dat behalve achtergrond de selectie ook astrofysische neutrino's bevat.

De gevoeligheid van de analyse is berekend door middel van het genereren van pseudo-experimenten bestaande uit gesimuleerde signalen en achtergrond. Zodoende zijn verdelingen voor de kansen van de twee hypotheses bepaald. Een ontdekking kan gemaakt worden als de kans een kritieke waarde over schrijdt. Deze waarde is zo gekozen dat de achtergrond hypothese met 3σ (of 5σ) significantie verworpen kan worden.

Er zijn twee alternatieve analyses gedaan. Ten eerste is de aanwezigheid van een signaal in de selectie getest aan de hand van een lijst van 51 a-priori bepaalde potentiële neutrino bronnen. Ten tweede heb ik in de hele hemel gezocht naar een signaal binnen de selectie klasse.

Voor de eerste keer in ANTARES is hierbij gebruik gemaakt van een meting van de neutrino energie, in dit geval gebaseerd op het aantal hits in de detector, om zodoende het onderscheid tussen signaal en achtergrond te verbeteren. Hierdoor is het benodigde aantal neutrino's voor een 5σ ontdekking verminderd met $\sim 25\%$.

De analyse is verder toegepast op neutrino bronnen met een uitgebreide ruimtelijke structuur, en op neutrino fluxen met cut-off energie. Simulaties laten zien dat de neutrino flux afkomstig van een bron met een Gaussische vorm ($\sigma_{\mathrm{bron}} = 1^\circ$) ongeveer 1.2 keer hoger moet zijn dan die van een puntbron. De ontdekkingswaarschijnlijkheid voor een neutrino flux die gekenmerkt wordt door een cut-off energie van $E_{\mathrm{cut-off}} = 1\mathrm{TeV}$ is 2 keer zo laag vergeleken met een neutrino flux met een E_ν^{-2} spectrum.

Neutrino flux modellen van drie galactische bronnen, RX J1713.7-3946, Vela X en de Krab Nevel, zijn ook getest. In het geval van RX J1713.7-3946 en Vela X is de ruimtelijke uitgebreidheid van de bron ook in rekening genomen.

De ruimtelijke uitgebreidheid van de bronnen is bepaald aan de hand van de afbeeldingen voor de gamma straling gepubliceerd door de H.E.S.S. collaboratie.

Resultaten

In geen van de zoektocht is een signaal gevonden. De meest significante positie in de hemel heeft coördinaten $(\alpha, \delta) = (-46.5°, -65.0°)$ waar 5(9) neutrino's zijn gevonden binnen 1(3) graden van de eerder genoemde coördinaten. De kansberekening leert dat de achtergrondhypothese met 2.6% waarschijnlijkheid overeen komt.

De kandidaat bron met het sterkste signaal is HESS J1023-575, waarbij 2 neutrino's gevonden zijn. De waarschijnlijkheid dat die achtergrond is, is 41%. Flux limieten met een 90% significantie zijn berekend met behulp van de Feldman en Cousins methode, onder de aanname dat de neutrino flux een E_ν^{-2} spectrum volgt. Voor sommige bronnen in het zuidelijk halfrond zijn de behaalde limieten de meest beperkende ter wereld. In dit halfrond is IceCube, alleen gevoelig voor zeer-energetische neutrino's, $E_\nu > 1\,\mathrm{PeV}$, terwijl in deze analyse 80% van het signaal uit neutrino's bestaat met een energie tussen $4\,\mathrm{TeV}$ en $700\,\mathrm{TeV}$.

Voor RX J1713.7-3946, Vela X en de Krab Nevel zijn ook limieten berekend onder aanname van de verschillende modellen die zijn besproken in Hoofdstuk 2..

Alhoewel er geen signaal boven de achtergrond is gevonden is het onderzoek in dit proefschrift een stap naar de eerste detectie van TeV neutrino's afkomstig van astrofysische bronnen. Hiervoor is de ANTARES detector niet groot genoeg. Maar met de reeds operationele IceCube detector en de bouw van KM3NET gaat de neutrino astronomie een hoopvolle toekomst tegemoet. Laten we daarom afwachten wat de toekomst ons brengt.

Riassunto

In questi quattro anni trascorsi da dottorando, ho provato parecchie volte a spiegare ad amici e parenti che cosa stessi facendo. Non sono sicuro di esserci riuscito visto che molte volte non sono stato in grado di finire la conversazione iniziata. Devo ammettere però che la loro espressione, mentre introducevo "misteriosi" argomenti quali l'accelerazione di raggi cosmici e il principio di funzionamento di ANTARES, erano abbastanza divertenti. Questo riassunto rappresenta probabilmente il mio ultimo tentativo di spiegare loro cosa ho fatto in Olanda in questi ultimi quattro anni, quindi spero che un lettore più esperto non rimanga deluso se inizierò con un'introduzione generale sull'astronomia e i raggi cosmici. In seguito, rivolgerò la mia attenzione su ANTARES e spiegherò come è possibile rivelare queste particella elusiva, chiamata neutrino, con un grande rivelatore in fondo al mare. Infine, la terza ed ultima parte di questo riassunto descriverà i risultati ottenuti.

7. Astronomia multimessenger

Quasi mille anni fa, nel 1054 D.C., astronomi cinesi, giapponesi ed arabi osservarono la presenza di una nuova stella "ospite" nella costellazione del Toro. All'epoca, gli astronomi usavano il termine "ospite" per identificare oggetti celesti che apparivano temporaneamente nel cielo in luoghi dove precedentemente non era stata osservata alcuna stella. Sebbene fosse chiaro che questa stella "ospite" fosse in qualche modo diversa da ciò che ora noi chiamamo cometa, all'epoca non potevano sapere che stavano osservando l'esplosione di una supernova.

Quando una stella brucia tutto il suo combustibile idrogeno, inizia un collasso gravitazionale. L'equilibrio e' rotto, la pressione di radiazione delle reazioni nucleari non può più sostenere la pressione gravitazionale dovuta alla massa della stella. A causa del collasso, la densità e la temperatura della stella aumentano, raggiungendo il valore critico che inizia il processo di consumo dell'elio. Dopo che anche l'elio viene esaurito, il collasso continua fino a che la fusione di elementi più pesanti del gruppo del ferro inizia. Questo meccanismo, che dipende fortemente dalla massa iniziale della stella, continua fino a che le reazione di fusione terminano e la stella collassa sotto la propria pressione gravitazionale. Questa implosione può causare l'espulsione di materia stellare nello spazio interstellare e il rilascio di un ammontare enorme di energia. Il materiale viene espulso a velocità fino a 30.000 km/s e un'onda "shock" si crea dalle interazioni della materia con il mezzo interstellare. L'onda "shock" spazza via il circostante volume di gas e polveri creando ciò che ora chiamiamo il "resto" di supernova.

Viene così creata una stella di neutroni o, nel caso la stella fosse molto massiva, un buco nero.

Quanto appena descritto è quanto accaduto alla stella "ospite" osservata nel 1054 D.C..

Al giorno d'oggi, questo resto di supernova è chiamato Nebulosa del Granchio (Figure 1). La Nebulosa del Granchio è situata ad una distanza approssimativa di 2 kpc dalla Terra, il che significa che la luce emessa da questo oggetto viaggia per 6523 anni prima di raggiungere il nostro pianeta.

Negli ultimi 50 anni, la Nebulosa del Granchio è diventata uno degli oggetti più studiati della nostra Galassio, sopratutto grazie alla sua luminosità e importanza storica. Queste osservazioni sono state fatte a diverse lunghezze d'onda: dalle onde radio alla banda visibile, dai raggi x alla banda dei raggi gamma.

Ciò che conta per il lavoro presentato in questa tesi è che la Nebulosa del Granchio e altre supernovae di origine galattica sono responsabili per l'accelerazione dei raggi cosmici. Accanto alle supernovae, altri oggetti sono ritenuti possibili sorgenti candidate per l'accelerazione dei raggi cosmici. Ne sono un esempio i plerioni e le microquasar o, al di fuori della Via Lattea, i "gamma-ray bursts" e i nuclei galattici attivi.

I raggi cosmici

I raggi cosmici sono particelle energetiche che penetrano continuamente l'atmosfera terrestre. Sono stati scoperti all'inizio del ventesimo secolo da Victor Hess, il quale trasportò tre elettrometri ad un'altitudine di 5.3 km usando palloni aerostatici con l'intento di indagare la ionizzazione dell'atmosfera (vedi Figura 2). Con molta sorpresa, egli osservò che la ionizzazione alle altidudini maggiori era più grande di quella misurata al suolo. La sola possibile spiegazione fu che la radiazione doveva provenire dall'alto, quindi di origine extra-terrestra.

Un secolo dopo la loro scoperta, ci sono ancora parecchie domande aperte riguardo i raggi cosmici: "Le supernovae sono o no responsabili per la l'accelerazione dei raggi cosmici? E come funziona questo meccanismo esattamente? Cosa sono il "ginocchio" e la "caviglia" osservanti nello spettro energetico?". Un modo per rispondere a queste domande è quello di cercare e rivelare neutrini astrofisici. Proprio questo, è l'argomento principale di questa tesi.

Produzione di neutrini

I neutrini sono particelle neutrali che interagiscono soltanto attraverso la forza debole. La loro esistenza fu proposta la prima volta nel 1930 da Wolfgang Pauli nel tentativo di spiegare la conservazione dell'energia e del momento angolare nei decadimenti beta. Molto famoso è il commento che Pauli pronunciò in merito alla propria interpretazione: "Ho fatto una cosa terribile, ho postulato l'esistenza di una particella che non può essere rivelata" [176]. Fortunatemente (per questa tesi), questa affermazione fu smentita 25 anni dopo quando Reines e Cowan rivelarono antineutrini creati da decadimento beta in un reattore nucleare.

Il lettore si starà chiedendo a questo punto: "Che relazione c'è tra raggi cosmici e neutrini?". La risposta a questa domanda è la chiave per capire il mio lavoro. Neutrini e raggi cosmici condividono la stessa origine, ovvero sono creati dalle stesse sorgenti. La produzione di neutrini altamente energetici è causata dall'interazione di raggi cosmici

accelerati, sopratutto nucleoni, con materia densa o fotoni nei pressi della sorgente di raggi cosmici.

Tutte queste reazioni producono i cosiddetti pioni, i mesoni più leggeri. I pioni sono particelle instabili, quindi decadono. I pioni carichi decadono in muoni, che non sono altro che leptoni simili agli elettroni ma molto più massivi, producendo un neutrino muonico. Il decadimento di muoni in elettroni genera un altro neutrino muonico e un ulteriore neutrino elettronico. I pioni neutrali invece decadono in due fotoni.

Accanto al decadimento dei pioni, ci sono altri processi che contribuiscono all'emissione di raggi gamma. È molto comune distinguere tra processi adronici, appunto il decadimento del pione π^0, e processi leptonici come l'emissione di sincrotrone e lo scattering Compton inverso. Il tipico spettro energetico per una sorgente può essere diviso in due parti. Quella a basse energie è dominata dall'emissione di sincrotrone. Scattering Compton inverso e decadimento di pioni neutri contribuiscono alla parte ad alte energie dello spettro, di solito fino a decine di TeV. Si può ora facilmente capire come il rivelamento di raggi gamma ad energie TeV da una precisa sorgente è generalmente considerato il primo indizio per una possibile emissione di neutrini, sebbene non vi sia un modo di distinguere a priori se i fotoni rivelati sono di origine leptonica o adronica.

Molti modelli teorici stanno cercando di spiegare lo spettro energetico per molte sorgenti candidate di raggi cosmici. Queste modelli in genere dipendono fortemente da parametri legati alle sorgenti stesse quali il campo magnetico e la densità di protoni, parametri che possono essere solo assunti. Per quanto riguarda i modelli adronici, è chiaro che il rivelamento di un segnale di neutrini astrofisici potrebbe limitare l'intervallo di valori dei parametri assunti. Mentre i raggi cosmici sono deviati da campi magnetici Galattici e extra-Galattici e i raggi gamma interagiscono con la radiazione cosmica di fondo, i neutrini conservano l'informazione sulla direzione.

8. L'astronomia dei neutrini con ANTARES

Il rilevamento di neutrini astrofisici fu per la prima volta proposto nel 1960 dal fisico russo Moisei Aleksandrovich Markov [104]. Egli suggerì di posizionare un rivelatore nel fondo di un lago o del mare e determinare la direzione di particelle cariche con l'aiuto della radiazione Cherenkov. L'idea di base è che i neutrini emessi da sorgenti astrofisiche interagiscono con la materia per mezzo delle interazioni di corrente carica creando in questo modo leptoni. Attraversando l'acqua, questi leptoni emettono radiazione Cherenkov.

Questa idea è stata adottata dalla collaborazione ANTARES per costruire il primo telescopio per neutrini nel Mar Mediterraneo. ANTARES può essere considerato come una grossa rete costituita da 12 linee, con un totale di 885 fotomoltiplicatori inclinati di 45° rispetto all'asse verticale. Un'illustrazione di ANTARES è mostrata in Figura 3.

Tramite simulazione sono state calcolate la risoluzione angolare e l'area effetiva. Per i dati analizzati in questo lavoro, assumendo un flusso di neutrini proporzionale a E_ν^{-2}, la risoluzione angolare ottenuta è di 0.466$\pm$0.10. L'area effetiva, ovvero l'area che si otterrebbe con un rivelatore efficiente al 100%, aumenta con l'energia del neutrino ed è approssimativamente 0.1, 1 e 10 m^2 a 1, 100 e 10000 TeV rispettivamente.

9. Il mio lavoro

Durante questi quattro anni in ANTARES, sono stato coinvolto nella ricerca di sorgenti puntiformi di neutrini astrofisici. In pratica, la presenza di un eccesso di neutrini astrofisici sul background veniva testata cercando "clusters" di eventi in una direzione data. Ovviamente, per questo tipo di analisi, una buona risoluzione angolare come quella di ANTARES, è di fondamentale importanza.

L'analisi presente in questa tesi si basa su quattro anni di dati raccolti da gennaio 2007 a dicembre 2010.

I candidati neutrini sono stati selezionati attraverso tre diversi tagli. Innanzitutto, soltanto gli eventi ricostruiti come "upgoing", cioè provenienti dal basso, sono stati selezionati. Quindi, tagli sulle variabili di qualità β e Λ sono stati imposti nel tentativo di rigettare muoni atmosferici selezionati per errore dal primo taglio. Questi tagli sono stati scelti ottimizzando la probabilità di scoperta, cioè il flusso di neutrini necessario per ottenere una probabilità del 50% di rivelare il signale con un livello di significanza di 5σ. Il campione finale di dati è costituito da 3058 candidati neutrini.

L'analisi è basata sul test del rapporto di verosomiglianza. L'ipotesi nulla è rappresentata dalla situazione in cui sono presenti solo muoni e neutrini atmosferici nel campione di dati. L'ipotesi alternativa invece si riferisce al caso in cui in aggiunta al background il segnale è presente con un flusso proporzionale a E_ν^{-2}.

La sensitività dell'analisi è stata calcolata attraverso la generazione dei cosidetti "pseudo-experiments", in cui venivano simulati sia il segnale che il background. In questo modo è stato possibile derivare la distribuzione della statistica del test per le due ipotesi. La scoperta viene fatta nel momento in cui la statistica del test osservata supera un valore critico determinato, attraverso la simulazione, dalla distribuzione della statistica del test per il solo background per un livello di confidenza di 3σ (or 5 σ).

In questa analisi due ricerche alternative sono state fatte. Nel primo caso, "candidate list search", sono state considerate 51 sorgenti candidate, individuate. Per ognuna di queste sorgenti la presenza di un eccesso di eventi segnale è stata testata. Nella ricerca a-tutto-cielo, "full-sky search", il segnale è stato cercato in ogni zona del cielo visibile.

Per la prima volta all'interno della collaborazione ANTARES, un estimatore dell'energia del neutrino è stato utilizzato nella verosimiglianza nel tentativo di migliorare la discriminazione tra segnale e background. L'estimatore scelto è il numero di "hita", dove un "hit" rappresenta una variabile che trasporta informazione riguardo la carica e il tempo di un evento. L'utilizzo di una funzione di densitaà di probabilità contenente informazione sul numero di "hits" è in grado di ridurre il numero di eventi necessari per una scoperta con livello di confidenza a 5σ del 25% circa come mostrato nella Figura 7.21.

In aggiunta a queste due ricerche, l'algoritmo utilizzato è stato anche testato in presenza di sorgenti estese e di neutrini con flussi descritti da funzioni esponenziali con "cut-off". Le simulazioni hanno mostrato che per una sorgente con un'estensione Gaussiana $\sigma_{\rm source} = 1^\circ$, il flusso necessario per una scoperta a 5σ è circa 1.4 volte maggiore rispetto al caso di sorgente puntiforme. Assumendo invece un flusso di neutrini parametrizzato da una funzione esponenziale con "cut-off" (con un valore di energia al "cut-off" pari a 1 TeV) si ottiene una probabilità di scoperta due volte maggiore rispetto al caso standard di flusso proporzionale a E_ν^{-2} .

Sono stati anche testati modelli teorici che descrivono l'emissione di neutrini da tre sorgenti Galattiche: RX J1713.7-3946, Vela X e la Nebulosa del Granchio. Per quanto riguarda RX J1713.7-3946 e Vela X si è tenuto conto anche del fatto che entrambe le sorgenti sono estese. A tal fine, una convoluzione tra l'estensione della sorgente e la "point spread function" è stata inclusa nella verosimiglianza. La Figura 7.22 mostra il risultato di questa convoluzione sia per RX J1713.7-3946 sia per Vela X.

Risultati

Sia nella ricerca "full-sky" che nella ricerca "candidate list" non è stato trovato un eccesso significativo di eventi. Nella ricerca "full-sky", il cluster piè significativo è situato alle coordinate $(\alpha, \delta) = (-46.5°, -65.0°)$ dove 5(9) eventi sono stati trovati entro 1(3) gradi da esse. Il valore della statistica del test associato a questo cluster è di 13.1. Ciò si traduce direttamente in un p-value, cioè la probabilità di ottenere una statistica del test pari o più estrema di quella osservata, pari al 2.6%.

Nella ricerca su sorgenti candidate la sorgente significativamente più importante è HESS J1023-575 dove il fit ha trovato 2 eventi segnale. Il p-value in questo caso è del 41%. Non avendo rivelato neutrini astrofisici mi sono dovuto accontentare di derivare limiti superiori con livello di confidenza del 90% al flusso di neutrini. Questi limiti sono mostrati in Figura 8.6 dove sono messi a confronto con altri limiti pubblicati da vari esperimenti. Per alcune di queste sorgenti nell'Emisfero Australe, i limiti derivati sono attualmente i più restrittivi (evvai!). Bisogna però ricordare che in questa parte del cielo, l'esperimento IceCube, situato al polo Sud e molto (ma molto) più di ANTARES, è sensibile a neutrini di energia superiore a 1 PeV, mentre in questa analisi l'80% degli eventi segnale ha un'energia compresa tra 4 TeV e 700 TeV.

Sono stati anche derivati limiti superiori assumendo i diversi modelli di emissione di neutrini astrofisici discussi nel Capitolo 2 per RX J1713.7-3946, Vela X e la Nebulosa del Granchio. Come esempio, la Figura 8.8 (in basso) mostra i risultati relativi a quest'ultima. I limiti ottenuti sono ben al di sopra delle previsioni. Ciò è dovuto principalmente alla bassa visibilità della Nebulosa alla latitudine di ANTARES. Risultati più promettenti sono stati invece raggiunti per RX J1713.7-3946 e Vela X come discusso nel Capitolo 8

Sebbene non sia stato trovato un eccesso di eventi segnale, l'analisi presentata in questa tesi rappresenta un piccolo passo verso il primo rivelamento di neutrini astrofisici di energia TeV. Nonostante il telescopio ANTARES sia forse troppo piccolo per ottenere un risultato di tale importanza, il futuro della astronomia dei neutrini è luminoso grazie al contributo presente di IceCube e futuro di KM3NET. Basta solo avere pazienza, e aspettare.

About the author

Claudio Bogazzi was born on October, 30th 1984 in Massa, Italy. He spent most of his childhood playing football, his true passion, for a local team. During the high-school years at the *Liceo Scientifico Guglielmo Marconi* in Carrara, he developed a keen interest in physics and astrophysics. He then decided to study physics at the University of Pisa in 2003 and after five and a half years he graduated with 107/110 mark.

While working on his master thesis he had the opportunity to spent three months in Amsterdam, working at the NIKHEF institute with the Astroparticle Physics - ANTARES group. He enjoyed this experience so much that he decided to apply for a Ph.D. position in the same group. His work as Ph.D. candidate started in June 2009 and ended four years later.

Acknowledgements

This work would not be the same without the help of a lot people. I therefore would like to spend this section to thank them.

First I would like to thank my supervisor Aart Heijboer for a lot of good reasons that can be summarised as: countless afternoons spent trying to explain me how a good code works and/or what hypothesis testing really is. Working together with him was a pleasure. Many collegues always reminded me how lucky I was to have Aart as supervisor. They were right.

Another person who deserves to be acknowledged in these first sentences is my promotor Maarten de Jong. Every conversation I had with Maarten always added something to my knowledge. Whether it was physics or economy, I always enjoyed listening to him.

And of course a huge thanks to all my colleagues (past and present) of the ANTARES group at NIKHEF: Akis, Ana, Arjen, Ching-Cheng, Claudio, Corey, Dimitris, Dorothea, Jelena, Jeroen, Eleonora, Els, Erwin, Gordinho, Guus, Maria, Mieke, Patrick, Paul, Robert, Ronald, Stephan, Tino, Tri. So many nice things to remember with all of you!

I had a very great time working for a nice collaboration such as ANTARES. I really hope that the nice and friendly atmosphere experienced in each collaboration meeting I went to will also be there for KM3NET. I would like to thank people like Antoine, Juande Juergen and Paschal for all the feedback and suggestions given to my analysis.

There are other very important persons who deserve to be mentioned, but as I am allowed to acknowledge only those who were involved in this work I will thank them personally.

Claudio Bogazzi, February 2014.